A BODY-EXACT STRIP THEORY APPROACH TO SHIP MOTION COMPUTATIONS

by

Piotr Józef Bandyk

A dissertation submitted in partial fulfillment
of the requirements for the degree of
Doctor of Philosophy
(Naval Architecture and Marine Engineering)
in The University of Michigan
2009

Doctoral Committee:

Professor Robert F. Beck, Chair
Professor Smadar Karni
Professor Armin W. Troesch
Associate Reseach Scientist Okey Nwogu

ACKNOWLEDGEMENTS

I would like to give a special thanks to Prof. Beck for being my thesis adviser and a great friend. From early on as an undergraduate in his courses, to the days when we would spend hours discussing research, his vast insight, attention to detail, and guidance have made this dissertation possible. A very special thanks to my committee members, Dr. Nwogu, Prof. Troesch, and Prof. Karni, for their individual contributions to my education and helpful discussions about research.

I also want to thank my family, especially my parents, Jerzy and Maria Bandyk, for their continuous support, encouragement, and understanding throughout my entire academic career. From a home-cooked meal, to helping with work around the car, it makes life is a little more enjoyable and less stressful.

I want to thank my friends, in and outside school, for being there when I needed them and being patient with me when research required all of my attention. I would especially like to thank my colleagues and office-mates, Jim Bretl, Ellie Nick, and Chris Hart, for countless meaningful conversations, whether they be about schoolwork or not.

I want to thank the Naval Architecture and Marine Engineering department faculty and staff for providing an excellent environment for learning and helping with funding along the way. My continuous career from undergraduate to graduate school is a testament to their dedication to the students.

TABLE OF CONTENTS

LIST OF FIGURES

LIST OF TABLES

LIST OF APPENDICES

Appendix

ABSTRACT

A BODY-EXACT STRIP THEORY APPROACH TO SHIP MOTION
COMPUTATIONS

by

Piotr Józef Bandyk

Chair: Robert F. Beck

A body-exact strip theory is developed to solve nonlinear ship motion problems
in the time-domain. The hydrodynamic model uses linearized free surface conditions
for computational efficiency and stability, and exact body boundary conditions to
capture events such as slamming and submergence. The strip theory approach is used
to speed up computations and reduce the difficulty in modeling complex geometries.
A nonlinear rigid body equation of motion solver is coupled to the hydrodynamic
model to predict ship responses in large waves.

Constant source strength flat panels are used to model the body and desingularized
sources are used on the free surface. At each time-step, a mixed boundary value
problem is solved. The free surface and rigid body motions are evolved using a fourth-
order Adams-Bashforth time-stepping technique. The acceleration potential is used
to increase numerical accuracy and highlight the coupling between the hydrodynamic
and rigid body motion problems, improving stability.

The problem formulation is comprehensive, and details of numerical techniques are

included. Two-dimensional problems are used to study the accuracy and convergence of the method. Strip theory results include a variety of hull forms: two Wigley models (I and III), a Series-60 hull, the ITTC standard S-175 containership, and two naval vessels. This emphasizes the robust capabilities of the method and presents a variety of analyses for discussion. The two-dimensional and strip theory results include small and large amplitude motions. Comparisons to experiments and other numerical methods are shown and discussed, when possible. In several cases, a variety of alternative solution techniques are shown to highlight improvements or differences in problem formulation.

The results obtained show good agreement with previous computational and experimental results. The method developed is accurate, robust, very computationally efficient, and can predict nonlinear ship motions. It is well suited to be used as a tool in ship design or as part of a path optimization model.

CHAPTER I

Introduction

There are various aspects to ship design, such as strength, stability, resistance and propulsion, seakeeping, maneuvering and controls. Tools and techniques are available to assess the qualities or characteristics of these components, but very few of them overlap and take other components into consideration. There are "total" design packages which estimate all of these aspects at the most primitive level and offer a well-balanced design. In certain cases, it is perhaps unnecessary or impractical to delve too deeply into how these pieces of ship design fit together and influence one another. However, certain relationships can not be treated independently. In particular, the seakeeping performance of a ship will have significant impact on the rest of the design.

Linear strip theory can provide quick answers for preliminary design, but is unable to predict behavior for extreme events which are often of interest. The goal of this dissertation is to formulate an approach that can predict nonlinear events while being computationally efficient and robust. This approach can then be used in the design stage or for real-time simulations to predict vessel loading and responses.

1.1 Background

Wehausen and Laitone (1960) give a detailed overview of various analytical meth-

ods for fluid problems. The governing equations and certain ideas have remained unchanged, such as the use of potential flow theory. The boundary element method is the most common technique to solve these problems. However, the implementation of the ideas has been evolving.

Modern seakeeping computations date back to the 1950's. Korvin-Kroukovsky and Jacobs (1957) discuss a slender-body approach to model heave and pitch motions. Gerritsma and Beukelman (1967) validated a strip theory with experimental results. These resulted in one of the most significant developments, the classical strip theory by Salvesen et al. (1970), including forward speed effects using the methods derived by Ogilvie and Tuck (1969). They extended the frequency-domain strip theory approach to five degrees-of-freedom. The surge degree-of-freedom was added in a consistent manner by Beck (1989).

Several attempts were made to combine the low-frequency slender-body theory with the high-frequency strip theory. The unified theory of Newman (1978) and the asymptotic matching method of Yeung and Kim (1985) are just two examples.

These frequency-domain methods are used extensively for linear calculations and are very satisfactory for small amplitudes. In order to capture nonlinearities, more work must be done. The increase in computational power has made it feasible to solve the viscous problem in the time-domain, as is done in unsteady Reynolds-Averaged Navier-Stokes (RANS) codes. The computational effort perhaps outweighs the results, even on modern computers. A one-minute time history of a ship in a seaway may take hundreds or thousands of CPU hours to simulate.

The time-domain approach has been applied to the potential flow theory for computational efficiency and capturing of nonlinear effects. The Mixed Euler-Lagrange (MEL) approach was developed by Longuet-Higgins and Cokelet (1976), solving the fully nonlinear two-dimensional water wave problem. MEL methods have been used to solve the fully nonlinear three-dimensioanl wave and wave-body interactions, Cao

et al. (1990), Cao (1991), Scorpio et al. (1996). A mixed boundary value problem is set up by knowing the instantaneous body velocity and free surface elevation. Nonlinear free surface boundary conditions are used to update the wave amplitude and an equation of motion solver may be used to update the body velocity and position. Free surface instabilities have been found in many cases, and wave breaking may occur. Techniques to overcome these issues have been proposed, but they are not very robust. Results of the MEL method are discussed by Beck (1999).

Sclavounos et al. (1997) discuss the developement of SWAN-1 and SWAN-2 based on the linearized double-body formulation, originally presented by Dawson (1977). Both codes are three-dimensional. SWAN-1 is linearized about the calm water surface, while SWAN-2 utilizes the weak scatterer hypothesis by Pawlowski (1992), in which the ship is assumed to be a weak scatterer whose presence has negligible effects on the incident and steady wave field. Kring et al. (1996) present results using this approach, and they appear to be an improvement on motion prediction over linear theory.

The 2D+t approach has been developed by Maruo and Song (1994) and Tulin and Wu (1996). The two-dimensional flow problem is solved at cross-sections of the ship. Hyperbolic marching is used in the longitudinal direction, starting at the bow, to account for the free surface interactions between the two-dimensional sections. A similar approach was developed by Faltinsen and Zhao (1991). These methods show significant improvements over strip theory for high-speed ships. The 2D+t methods may still utilize the fully nonlinear free surface conditions. The difficulty in evolving the nonlinear free surface is when large amplitude motions cause waves to break.

In potential flow, large amplitude motion problems are most easily dealt with by using linearized free surface and exact body boundary conditions. This so called body-exact problem was developed by Beck and Magee (1990) using a time-domain Green's function. A similar approach for a surface-piercing body was developed by Lin and Yue (1990). The variability of wetted surface and hull shape changes due to

incident waves and ship motions can be modeled accurately. Beck and Reed (2001) give a good overview of the state-of-the-art for ship motion computations, describing some of the methods listed here.

In the simplest case of the body-exact blended method, exact hydrostatics and Froude-Krylov exciting forces can be combined with linear diffraction and radiation forces, as the latter two are more expensive to calculate. Finn et al. (2003) present a strip theory approach where the nonlinear radiation forces are calculated in geometrically complex sections where nonlinearities occur, such as the bow.

Zhang and Beck (2007) discuss two-dimensional large amplitude motions of circular, box, and wedge shapes. The slamming problem is presented with encouraging results. Zhang (2007) continues to extend the body-exact approach to three-dimensions and good results are shown for a Wigley Hull and S-175 Containership when compared to other codes and experiments. Zhang et al. (2007) extend the two-dimensional code to a strip theory for arbitrary hull geometries and an extensive comparison is done between the strip theory and three-dimensional results. The methods compare well, although the advantages of the strip theory are evident: computation time is an order of magnitude faster and modeling arbitrary hull geometries is not as complicated.

Fossen (1991) describes the six degree-of-freedom rigid body equations of motions for underwater and surface marine vehicles. Fossen (2005) uses this approach for nonlinear ship motion predictions. However, the linear frequency-domain hydrodynamic coefficients are used. Using the time-domain approach, numerical instabilities may arise in the equations of motion. A possible solution to this is to determine the fluid acceleration directly. The utilization of the so called "acceleration potential" can be found in Vinje and Brevig (1981) for the two-dimensional problem, and extended to three-dimensions by Kang and Gong (1990) and Tanizawa (1995).

The acceleration potential can be used along with the body equations of motion to improve numerical stability. Examples of this can be seen in Yang (2004) and van

Daalen (1993). Most of these methods utilize linear hydrodynamic models. Kang and Gong (1990) show some interesting nonlinear results for large amplitude motions of a sphere.

Bishop and Price (1981) presented one of the first comparisons of the seakeeping and maneuvering formulations, in their classical sense. Later, Bailey et al. (1998) made an attempt at combining seakeeping and maneuvering into a unified model. They describe some techniques to correct the hydrodynamic coefficients and account for the viscous characteristics found in maneuvering. Fossen and Smogeli (2004) describe a combined approach for the equations of motion, linear hydrodynamics, and viscous maneuvering term corrections. Fang et al. (2005) and Sutulo and Guedes Soares (2008) describe similar methods to model a ship undergoing a turning circle in a wave field. In both cases, the hydrodynamic model is based on a linear strip theory.

1.2   Overview

This dissertation presents the development of a blended method that captures the nonlinearities of the loads acting on the ship while using linear free surface conditions. The nonlinear hydrodynamic model is coupled to a nonlinear rigid body equation of motion solver. Aspects of maneuvering theory may be carefully added to the seakeeping model to demonstrate how they affect one another. Traditionally, the seakeeping and maneuvering are treated separately. Care must be taken to account for the overlap between the high-frequency potential flow seakeeping model and the low-frequency maneuvering model, where viscous terms are important.

The combination of a body-nonlinear time-domain approach coupled with nonlinear equations of motion and some maneuvering corrections is unique. The strip theory approximation allows for faster computations and simplified body geometry definition. The result is a hydrodynamic model that allows the prediction of nonlin-

ear loads and motions in a very efficient and robust manner. The theory, numerical methods, validations, and discussion will be broken up as follows.

Chapter II describes the problem formulation. This includes the conventions used, explanation and justification of the assumptions made, and description of the boundary conditions. The coupling between the equations of motion and acceleration potential is described in detail.

Chapter III describes the details of the numerical techniques used, including the discretization of the two-dimensional boundary, time marching and stability, and treatment of the forward speed terms.

Chapter IV presents the two-dimensional results. This includes convergence studies, linear validations, and large amplitude validations.

Chapter V presents the strip theory results for prescribed motions. A variety of hull forms are used to validate the linear hydrodynamic coefficients, exciting forces, and some discussion of large amplitude motions.

Chapter VI validates the equations of motion using the body-exact hydrodynamic model. Small wave amplitudes are used to compare the results to the response amplitude operators of linear theory.

Chapter VII discusses the contributions of this dissertation and possible considerations for future work.

CHAPTER II

Problem Formulation

2.1   Conventions and Coordinate Systems

Three coordinate systems are used in this formulation. They are the earth-fixed, hydrodynamic, and body-fixed frames, indicated by $\mathbf{x_o}, \mathbf{x}, \bar{\mathbf{x}}$, respectively. The earth frame is inertial and used as a global reference frame. The fluid dynamics are solved in the hydrodynamic frame and the rigid body equations are solved in the body frame. In the earth-fixed frame, the $z_o - axis$ points up (i.e. out of the water) while the $x_o - axis$ can point in any horizontal reference direction and the $y_o - axis$ must follow the right-hand coordinate convention. Its origin is arbitrary, so long as the $x_o y_o - plane$ is coincident with the mean water level.

The hydrodynamic frame follows the mean or desired path of the ship. At present, it translates along the x_o axis at a the mean ship velocity, U_o. The hydrodynamic problem is solved in this frame, hence the name. At time $t = 0$, the hydrodynamic frame is coincident with the earth-fixed frame. The body frame is fixed to the ship and is described by three translations and rotations relative to the hydrodynamic frame. The $\bar{x} - axis$ points out the bow, the $\bar{y} - axis$ points to port, and the $\bar{z} - axis$ points up. It's origin is at amidships, along the centerline, and on the calm waterline. In the ship's mean position, the body and hydrodamic frames are coincident. For this reason, the hydrodynmaic frame may also be referred to as the equilibrium frame.
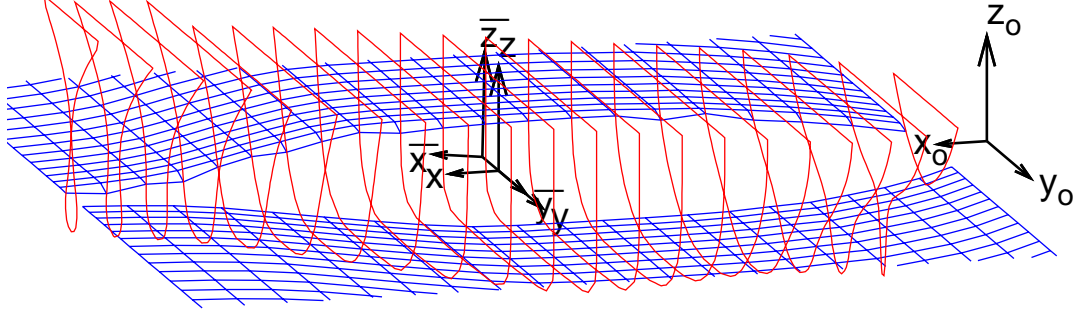
Figure 2.1: Coordinate Systems

The relationship of the three frames to one another is illustrated in Figure 2.1

The use of several reference frames requires a clear and consistent statement about gradients and derivatives. The hydrodynamics and rigid body dynamics are solved in different frames. Bernoulli's equation is derived in the hydrodynamic frame, while the rigid body equations of motion are solved in the body frame.

Three time-derivative conventions are described. The partial ∂, substantial D, and prescribed path δ time-derivates will be used regularly in the derivation of the problem. In terms of the velocity potential, the partial time-derivative, $\frac{\partial \phi}{\partial t}$, is fixed in the hydrodynamic frame. This is the same term as appears in Bernoulli's equation, as written in the hydrodynamic frame. The other time-derivatives are related by

$$\frac{D}{Dt} = \frac{\partial}{\partial t} + \mathbf{u} \cdot \nabla \tag{2.1}$$

$$\frac{\delta}{\delta t} = \frac{\partial}{\partial t} + \mathbf{V} \cdot \nabla \tag{2.2}$$

where $\mathbf{u}$ is the fluid velocity and $\mathbf{V}$ is a prescribed velocity, all in the hydrodynamic frame.

2.2   The Governing Equations

The velocity potential is commonly used in theoretical and numerical fluid mechanics. In marine hydrodynamics, it is has seen many applications because of its simplicity, accuracy, and efficiency. This section starts with a general statement of the conservation laws. Assumptions are made along the way to simplify the equations, ending with the utilization of the velocity potential. The derivation includes vector calculus identities and begins with a statement of conservation of mass for an arbitrary fixed control volume. The Einstein summation convention is used.

$$\frac{D}{Dt}\iiint_V \rho dV = \iiint_V \frac{\partial \rho}{\partial t}dV + \iint_A \rho u_i n_i dA = 0 \tag{2.3}$$

where ρ is the fluid density, u_i and n_i are the ith components of the fluid velocity and unit normal, respectively. The surface integral can be written as a volume integral using the divergence theorem, resulting in

$$\iiint_V [\frac{\partial \rho}{\partial t} + \frac{\partial \rho u_i}{\partial x_i}]dV = 0 \tag{2.4}$$

The conservation of mass holds for *any* volume, therefore the integrand of Eqn. (2.4) must equal zero. We assume the fluid is incompressible and homogeneous everywhere in the domain, reducing to the well known form of the continuity equation.

$$\frac{\partial u_i}{\partial x_i} = \nabla \cdot \mathbf{u} = \mathbf{0} \tag{2.5}$$

The conservation of momentum equations are given by

$$\frac{D}{Dt}\iiint_V \rho u_i dV = \iint_A \tau_{ij} n_j dA + \iiint_V F_i dV \tag{2.6}$$

where τ_{ij} is the stress tensor, and F_i is an external force. The surface integral term in Eqn. (2.6) can be transformed into a volume integral using the divergence theorem. The left hand side of Eqn. (2.6) can be rewritten similarly to Eqn. (2.4)

$$\iiint_V [\frac{\partial \rho u_i}{\partial t} + \frac{\partial \rho u_i u_j}{\partial x_j} - \frac{\partial \tau_{ij}}{\partial x_j} - F_i]dV = 0 \tag{2.7}$$

and since it holds for *any* volume, the integrand in Eqn. (2.7) must equal zero. The stress-strain relation for an incompressible Newtonian fluid is given by

$$\tau_{ij} = -p\delta_{ij} + \mu(\frac{\partial u_i}{\partial x_j} + \frac{\partial u_j}{\partial x_i}) \tag{2.8}$$

where δ_{ij} is the Kronecker delta function ($\delta_{ij} = 1$ if $i = j$, $\delta_{ij} = 0$ if $i \neq j$), p is the pressure, μ is the viscosity of the fluid. This relation can be used to rewrite the third term in Eqn. (2.7)

$$\frac{\partial \tau_{ij}}{\partial x_j} = -\frac{\partial p}{\partial x_i} + \mu \frac{\partial^2 u_i}{\partial x_j \partial x_j} \tag{2.9}$$

The result is a form of the incompressible Navier-Stokes equations, written below using tensor and vector notation

$$\rho \frac{\partial u_i}{\partial t} + \rho u_j \frac{\partial u_i}{\partial x_j} = -\frac{\partial p}{\partial x_i} + \mu \frac{\partial^2 u_i}{\partial x_j^2} + F_i \tag{2.10}$$

$$\rho \frac{\partial \mathbf{u}}{\partial t} + \rho(\mathbf{u} \cdot \nabla)\mathbf{u} = -\nabla p + \mu \nabla^2 \mathbf{u} + \mathbf{F} \tag{2.11}$$

Next, we replace the conservative force $\mathbf{F}$ with a scalar function $\Upsilon = -\rho g z$, such that $\nabla \Upsilon = \mathbf{F}$. The vorticity is given by $\mathbf{\Omega} = \nabla \times \mathbf{u}$ and the following vector identity is used

$$(\mathbf{u} \cdot \nabla)\mathbf{u} = \frac{1}{2}\nabla(\mathbf{u} \cdot \mathbf{u}) - \mathbf{u} \times \mathbf{\Omega} \tag{2.12}$$

For incompressible fluids, the vorticity transport equation is given by

$$\frac{D\boldsymbol{\Omega}}{Dt} = (\boldsymbol{\Omega} \cdot \nabla)\mathbf{u} + \frac{\mu}{\rho}\nabla^2\boldsymbol{\Omega} \tag{2.13}$$

We assume the fluid is inviscid ($\mu = 0$) and starts from rest with ($\boldsymbol{\Omega} = \mathbf{0}$ at $t = 0$). Therefore $\boldsymbol{\Omega}$ will *always* be zero, or the fluid is irrotational. Eqn. (2.11) then simplifies to

$$\frac{\partial \mathbf{u}}{\partial t} + \nabla(\frac{1}{2}\mathbf{u} \cdot \mathbf{u} + \frac{p}{\rho} + gz) = 0 \tag{2.14}$$

Irrotational flows are conveniently described by a scalar function, the velocity potential, Φ, where $\nabla\Phi = \mathbf{u}$.

$$\nabla(\frac{\partial \Phi}{\partial t} + \frac{1}{2}\nabla\Phi \cdot \nabla\Phi + \frac{p}{\rho} + gz) = 0 \tag{2.15}$$

Integrating Eqn. (2.15) in space gives the unsteady form of Bernoulli's equation, for an incompressible, homogeneous, inviscid, irrotational flow

$$\frac{\partial \Phi}{\partial t} + \frac{1}{2}\nabla\Phi \cdot \nabla\Phi + \frac{p}{\rho} + gz = B(t) \tag{2.16}$$

where $B(t)$ is a constant, independent of the space variables, but dependent on time. For completeness, we can rewrite the continuity equation, Eqn. (2.5), using the velocity potential. The result is the recognizable Laplace equation

$$\nabla^2\Phi = 0 \tag{2.17}$$

Eqns. (2.16) and (2.17) are the basis of the potential flow theory. Assuming the fluid is incompressible, homogenous, inviscid, and starts from rest greatly reduces the complexity of the problem. More importantly, the numerical methods to solve problems based on potential flow have proven to be accurate and efficient.

11

The total potential, Φ, can be decomposed into a free stream and perturbation potential, ϕ. The free stream potential is useful when the ship has a mean speed associated with it, such as constant forward speed. The perturbation velocity potential must satisfy Laplace's equation.

$$\Phi(x, y, z, t) = -U_o x + \phi(x, y, z, t) \tag{2.18}$$

$$\nabla^2 \phi(x, y, z, t) = 0 \tag{2.19}$$

The boundary integral problem can be solved once the appropriate boundary conditions have been defined. The total pressure is given by Bernoulli's equation, written in the hydrodynamic frame. We can assume the atmospheric pressure is zero. The Bernoulli constant is determined by finding the pressure far away from the body on $z = 0$, such that $B(t) = \frac{1}{2}U_o^2$.

$$p = -\rho\left(\frac{\partial \phi}{\partial t} + \frac{1}{2}|\nabla \phi|^2 - U_o\frac{\partial \phi}{\partial x} + gz\right) \tag{2.20}$$

This derivation assumes that the hydrodynamic frame translates at a constant velocity, U_o, along the x_o direction and is therefore inertial. An alternative formulation may be derived, including an accelerating or rotating hydrodynamic frame, but will result in a different form of Bernoulli's equation.

2.3   Strip Theory Approximation

The hull surface can be defined by $y = \pm b(x, z)$. Three-dimensional unit normals to the body surface can be found as

$$\mathbf{n} = (n_1, n_2, n_3) = \frac{(b_x, \mp 1, b_z)}{\sqrt{b_x^2 + 1 + b_z^2}} \tag{2.21}$$

where the normal direction points into the body, and $b_x = \frac{\partial b}{\partial x}$, $b_z = \frac{\partial b}{\partial z}$. It is convenient to define $(n_4, n_5, n_6) = \mathbf{r} \times \mathbf{n}$ where $\mathbf{r}$ is a position vector from a ship-fixed origin pointing to a node on the hull surface. The forces and moments on the ship can be found by integrating the pressure around the instantaneous hull wetted surface.

$$F_j = \iint_S p n_j dS \qquad (2.22)$$

Under the slender-body assumption, the length (L) is large compared to the beam (B) and draft (T) of the vessel, or $L = O(1); B, T = O(\epsilon)$, where ϵ is some small parameter. Therefore, $b_x << (1, b_z)$, the strip theory unit normals are given by

$$\mathbf{N} = (N_1, N_2, N_3) = \frac{(b_x, \mp 1, b_z)}{\sqrt{1 + b_z^2}} \qquad (2.23)$$

where the two-dimensional unit normal, $(0, N_2, N_3)$, has unity magnitude and is used to satisfy the two-dimensional body boundary conditions. N_1 is a fictitious normal in the $x-$direction, used to solve the surge problem. It is useful to define (N_4, N_5, N_6) as

$$(N_4, N_5, N_6) = \mathbf{r} \times \mathbf{N} \qquad (2.24)$$

where $\mathbf{r}$ is the position vector of the node, as defined earlier.

The exact forces and moments can be rewritten in terms of the parametrically defined hull surface, where $dS = \sqrt{b_x^2 + 1 + b_z^2} dx dz$

$$F_j = \iint_A p n_j \sqrt{b_x^2 + 1 + b_z^2} dx dz \qquad (2.25)$$

and we write dz in terms of the two-dimensional definition

$$\frac{dz}{dl} = \frac{-N_2}{1} \Rightarrow dz = \frac{dl}{\sqrt{1 + b_z^2}} \qquad (2.26)$$

13

where dl is the integration variable along the tangential direction of the two-dimensional hull section contour.

Now, we can separate the integral into an integral along the contour C_H, defining the wetted two-dimensional hull section, and L, along the length of the ship

$$F_j = \int\limits_L dx \int\limits_{C_H} pn_j \frac{\sqrt{b_x^2 + 1 + b_z^2}}{\sqrt{1 + b_z^2}} dl \qquad (2.27)$$

recalling that $b_x = \frac{-n_1}{n_2}$ and $b_z = \frac{-n_3}{n_2}$

$$F_j = \int\limits_L dx \int\limits_{C_H} pn_j \frac{\sqrt{n_1^2 + n_2^2 + n_3^2}}{\sqrt{n_2^2 + n_3^2}} dl = \int\limits_L dx \int\limits_{C_H} pn_j \frac{1}{\sqrt{1 - n_1^2}} dl \qquad (2.28)$$

which is an approximation if only n_j is used. Since the two-dimensional normals N_j, defined in Eqn. 2.23, scale n_j by exactly this amount, no approximation has been made in the integration of the pressure.

$$n_j = N_j \sqrt{1 - n_1^2} \qquad (2.29)$$

$$F_j = \int\limits_L dx \int\limits_{C_H} pN_j dl \qquad (2.30)$$

However, the pressure p comes from the exact solution of the three-dimensional boundary value problem. We further use the slender-body assumption to reduce the three-dimensional Laplace equation into a series of two-dimensional problems, to leading order. Each two-dimensional problem must satisfy the Laplace equation on each transverse strip. For simplicity of notation, the potential ϕ will refer to the

14

two-dimensional value from here onward.

$$\phi \equiv \phi(y, z, t; x) \tag{2.31}$$

$$\nabla^2 \phi(y, z, t; x) = 0 \tag{2.32}$$

$$p = -\rho(\frac{\partial \phi}{\partial t} - U_o \frac{\partial \phi}{\partial x} + \frac{1}{2}|\nabla \phi|^2 + gz) \tag{2.33}$$

Eqn. (2.33) is an approximation of Eqn. (2.20), since it is based on the solution of the two-dimensional potential. The details of the components in the the pressure equation (2.33) will be discussed in the following sections.

2.4   Boundary Integral Method

We can use Green's theorem to write the fluid problem as a set of boundary integral equations, solving the two-dimensional problem. We use the source distribution method in this formulation, where the perturbation potential is given by

$$\phi(\mathbf{x}) = \int_C \sigma(\boldsymbol{\xi}) G(\mathbf{x}; \boldsymbol{\xi}) dC \tag{2.34}$$

where C is the contour defining the perimeter of the two-dimensional boundary, $\mathbf{x}$ is a point anywhere in the fluid, and $\boldsymbol{\xi}$ are source points located on the boundary C, with some unknown strength σ. C includes all the contours or boundaries surrounding the fluid domain. G is a Green function that satisfies the Laplace equation. The two-dimensional Rankine source Green function used is

$$G(\mathbf{x}; \boldsymbol{\xi}) = \ln |\mathbf{x} - \boldsymbol{\xi}| \tag{2.35}$$

15

and has the following properties

$$\nabla^2 G = 2\pi\delta(\mathbf{x} - \boldsymbol{\xi}) \tag{2.36}$$

$$\nabla G \to 0 \quad \text{as} \quad \mathbf{x} \to \infty \tag{2.37}$$

where δ is the Dirac delta function. The source strength must be found such that the appropriate boundary conditions are satisfied. Numerically, an influence matrix can be determined where the discretized boundary elements have prescribed boundary conditions, and the source strengths can be determined. Once these are known, the potential and its spatial derivatives can be computed using the given Green function. Details are discussed in the next chapter.

2.5   Velocity Potential Decomposition

The perturbation potential on each section is broken up into four components

$$\phi(y, z, t; x) = \phi^I + \phi^D + \phi^R + \phi^A$$

where $\qquad \phi^I = \qquad$ incident wave potential, known *a priori*

$\qquad\qquad\quad \phi^D = \qquad$ diffracted potential

$\qquad\qquad\quad \phi^R = \qquad$ radiated potential

$\qquad\qquad\quad \phi^A = \qquad$ non-zero angle potential

In the earth-fixed frame, the incident potential and elevation, linearized about $z = 0$, are given by

$$\phi^I = \frac{iga}{\omega_o}e^{-ik(x_o cos\beta + y_o sin\beta)}e^{iw_o t}e^{kz} \tag{2.38}$$

$$\eta^I = ae^{-ik(x_o cos\beta + y_o sin\beta)}e^{iw_o t} \tag{2.39}$$

16

where a is the wave amplitude, ω_o is the absolute wave frequency, $k = \frac{2\pi}{\lambda}$ is the wave number corresponding to a wavelength λ, and β is the heading angle, the angle of the wave propagation relative to ship heading. $\beta = 180^o$ is the case of head seas, for example. Since the incident wave is defined analytically, so are the values of its derivatives in space and time, which are needed for boundary conditions and to find the incident wave, or Froude-Krylov, pressure.

The resulting exact body boundary conditions are re-written in two-dimensions using the strip theory approach

$$\mathbf{N}\cdot\nabla\phi^D = -\mathbf{N}\cdot\nabla\phi^I \quad \text{on} \quad C_H \tag{2.40}$$

$$\mathbf{N}\cdot\nabla\phi^R = \sum_{i=1}^{6} v_i N_i \quad \text{on} \quad C_H \tag{2.41}$$

$$\mathbf{N}\cdot\nabla\phi^A = U_o(-\eta_6 N_2 + \eta_5 N_3) \quad \text{on} \quad C_H \tag{2.42}$$

where $v_i = (v_1, v_2, v_3, \omega_1, \omega_2, \omega_3)$ includes the three translational and rotational velocities of the body. The terms on the right-hand sides of Eqns. (2.40) and (2.41) represent the instantaneous velocity of the fluid in order to satisfy the corresponding body boundary conditions. The terms on the right-hand side of Eqn. (2.42) are the two-dimensional corrections when there is a non-zero pitch angle, η_5, or non-zero yaw angle, η_6, in the case of forward speed. This correction assumes small angles relative to the hydrodynamic frame, such that $sin(\eta_{5,6}) \approx \eta_{5,6}$.

2.6 Mixed Boundary Value Problem

The exact two-dimensional body boundary conditions are given in Eqns. (2.40) through (2.42). Each of these potentials must satisfy the same set of remaining boundary conditions. On the mean free surface, the linearized kinematic and dynamic

free surface boundary conditions are used to march the free surface in time

$$\left(\frac{\partial}{\partial t} - U_o\frac{\partial}{\partial x}\right)\zeta = \frac{\partial \phi}{\partial z} \qquad \text{on} \quad C_F \qquad (z = 0) \tag{2.43}$$

$$\left(\frac{\partial}{\partial t} - U_o\frac{\partial}{\partial x}\right)\phi = -g\zeta \qquad \text{on} \quad C_F \qquad (z = 0) \tag{2.44}$$

where $z = \zeta(y, t; x)$ is the free surface elevation, g is the acceleration due to gravity, and C_F is the contour defining the free surface, or $z = 0$ in this linearized case. Consistent with strip theory, we assume the encounter frequency is high, $\frac{\partial}{\partial t} >> U_o\frac{\partial}{\partial x}$, and ignore the downstream free surface effects resulting in

$$\frac{\partial \zeta}{\partial t} = \frac{\partial \phi}{\partial z} \qquad \text{on} \quad C_F \qquad (z = 0) \tag{2.45}$$

$$\frac{\partial \phi}{\partial t} = -g\zeta \qquad \text{on} \quad C_F \qquad (z = 0) \tag{2.46}$$

The velocity potential is known on the mean free surface. In the far field, a radiation boundary condition is imposed such that only the incident waves are incoming. This is done numerically by incorporating an outer "beach" region, with exponentially increasing node spacing, that absorbs outgoing waves. Also, the water is assumed deep and the gradient of the perturbation potential vanishes as $z \to -\infty$. This condition is automatically satisfied by the selection of the Green function, G, given in Eqn. (2.35). The incident wave potential is known, while the other potentials must be computed. They are initially set to zero and the dynamics (ship motions or incident wave elevation) are gradually increased using a linear or hyperbolic tangent ramp function. Figure 2.2 presents a schematic of the two-dimensional boundary value problem. Once the mixed boundary value problem is solved, the velocity potential and its derivatives can be determined anywhere in the fluid domain. The pressure on the body can be determined by using Eqn. (2.33). The free surface conditions are stepped in time using Eqns. (2.45) and (2.46).

Two-Dimensional Body-Exact Computation Model

Free Surface Conditions

$$\frac{\partial \phi}{\partial t} = -g\zeta, \quad \frac{\partial \zeta}{\partial t} = \frac{\partial \phi}{\partial z}$$

applied on z=0

$$dy_{out_i} = dy_{in} * 1.0378^{\frac{i(i-1)}{2}}, i = 1..20$$

outer domain

z

outer domain

y

+ sources
• nodes

FSBC $\quad \phi \quad$ on z=0

BBC $\quad \dfrac{\partial \phi}{\partial N} \quad$ on exact body

panel distribution on exact position of body

Laplace

Deep Water $\quad \nabla \phi \to 0 \quad$ as $\quad z \to -\infty$
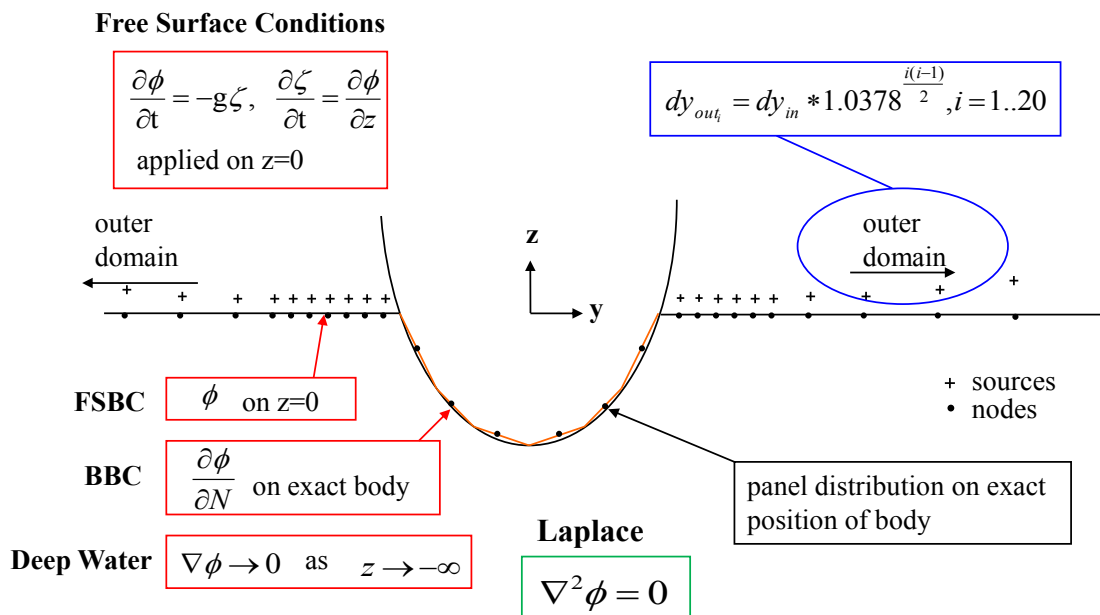
$$\nabla^2 \phi = 0$$

Figure 2.2: Two-Dimensional Boundary Value Problem

2.7 Forces and Moments

The forces and moments on the body are given by

$$\mathbf{F} = \int_L dx \int_{C_H} p\mathbf{N} \, dl \tag{2.47}$$

$$\mathbf{M} = \int_L dx \int_{C_H} p\mathbf{r} \times \mathbf{N} \, dl \tag{2.48}$$

and the pressure p, given by Eqn. (2.33), can be separated into hydrostatic and hydrodynamic components

$$p = p^{HS} + p^{DYN} \tag{2.49}$$

$$p^{HS} = -\rho g z \tag{2.50}$$

$$p^{DYN} = p^I + p^D + p^R + p^A + p^S \tag{2.51}$$

where p^I, p^D, p^R, p^A are first-order, $-\rho(\frac{\partial \phi}{\partial t} - U_o \frac{\partial \phi}{\partial x})$, terms of the incident (also called Froude-Krylov), diffracted, radiated, and angle components of the pressure. p^S is the second-order term, $-\rho \frac{1}{2} |\nabla \phi|^2$, and includes the entire perturbation velocity, $\nabla \phi$, from all the components.

After the two-dimensional mixed boundary value problems have been solved, ϕ and $\nabla \phi$ of each component can be found anywhere in the domain. The $\frac{\partial \phi}{\partial x}$ term is not solved for since it is not a part of the two-dimensional problem, and must be estimated numerically. This can be done by numerical differentiation or using interpolation schemes, such as radial basis functions. More details will be given in Chapter III.

The proposed pressure formulation solves for $\frac{\partial \phi}{\partial t}$ directly, instead of numerically differentiating, as will be discussed later. An advantage of this method is that it is not sensitive to the time-step size when computing the pressure on the body, since

$\frac{\partial \phi}{\partial t}$ is solved for directly. Another advantage is that this method is robust for large amplitude motions and indifferent to panel variations between time-steps.

An alternative to the pressure formulation is the momentum formulation, which is computationally less expensive but seems to have problems for larger amplitudes when then sectional areas change. A summary is presented in Appendix A, including its origins, a brief derivation, and a sample case where the formulation breaks down.

2.8 Equations of Motion

The equations are set up by determining the vessels position and velocity, including rotational effects. The time-derivatives of these values, along with the forces acting on the vessel, are necessary to drive the equations of motion. The formulation followed here uses the conventions similar to those found in Fossen (1991) and Fossen (1994). The vessel's location and orientation can be described by three translations and three rotations, given by η_i. The coordinates are in the hydrodynamic frame and the rotations are Euler angles. The vessel's linear and angular velocity are described in the body-fixed frame, given by v_i. The forces and moments on the vessel are described in the body-fixed frame, given by F_i.

$$\eta_i = [\eta_1, \eta_2, \eta_3, \eta_4, \eta_5, \eta_6]^T \tag{2.52}$$

$$v_i = [v_1, v_2, v_3, \omega_1, \omega, \omega_3]^T \tag{2.53}$$

$$F_i = [F_1, F_2, F_3, M_1, M_2, M_3]^T \tag{2.54}$$

The equations of motion are then be given by

$$\sum_{j=1}^{6} [M_{ij} + M_{ij}^*]\dot{v}_j = F_i^{HS} + F_i^I + F_i^D + F_i^{R*} + F_i^A + F_i^S + F_i^{EXT} \tag{2.55}$$

$$\dot{\eta}_i = [T]v_j \tag{2.56}$$

where

$$M_{ij} \qquad \text{is the rigid body mass matrix}$$

$$M_{ij}^* \qquad \text{is the radiation impulsive added mass matrix}$$

$$F_i^{HS} \qquad \text{are the hydrostatic forces and moments}$$

$$F_i^{I} \qquad \text{are the incident (Froude-Krylov) forces and moments}$$

$$F_i^{D} \qquad \text{are the diffraction forces and moments}$$

$$F_i^{R*} \qquad \text{are the radiation memory forces and moments}$$

$$F_i^{A} \qquad \text{are the angle of attack forces and moments}$$

$$F_i^{S} \qquad \text{are the second-order forces and moments}$$

$$F_i^{EXT} \qquad \text{are the external forces and moments}$$

$$T \qquad \text{is a transformation matrix}$$

$$T = \begin{bmatrix} T_1 & 0_{3x3} \\ 0_{3x3} & T_2 \end{bmatrix}$$

$$T_1 = \begin{bmatrix} c5c6 & -c4s6 + s4s5c6 & s4s6 + c4s5c6 \\ c5s6 & c4c6 + s4s5s6 & -s4c6 + c4s5s6 \\ -s5 & s4c5 & c4c5 \end{bmatrix}$$

$$T_2 = \begin{bmatrix} 1 & s4t5 & c4t5 \\ 0 & c4 & -s4 \\ 0 & s4/c5 & c4/c5 \end{bmatrix}$$

where s, c, t are sine, cosine, and tangent, respectively, and 4, 5, 6 are η_4, η_5, η_6, respectively. The inverses of T_1 and T_2 can be found, allowing the transformation of hydrodynamic frame velocities into the body-fixed frame. It is worth noting that

$T_1^{-1} = T_1^T$, but $T_2^{-1} \neq T_2^T$ since the Euler angle rates are not orthogonal.

The radiation terms, M_{ij}^* and F_i^{R*}, arise from the fact that the acceleration potential is used to move the body acceleration dependent component of the force to the other side of the rigid body equations of motion. The derivation of this term is described in the next section.

2.9 The Acceleration Potential

The "acceleration potential", given by ψ, is defined as $\psi = \frac{\partial \phi}{\partial t}$. Its use in this formulation is driven by two motivations. First, it allows the direct solution of the $\frac{\partial \phi}{\partial t}$ term in the pressure equation (2.33). This is very beneficial when using the body-exact approach, as the time-derivative of the potential is solved for at each time-step. This avoids numerical difficulties with repanelization techniques and using finite differencing schemes. Some examples of this are given later.

The second motivation of this method is that the acceleration potential can be written in terms of the body acceleration, $\dot{v}_i$. Since this is an unknown, special care may be taken to move this term to the other side of the rigid body equations of motion. Similar work has been done by Vinje and Brevig (1981) and Kang and Gong (1990), including applications of prescribed motions. Beck et al. (1994) present a similar method, including an iterative method to solve for the body acceleration. Tanizawa (1995) and van Daalen (1993) discuss the special case of the acceleration potential and how it couples to the rigid body equations of motion.

The objective is to set up a boundary value problem for the acceleration potential, as was done for the velocity potential, since the acceleration potential also satisfies the Laplace equation. The appropriate boundary conditions must be determined. The deep water and far field conditions are the same as described for the velocity potential. The free surface condition requires a knowledge of $\frac{\partial \phi}{\partial t}$ on $z = 0$. This is known from the linearized free surface conditions, Eqns. (2.45) and (2.46). The

corresponding body boundary conditions are more difficult to derive, as they involve time-derivatives in the hydrodynamic and body frames.

The body boundary conditions given in Eqns. (2.40) through (2.42) are used, and the appropriate time-derivatives are taken. Two identities are used in this derivation.

$$\frac{\delta}{\delta t} = \frac{\partial}{\partial t} + \mathbf{V} \cdot \nabla \tag{2.57}$$

$$(\frac{\partial}{\partial t})_{hydrodnymic} = (\frac{\partial}{\partial t})_{body} + \boldsymbol{\omega} \times \tag{2.58}$$

where $\mathbf{V}$ is the body node velocity, given by $\mathbf{V} = \mathbf{v} + \boldsymbol{\omega} \times \mathbf{r}$, and $\frac{\delta}{\delta t}$ is the time-derivative, in the body frame, following the body node. The second equation relates time-derivatives between two frames.

The diffraction body boundary condition is found by partial differentiation with respect to time, in the hydrodynamic frame, of Eqn. (2.40)

$$\frac{\partial}{\partial t}(\mathbf{N} \cdot \nabla \phi^D) = \frac{\partial}{\partial t}(-\mathbf{N} \cdot \nabla \phi^I) \tag{2.59}$$

the chain rule is applied, and Eqn. (2.58) is applied to the unit normals. Realizing that $(\frac{\partial \mathbf{N}}{\partial t})_{body} = 0$, the resulting equation is

$$\mathbf{N} \cdot \nabla \psi^D = -\mathbf{N} \cdot \nabla \psi^I - (\boldsymbol{\omega} \times \mathbf{N}) \cdot (\nabla \phi^D + \nabla \phi^I) \quad \text{on} \quad C_H \tag{2.60}$$

The radiation body boundary condition is found by taking the time-derivative of Eqn. (2.41) in the body frame, following the node.

$$\frac{\delta}{\delta t}(\mathbf{N} \cdot \nabla \phi^R) = \frac{\delta}{\delta t}(\mathbf{V} \cdot \mathbf{N}) = \frac{\delta}{\delta t}[\mathbf{v} \cdot \mathbf{N} + \boldsymbol{\omega} \cdot (\mathbf{r} \times \mathbf{N})] \tag{2.61}$$

24

and since $(\frac{\delta \mathbf{N}}{\delta t})_{body} = 0$, the left and right-hand sides can be rewritten

$$(\frac{\delta}{\delta t})_{body}(\mathbf{v} \cdot \mathbf{N} + \boldsymbol{\omega} \cdot (\mathbf{r} \times \mathbf{N})) = \dot{\mathbf{v}} \cdot \mathbf{N} + \dot{\boldsymbol{\omega}} \cdot (\mathbf{r} \times \mathbf{N}) \qquad (2.62)$$

$$(\frac{\delta}{\delta t})_{body}(\mathbf{N} \cdot \nabla \phi^R) = \mathbf{N} \cdot [(\frac{\partial}{\partial t})_{body}(\nabla \phi^R) + (\mathbf{V} \cdot \nabla)\nabla \phi^R] \qquad (2.63)$$

$$\text{where} \qquad (\frac{\partial}{\partial t})_{body}(\nabla \phi^R) = (\frac{\partial}{\partial t})_{hydrodynamic}(\nabla \phi^R) - \boldsymbol{\omega} \times (\nabla \phi^R) \qquad (2.64)$$

resulting in

$$\mathbf{N} \cdot \nabla \psi^R = \dot{\mathbf{v}} \cdot \mathbf{N} + \dot{\boldsymbol{\omega}} \cdot (\mathbf{r} \times \mathbf{N}) - (\boldsymbol{\omega} \times \mathbf{N}) \cdot \nabla \phi^R - \mathbf{N} \cdot (\mathbf{V} \cdot \nabla)\nabla \phi^R \quad \text{on} \quad C_H \quad (2.65)$$

The angle of attack body boundary condition is derived similarly to the radiation condition, by taking the body frame time-derivative of Eqn. (2.42).

$$\frac{\delta}{\delta t}(\mathbf{N} \cdot \nabla \phi^A) = \frac{\delta}{\delta t}(U_o(-\eta_6 N_2 + \eta_5 N_3)) \qquad (2.66)$$

and, assuming U_o to be constant, results in

$$\mathbf{N} \cdot \nabla \psi^A = -(\boldsymbol{\omega} \times \mathbf{N}) \cdot (\nabla \phi^A - \mathbf{U_o}) \quad \text{on} \quad C_H \qquad (2.67)$$

where $\mathbf{U_o} = (U_o, 0, 0)$ for the case of constant forward speed.

Eqns. (2.60), (2.65), and (2.67) are the equivalent diffraction, radiation, and angle body boundary conditions for the acceleration potential. The right-hand sides of these equations can all be determined once the ϕ problem is solved. The result is a mixed boundary value problem for ψ written in the hydrodynamic frame.

At this point, the acceleration potential has been described such that the $\frac{\partial \phi}{\partial t}$ term in the pressure equation (2.33) can be solved for directly. This next step is to move the body acceleration terms, $\dot{\mathbf{v}}$ and $\dot{\boldsymbol{\omega}}$, to the other side of the rigid body equations of motion. This is done by splitting the radiation acceleration potential

25

into two components, impulsive ($\psi^{R,I}$) and memory ($\psi^{R,M}$), subject to the following boundary conditions.

$$\psi^R = \psi^{R,I} + \phi^{R,M} \tag{2.68}$$

$$\mathbf{N}\cdot\nabla\psi^{R,I} = \dot{\mathbf{v}}\cdot\mathbf{N} + \dot{\boldsymbol{\omega}}\cdot(\mathbf{r}\times\mathbf{N}) \quad \text{on} \quad C_H \tag{2.69}$$

$$\mathbf{N}\cdot\nabla\psi^{R,M} = -(\boldsymbol{\omega}\times\mathbf{N})\cdot\nabla\phi^R - \mathbf{N}\cdot(\mathbf{V}\cdot\nabla)\nabla\phi^R \quad \text{on} \quad C_H \tag{2.70}$$

$$\psi^{R,I} = 0 \quad \text{on} \quad C_F \tag{2.71}$$

$$\psi^{R,M} = \psi^R \quad \text{on} \quad C_F \tag{2.72}$$

Combining the boundary conditions, we recover the original radiation acceleration potential problem. For simplicity of notation, let $\chi \equiv \psi^{R,I}$. This impulsive problem, which is only a function of the body accelerations, is further reduced into six canonical problems.

$$\chi = \sum_{i=1}^{6} \dot{v}_i \chi_i \tag{2.73}$$

where $\dot{v}_i$ and χ_i are the acceleration and the scaled acceleration potential, due to a unit body acceleration, in the ith mode of motion. They must satisfy the following boundary conditions

$$\mathbf{N}\cdot\nabla\chi_i = N_i \quad \text{for} \quad i = 1..6 \quad \text{on} \quad C_H \tag{2.74}$$

$$\chi_i = 0 \quad \text{for} \quad i = 1..6 \quad \text{on} \quad C_F \tag{2.75}$$

The solution of this boundary value problem is where the M_{ij}^* and F_i^{R*} terms originate. The $\psi^{R,M}$ solution goes into the pressure equation and is then integrated around the entire body, resulting in an expression for F_i^{R*} that *excludes* the body acceleration component. The solution of χ_i everywhere on the body can be used to find the radiation impulsive added mass matrix, M_{ij}^*, and the components are given

by

$$M_{ij}^* = \rho \int_L dx \int_{C_H} \chi_j N_i \, dl \qquad (2.76)$$

Breaking down the radiation acceleration potential in such a way allows moving the unknown body acceleration terms to the other side of the equations of motion, as given in Eqn. 2.55. This reduces numerical instabilities and increases accuracy in the coupled hydrodynamic and rigid body equations.

2.10 Viscous Forces

The effects of viscosity are not captured in potential flow theory. Usually these effects are small enough that ignoring viscosity is justified. However, there are instances where they must be included, such as additional viscous roll damping. The model used in this formulation is that of Himeno (1981), where emprical corrections are added for viscosity. The amount of additional damping is dependent on the hull form or section shape, and is usually determined from experimental results.

Besides viscous roll damping, other motions must be considered. Surge, sway, and yaw have no restoring mechanisms. Adding viscous damping terms in those degrees of freedom is important, especially in the case of free motions, where the vessel may drift off. Especially important is the case of zero encounter frequency, where potential flow predicts zero damping. The maneuvering equations and coefficients suggest otherwise, because they include viscous effects. The goal is to include these effects in a viscous forcing model, while not "double counting" the potential flow results.

An approach to solve this problem is discussed by Bailey et al. (1998). They include an additional damping component, due to viscosity, based on the assumption that $B_{22} = -Y_v$ and $B_{66} = -N_r$ at the zero frequency limit. B_{22} and B_{66} are the sway-sway and yaw-yaw damping coefficients in seakeeping theory, respectively. Y_v and N_r are the sway-sway and yaw-yaw stability derivatives in maneuvering theory,

respectively. Bailey et al. (1998) propose a linear ramp function, up to some limiting frequency, where this viscous term is simply added to the potential flow results. Fossen and Smogeli (2004) and Fossen (2005) present a similar approach, but extend it to all six degrees of freedom by adding a viscous addition to all the diagonal terms of the damping matrix.

The simplified method used here resembles that in Bailey et al. (1998). Additionally, we use a semi-empirical method for calculating the stability derivatives of interest. As discussed by Clarke et al. (1983), the hull is assumed to be a low aspect ratio wing and the maneuvering coefficients are a function of the length to draft ratio of the ship. A more advanced method includes regression analysis to develop empirical formulas to correct the simplified coefficients.

$$Y'_v = C_o(A_1 + B_1) \tag{2.77}$$

$$Y'_r = C_o(A_2 + B_2) \tag{2.78}$$

$$N'_v = C_o(A_3 + B_3) \tag{2.79}$$

$$N'_r = C_o(A_4 + B_4) \tag{2.80}$$

$$\text{where} \quad C_0 = -\pi \left(\frac{T}{L}\right)^2 \tag{2.81}$$

$$A_1 = 1.0 \qquad B_1 = 0.4 C_B \frac{B}{T} \tag{2.82}$$

$$A_2 = -0.5 \qquad B_2 = 2.2 \frac{B}{L} - 0.08 \frac{B}{T} \tag{2.83}$$

$$A_3 = 0.5 \qquad B_3 = 2.4 \frac{T}{L} \tag{2.84}$$

$$A_4 = 0.25 \qquad B_4 = 0.039 \frac{B}{T} - 0.56 \frac{B}{L} \tag{2.85}$$

where L, B, T, C_B are the length, beam, draft, and block coefficient of the hull. The A_i coefficients come from the low aspect ratio wing theory, and the B_i coefficients come the linear regression analysis of the velocity derivatives. The dimensional values

	Y_v'	Y_r'	N_v'	N_r'
Low AR wing (B coeff =0)	-0.01025	0.00513	-0.00513	-0.00256
Semi-empirical	-0.01743	0.00396	-0.00653	-0.00274
Experiments	-0.0164	0.00291	-0.00691	-0.0032

Table 2.1: Series 60 CB=0.7 Sway and Yaw Maneuvering Coefficients

of these coefficients are given by

$$Y_v = Y_v' 0.5\rho L^2 U \tag{2.86}$$

$$Y_r = Y_r' 0.5\rho L^3 U \tag{2.87}$$

$$N_v = N_v' 0.5\rho L^3 U \tag{2.88}$$

$$N_R = N_r' 0.5\rho L^4 U \tag{2.89}$$

where ρ is the fluid density and U is approximated to be the mean ship speed, or U_o.

The Series-60 hull (with 0.7 block coefficient) is used to check this semi-emperical method. The comparisons between the predicted values using low aspect ratio wing theory, the semi-emperical method (low aspect ratio plus regression), and experimental results are shown in Table 2.1.

The results indicate that the semi-emperical formulation improves the estimate of the coefficients. These estimates do not have to be exact. The maneuvering coefficients are added to the potential flow damping up to a certain frequency, ω_v, using a linear ramp. Fossen and Smogeli (2004) use the following

$$F_{i,visc} = -B_{ii,visc} v_i (1 - \frac{\omega_e}{\omega_v}), \quad \omega_e \leq \omega_v \tag{2.90}$$

$$F_{i,visc} = 0, \quad \omega_e > \omega_v \tag{2.91}$$

for $i = 2, 6$ or in sway, and yaw, and $B_{22,visc} = -Y_v$, $B_{66,visc} = -N_r$. ω_v is based on comparing the potential flow damping coefficients with experiments, and can be given by the non-dimensional value of 12.5, or $\omega_v = 12.5\sqrt{\frac{g}{L}} \approx 3rad/s$ for the S-175,

for example. This gives a form of a viscous force that can be added to the rigid body equations of motion, as presented earlier.

CHAPTER III

Numerical Techniques

3.1 Source Distribution Method

At each time-step a mixed boundary value problem must be solved; the potential is given on the free surface and the normal derivative of the potential is given on the body surface. In this formulation, the source distribution technique is used. Desingularized sources are used to model the free surface, while constant strength flat panels are used to model the body wetted surface. The potential at any point in the fluid domain can be found by

$$\phi_i = \sum_{C_F} \sigma_j G(\mathbf{x}_i; \boldsymbol{\xi}_j) + \int_{C_H} \sigma_j G(\mathbf{x}_i; \boldsymbol{\xi}_j) dl \qquad (3.1)$$

where ϕ_i can be the velocity or acceleration potential at some field point, $\mathbf{x}_i$, anywhere in the domain. $\boldsymbol{\xi}_j$ is the location of a source point with corresponding source strength σ_j. The first term on the right-hand side of Eqn. (3.1) is the summation of the influence of the isolated desingularized sources on the free surface, while the second term includes the integral over the panels on the body. $G(\mathbf{x}_i; \boldsymbol{\xi}_j)$ is a Rankine source

Green function

$$G(\mathbf{x}_i; \boldsymbol{\xi}_j) = \ln r \tag{3.2}$$

$$r = |\mathbf{x}_i - \boldsymbol{\xi}_j| \tag{3.3}$$

where r is the distance between a field point and a source point

Applying the boundary conditions and using Eqn. (3.1), the integral mixed bound-ary value equations can be discretized to form a system of linear equations, shown in Eqns. (3.4) and (3.5). On the free surface, desingularized sources are distributed outside of the domain such that the the source points never coincide with collocation or node points, avoiding singularities. Isolated sources are used rather than a distri-bution, reducing the complexity of the influence matrix. The desingularized distance is given by the square root of the local mesh size.

$$\sum_{C_F} \sigma_j \ln |\mathbf{x}_i - \boldsymbol{\xi}_j| + \int_{C_H} \sigma_j \ln |\mathbf{x}_i - \boldsymbol{\xi}_j| dl = \phi_i \quad \mathbf{x}_i \in C_F \tag{3.4}$$

$$\sum_{C_F} \sigma_j \frac{\partial \ln |\mathbf{x}_i - \boldsymbol{\xi}_j|}{\partial N} + \int_{C_H} \sigma_j \frac{\partial \ln |\mathbf{x}_i - \boldsymbol{\xi}_j|}{\partial N} dl = \frac{\partial \phi_i}{\partial N} \quad \mathbf{x}_i \in C_H \tag{3.5}$$

where $\mathbf{x}_i$ = a point on the boundary of the domain

$\boldsymbol{\xi}_j$ = a source point

σ_j = the source strength

ϕ_i = the given potential on the free surface

$\frac{\partial \phi_i}{\partial N}$ = the given normal derivative of the potential on the body

C_F = the free surface contour

C_H = the hull contour

$\frac{\partial}{\partial N}$ = $\mathbf{N} \cdot \nabla$

The body surface is modeled using panels, which are more suitable for arbitrarily shaped bodies. The resulting discretized equations are given by

$$\sum_{j=1}^{N_F} \sigma_j \ln |\mathbf{x}_i - \boldsymbol{\xi}_j| + \sum_{j=1}^{N_B} \sigma_j \int_{\Delta l_j} \ln |\mathbf{x}_i - \boldsymbol{\xi}_j| dl = \phi_i \quad \mathbf{x}_i \in C_F \tag{3.6}$$

$$-\pi \sigma_i + \sum_{j=1}^{N_F} \sigma_j \frac{(\mathbf{x}_i - \boldsymbol{\xi}_j) \cdot \mathbf{N}_i}{|\mathbf{x}_i - \boldsymbol{\xi}_j|^2} + \sum_{j=1, j \neq i}^{N_B} \sigma_j \int_{\Delta l_j} \frac{(\mathbf{x}_i - \boldsymbol{\xi}_j) \cdot \mathbf{N}_i}{|\mathbf{x}_i - \boldsymbol{\xi}_j|^2} dl = \frac{\partial \phi_i}{\partial N} \quad \mathbf{x}_i \in C_H \tag{3.7}$$

where $\mathbf{N}_i$ is the unit normal on body panel i, N_F is the number of free surface nodes, and N_B is the number of body nodes.

Eqns. (3.6) and (3.7) can be written in matrix form, $A_{ij} \sigma_j = b_i$, where A_{ij} is the influence matrix, determined by the left hand sides of the equations, σ_j are the unknown source strengths, and b_i is the right-hand side of the equations. The matrix is inverted using Gaussian elimination and the source strengths can be determined.

Once the source strengths are known, the potential and its derivatives can be computed anywhere in the domain. In particular, we are interested in ϕ and its

gradients on the body and free surface boundaries. Similar influence matrices can be set up to determine these values, given the source strengths. Details can be found in Appendix B. This approach can be used to solve the velocity potential or acceleration potential, including each of the individual components.

The case of a deeply submerged body can be used as a preliminary validation of the influence matrices. There is no free surface and the velocity potential can often be given analytically, depending on the body shape. Appendix C provides a detailed verification of the influence matrices derived in Appendix B, using a known analytic solution for the velocity potential for the case of a deeply submerged circular section. Some interesting results arise, suggesting that a constant strength flat panel method cannot be used to compute the second space derivatives of the velocity potential on the body. These values are required to set up the boundary value problem for the radiation acceleration potential, given in Eqn. (2.65). The alternative is to numerically estimate these values using the fluid velocity, or $\nabla\phi$, on adjacent panels and differentiate them along the tangential direction. Details and validations are presented in Appendix C.

3.2 Domain Discretization

There are a variety of ways to discretize the domain boundaries, depending on the problem being addressed. In this formulation the free surface is broken up into an inner and outer region, where the inner region resolves the waves and the outer region is used as a numerical beach. For single frequency oscillations at ω, the inner region can span several wavelengths on either side of the body, where the wavelength is given by the deep water dispersion relation, $\lambda = \frac{2\pi g}{\omega^2}$. To resolve the radiated waves, typically 30 nodes are distributed per wavelength in the inner region. The number of wavelengths and nodes per wavelength can be varied. For multiple frequencies, a discretization can be derived where the node spacing gradually increases as the points

34

are farther from the body. This can resolve short waves near the body and long waves farther away. Convergence and validations are presented later.

The outer region acts as a numerical beach to prevent wave reflection. 20 nodes are distributed over 80 wavelengths with exponentially increasing spacing, as determined by Lee (1992), with the following distribution

$$dy2_i = dy * 1.0378^{\frac{i(i-1)}{2}} \quad \text{for} \quad i = 1..20 \tag{3.8}$$

where dy is the spacing of the outermost nodes in the inner domain. This distribution is sufficient to effectively delay wave reflection for about 15 periods of oscillation. If a longer time simulation is desired, the coefficient and number of outer domain nodes must be adjusted. Lee (1992) discusses this in detail for the two-dimensional problem.

The desingularized sources on the free surface are distributed outside the domain a small distance above the calm water surface. The desingularized distance, l_d, is given by

$$l_d = \sqrt{l_c dy} \tag{3.9}$$

where l_c is some characteristic length scale of the problem, the panel size or smallest node spacing, for example. This problem is discussed by Cao et al. (1991).

The body is modeled using flat panels because they are more suitable for arbitrary body shapes. The two-dimensional method by Zhang (2007) utilizes a "rubber-banding" scheme, where the number of panels remains the same, and the influence matrix size is constant. This has significant benefits, including the ability to use an iterative solver. However, for the body-exact approach, we must allow sections to come out of the water entirely. This would result in body panel resolution that could be orders of magnitude smaller than free surface resolution, leading to ill-conditioned matrices, and resulting in poor numerics.

The alternate approach is to use a "fixed" panelization, in which the body is pan-

elized once, using a preprocessor. This produces better influence matrices and there is never a need to curve fit the the body between time-steps, saving some computation time. This method requires direct matrix inversion, which is the most computationally expensive step in the entire formulation. However, with the problems stated in this formulation, that is beneficial. Since each of the components of the velocity potential (3 total) and acceleration potential (10 total) have the same influence matrix, a single inverted matrix can be used multiple times to solve for each component. The computational time to back-substitute is far less than that to iteratively solve the matrix problem for each component.

3.3   Time-Stepping

The free surface elevation and potential are updated using the kinematic (2.45) and dynamic (2.46) free surface boundary conditions. The rigid body equations of motion, Eqns. (2.55) and (2.56) must also be integrated in time for the case of free motions. Time-stepping is done using a fourth-order Adams-Bashforth scheme

$$P^1 = P^0 + \frac{\Delta t}{24}(55P_t^0 - 59P_t^{-1} + 37P_t^{-2} - 9P_t^{-3}) \tag{3.10}$$

where P is the function being numerically integrated, P_t is the time-derivative, and the superscripts indicate which time-step the values are taken from, i.e. 0 is the current time-step. The quantities that are integrated in such a manner are $P = \phi, \zeta$ for the free surface conditions and $P = v, \eta$ for the body equations of motion.

The time-step size can be chosen as a number of time-steps per period. For example, using $T/100 \leq \Delta t \leq T/200$ is usually sufficient. The spatial resolution, especially on the free surface, can introduce stability problems if the time-step is too coarse. This is discussed by Park and Troesch (1992) and Wang and Troesch (1997),

including a description of a free surface stability index, FSS.

$$FSS = \pi g \Delta t^2 / \Delta x \qquad (3.11)$$

An acceptable value for the stability index is dependent on the discretization and integration schemes used on the free surface. It is aslo dependent on the types of boundary conditions. As a conservative estimate, a value of $FSS \leq 1$ will ensure a stable free surface throughout the computations.

3.4   Body and Free Surface Intersection

In linear theory, the free surface conditions are satisfied on the calm water surface, $z = 0$, and the body boundary conditions are satisfied on the mean position of the body. In the body-exact formulation, the body geometry changes depending on the motions, and we want to integrate the pressure on the actual wetted surface of the hull. This requires a knowledge of the intersection points between the body and the free surface. Using the exact free surface would be very challenging, since only the incident wave is well defined. As a compromise, we can model the intersection of the body up to the incident free surface. The remaining perturbation free surface conditions are linearized about a plane defined by the intersection of the exact body and the incident wave. This differs from the weak-scatterer formulation of Pawlowski (1992), which linearizes the free surface conditions about the incident wave profile.

We want to integrate up to $z = \eta^I$, and the linear incident potential in Eqn. (2.38) is only valid up to $z = 0$. Using this potential and the linearized form of the pressure equation, $p = -\rho(\frac{\partial \phi}{\partial t} + gz)$, from Eqn. (2.33), we find that $p \neq 0$ on $z = \eta^I$ and the dynamic free surface condition is violated. A simple correction, widely used in the offshore industry, is to scale the incident wave potential by modifying the e^{kz} term

with $e^{k(z-\eta^I)}$ when evaluating the pressure, resulting in

$$\phi^I = \frac{iga}{\omega_o}e^{-ik(x_o cos\beta+y_o sin\beta)}e^{iw_o t}e^{k(z-\eta^I)} \tag{3.12}$$

This formulation is similar to that of Wheeler (1970), but assumes deep water. We can verify the dynamic free surface condition using this form of the incident potential. For example, linear waves traveling in the x_o-direction ($\beta = 0$) are given by

$$\phi^I = \frac{iga}{\omega_o}e^{i(w_o t-kx_o)}e^{k(z-\eta^I)} \tag{3.13}$$

$$\eta^I = ae^{i(w_o t-kx_o)} \tag{3.14}$$

We can evaluate the linear incident pressure by examining

$$p^* = \frac{p}{\rho g} = ae^{i(w_o t-kx_o)}e^{k(z-\eta^I)} - z \tag{3.15}$$

and verify that $p^* = 0$ on the incident wave elevation. It is evident that solving for the pressure on $z = \eta^I$ results in zero pressure, thus satisfying the dynamic free surface condition. This modification to the incident potential is sufficient to allow integration up to the incident wave using the body-exact approach.

3.5   Section Exit and Entry

One of the main reasons for using the body-exact approach is the ability to get accurate solutions for large amplitude motions. This includes allowing sections to come out of and go back into the water. This is done simply by stopping calculations as a section comes out of the water, then re-initializing ϕ and ϕ_t to zero at that section. As the section enters the water, the two-dimensional problem is solved as usual. This often leads to spikes in the pressure, as you would expect from an impact problem.

38

3.6 Radial Basis Functions

The $\frac{\partial \phi}{\partial x}$ term in the pressure equation (2.33) can be approximated by using radial basis functions (RBF). Using this method to numerically solve partial differential equations is discussed by Kansa (1999). A more general discussion of RBFs is presented by Buhmann (2000).

Once the two-dimensional problem is solved for each section, the velocity potentials at nodes on the entire body are given as a function of the Euclidean distance between the nodes.

$$f_j(\mathbf{x}_i) \equiv f(|\mathbf{x}_i - \mathbf{x}_j|) \tag{3.16}$$

$$\phi(\mathbf{x}_i) = \sum_{j=1}^{N} \alpha_j f_j(\mathbf{x}_i) + \alpha_{N+1} \tag{3.17}$$

$$\sum_{j=1}^{N} \alpha_j = 0 \tag{3.18}$$

where f is one of many possible basis functions. The final equation (3.18) for the coefficients α_j is to ensure uniqueness. These expansion coefficients are found by setting up a system of $N + 1$ equations, such that

$$P = \begin{bmatrix} 1 \\ \vdots \\ 1 \end{bmatrix} \in \mathbf{R^N}$$

$$F = \begin{bmatrix} f_1(\mathbf{x}_1) & \cdots & f_N(\mathbf{x}_1) \\ \vdots & f_j(\mathbf{x}_i) & \vdots \\ f_1(\mathbf{x}_N) & \cdots & f_N(\mathbf{x}_N) \end{bmatrix} \in \mathbf{R^{N \times N}}$$

$$H = \begin{bmatrix} F & P \\ P^T & 0 \end{bmatrix} \in \mathbf{R^{(N+1) \times (N+1)}}$$

and the $N + 1$ system can be rewritten in matrix form

$$H_{ij}\alpha_j = \phi_i \tag{3.19}$$

with $\phi_{N+1} = 0$. The interpolation expansion coefficients can be found after matrix inversion

$$\alpha_j = [H_{ij}]^{-1}\phi_i \tag{3.20}$$

These coefficients can be used to interpolate the data in three-dimensional space and to find derivatives at any point. The x-velocity of the fluid is found by taking the partial derivative of the basis function with respect to the x-direction.

$$\frac{\partial \phi(\mathbf{x}_i)}{\partial x} = \sum_{j=1}^{N} \alpha_j \frac{\partial f_j(\mathbf{x}_i)}{\partial x} \tag{3.21}$$

Several basis functions were tested and compared before implementation in computations. Of the many functions available, the three shown below exhibit the quality of a "sphere of influence", such that points closer to the node of interest have a larger influence on that node

$$f_j(\mathbf{x}_i) = e^{-\frac{|\mathbf{x}_i - \mathbf{x}_j|}{c_j}} \qquad \text{Exponential Spline} \tag{3.22}$$

$$f_j(\mathbf{x}_i) = e^{-\frac{|\mathbf{x}_i - \mathbf{x}_j|^2}{c_j^2}} \qquad \text{Gaussian} \tag{3.23}$$

$$f_j(\mathbf{x}_i) = (1 + \frac{|\mathbf{x}_i - \mathbf{x}_j|^2}{c_j^2})^{-1/2} \qquad \text{Inverse MQ} \tag{3.24}$$

Using a defined analytic velocity potential as a test, the candidate functions were compared for accuracy of interpolation and approximation to partial derivatives. The analytic potential was of the form $\phi \propto x^2$, with some variation for nodes on the same station (x-location). Another function, $\phi \propto x^2 + x^3$, was tested as well. The approximate partial x-derivatives were compared to the known solutions. The Gaussian

40
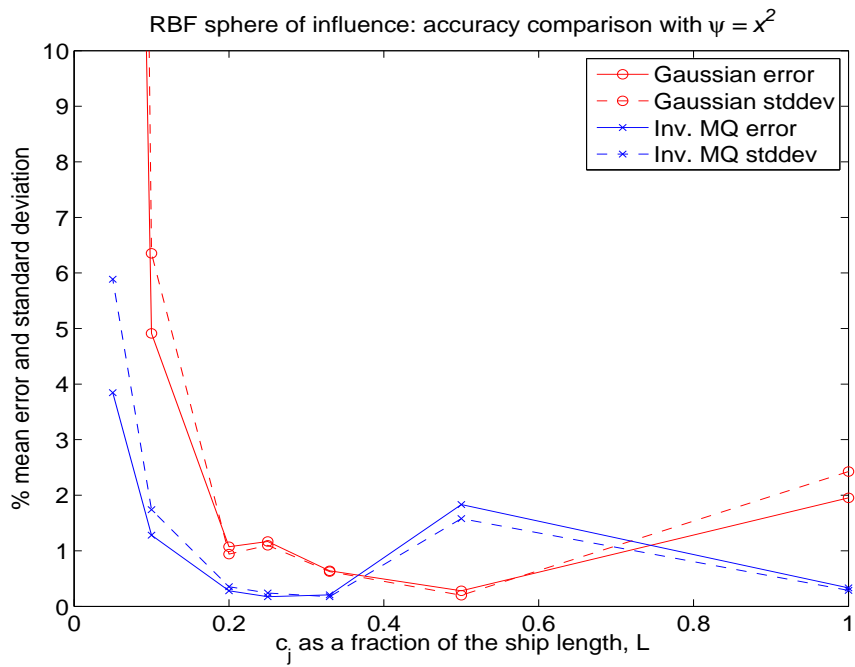
Figure 3.1: RBF c_j comparison, $\phi \propto x^2$
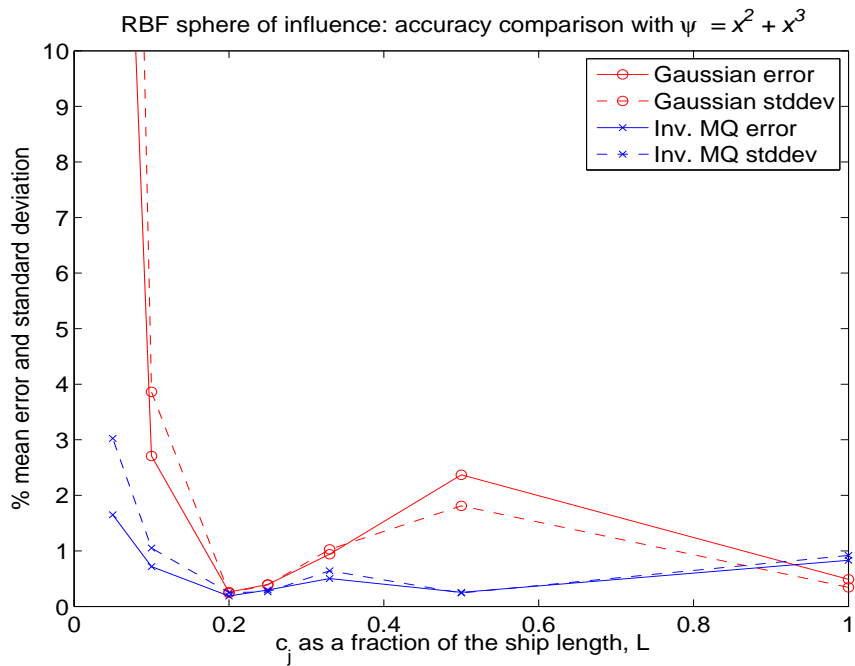
Figure 3.2: RBF c_j comparison, $\phi \propto x^2 + x^3$

(3.23) and Inverse Multi-Quadratic (3.24) functions proved to be the more accurate basis functions. Their accuracy depends on the "sphere of influence" term, c_j. Several tests cases were run to determine an the optimum value of this variable. The test cases involved computing the partial x-derivative of the RBF approximation and comparing it to the known solution. Both the Gaussian and Inverse Multi-Quadratic functions were evaluated. Mean error and standard deviation were considered as benchmarks of comparison. The percentages (based on the mean absolute value of the exact solutions) of mean error and standard deviation are shown as functions of c_j in Figures 3.1 and 3.2. They indicate that using approximately $L/4$ yields good results for both functions. The estimation at the end sections is not as good because the interpolation is only one-sided.

Implementing this basis function in the computations resulted in occasional instabilities, especially for extreme amplitude motions at higher frequency. The source of the instability is the $\frac{\partial \phi}{\partial x}$ term estimated by the RBF. It is a result of very high condition numbers in the matrix inversion routines, which use Gaussian elimination. Several attempts were made to correct this, but some instabilities remained. The Exponential Spline function, Eqn. (3.22), although less accurate, had much better condition numbers. The final selection for use in the code was an exponential function of power 1.5, as shown in Eqn. (3.25). This function was much more accurate than the Exponential Spline while being better conditioned for matrix inversion than the Gaussian function.

$$f_j(\mathbf{x}_i) = e^{-\frac{|\mathbf{x}_i - \mathbf{x}_j|^{1.5}}{c_j^{1.5}}} \tag{3.25}$$

The results were again verified against analytic velocity potentials. This RBF gives accurate approximations to $\frac{\partial \phi}{\partial x}$, while remaining stable when implemented in the real code for actual ship hulls.

42

3.7   Computation Time

An important aspect of this work is computational efficiency. The code can achieve real-time simulations on a high-end desktop computer with multiple cores, which are common today. The implementation of a strip theory allows very efficient use of multi-core machines. The most computationally expensive portion is matrix inversion, followed by back-substitution of the many right-hand sides, that must be done at each time-step. Most of these matrix operations can be done independently for each station. The matrix inversion and back-substitution routines used are available in LINPACK, written in Fortran. They are efficient, accurate, and well-suited for this type of problem.

For example, consider a ship with 20 stations, where each station has 100 free surface nodes on either side of the body (including the beach) and 50 panels to model the body. This requires inverting 20 influence matrices with size 250x250 at each time-step. In this example, it takes approximately 0.02sec/station/time-step of wall-clock time using an Intel®Core™2 2.4GHz processor and Intel®Fortran compiler, *without* parallelization. Solving the forward speed problem with radial basis functions introduces more matrix inversions, and an additional 0.4sec/time-step. All computations take 0.8sec/time-step in this example. If the period of oscillation is about $T = 15$sec and the time-step size is about $T/100$ (typical values for real ship simulations), the simulation will execute five times slower than real-time. However, if the compiler supports multi-core directives, significant improvements can be made. The two-dimensional problems are independent of one another, and can be solved in parallel.

The OpenMP architecture supported in the Intel®Fortran compiler is ideal for these sort of computations. The execution speed scales very well with the number of processors or cores, up to the number of stations. The current code has been tested for parallelization performance on two-, four-, and eight- core machines, common for

present-day desktops. There is some overhead that will not scale with the number of cores, unless the code is optimized in more detail. Regardless, exploiting the independence of the two-dimensional problems offers significant speed gains. For example, running the same test case *with* parallelization on an eight-core machine shows $85 - 90\%$ average CPU utilization, resulting in simulations faster than real-time.

CHAPTER IV

Two-Dimensional Results

The origin of this section is based on the two-dimensional boundary element method developed by Zhang (2007). One fundamental departure from that work is the direct solution the acceleration potential, instead of numerical differentiation of the velocity potential, which is a significant improvement. It offers better solutions of $\frac{\partial \phi}{\partial t}$ and can be coupled with the equations of motions, as described earlier. Many other aspects, such as panelization models, spatial and temporal discretization, and numerical techniques, have been developed to better suit the body-exact approach. These factors complicate a direct comparison of the current and original methods. The following sections go through a range of test cases to verify the two-dimensional computations. In many cases, select results are shown using the approach originally given by Zhang (2007).

4.1 Validation of the Acceleration Potential

The form of the acceleration potential derived in this approach can be compared with other methods. Two methods are chosen in this case. The first is the original numerical differentiation of $\frac{\partial \phi}{\partial t}$ using central or backwards differencing schemes, as originally done in Zhang (2007). The second is the method discussed by Kang and Gong (1990), in which a boundary value problem is set up to solve for $\frac{\delta \phi}{\delta t}$, as defined
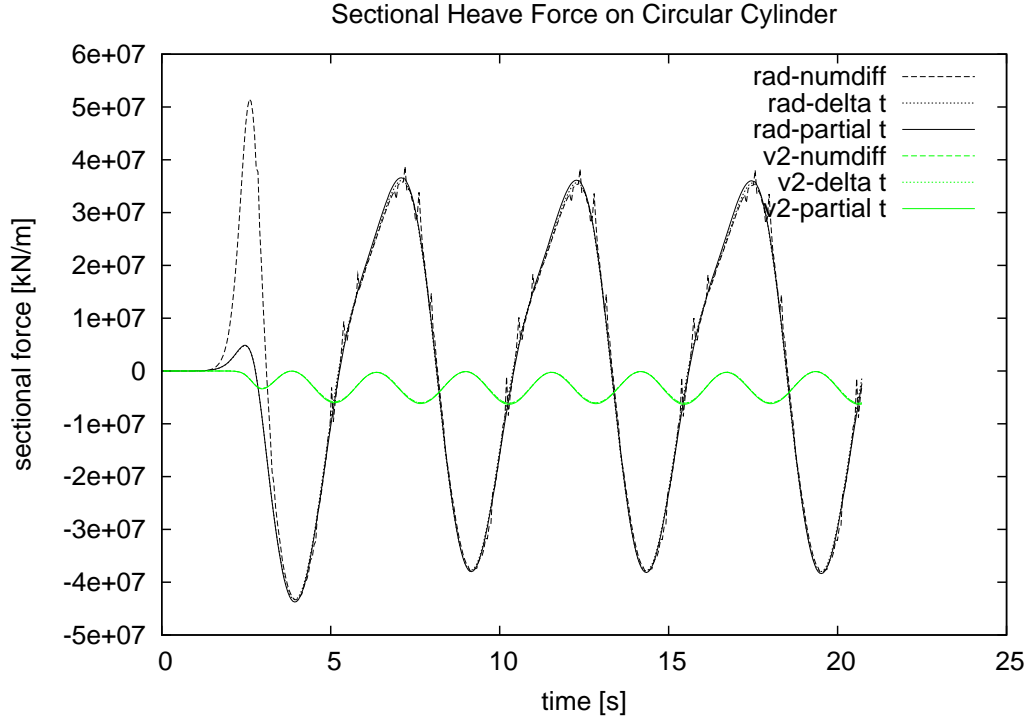
Figure 4.1: Circular Cylinder Forced Heave, $a = 2m$, $R = 10m$, $\omega^2 R/g = 1.5$

in Eqn. (2.57).

The sectional heave force on a two-dimensional circular cylinder is calculated at a range of amplitudes. The non-dimensional frequency is $\omega^2 R/g = 1.5$ where $R = 10m$. The amplitudes of motion are at $a = 2, 4, 6m$. Figures 4.1 through 4.3 show the radiation, "rad", and second order, "v2", components of the force on the section in each of these cases. These components correspond to the first and second order terms found in the pressure equation (2.33). The three methods are labeled "numdiff", "delta", and "partial" for the numerical differentiation, $\frac{\delta\phi}{\delta t}$, and $\frac{\partial\phi}{\partial t}$ formulations, respectively. The hydrostatic force is not shown, since it would be identical between the methods.

In Figure 4.1, all three sets of results agree well. There are some spikes in the radiation force from numerical differentiation. They are due the fact that the differencing scheme has difficulties if the number of panels changes between time-steps. As the amplitude increases, significant nonlinearities start to arise in the radiation
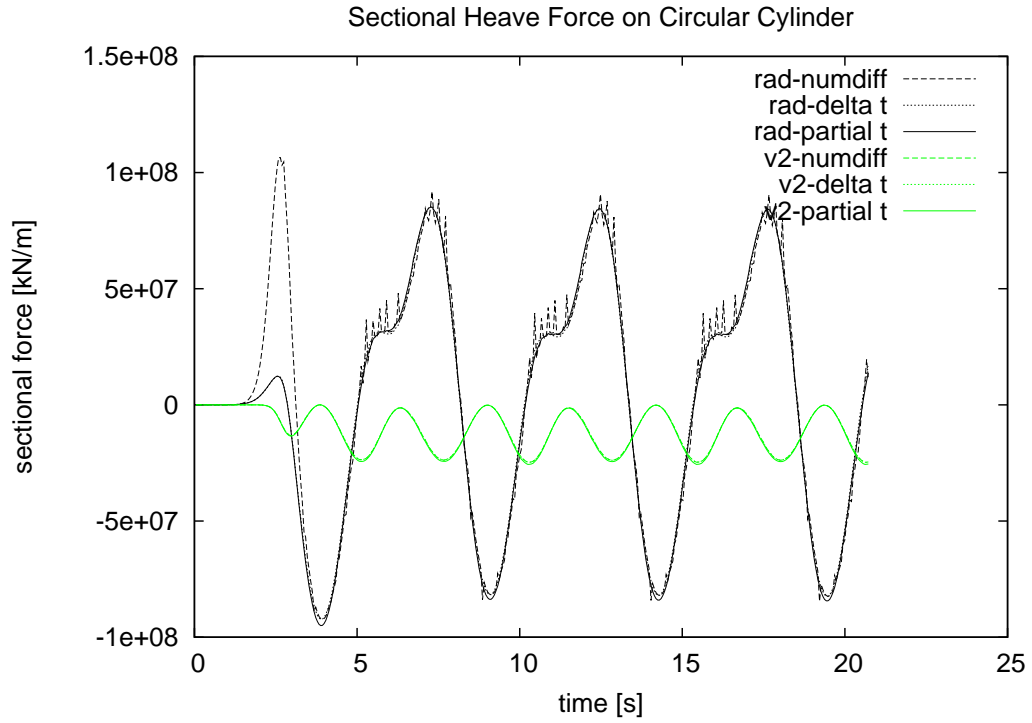
Figure 4.2: Circular Cylinder Forced Heave, $a = 4m$, $R = 10m$, $\omega^2 R/g = 1.5$
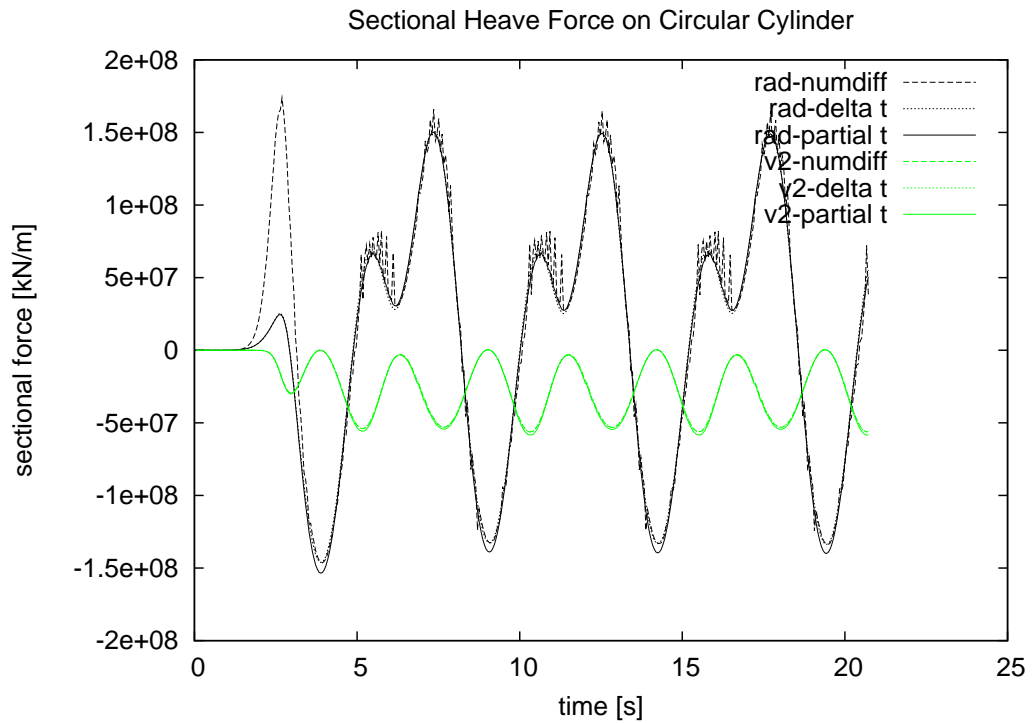
Figure 4.3: Circular Cylinder Forced Heave, $a = 6m$, $R = 10m$, $\omega^2 R/g = 1.5$

47

component, and these spikes get more severe. In the body-exact formulation, some of the advantages of a direct solution for $\frac{\partial \phi}{\partial t}$ can be seen in these results, especially in Figures 4.2 and 4.2

The method proposed by Kang and Gong (1990) offers the same advantages and compares very well with the current method. However, the problem becomes difficult when considering how the free surface conditions must be specified. The entire boundary value problem is written in terms of body-frame time-derivatives, including the free surface. For example, in six degree-of-freedom motions, the body rotation rates become part of the free surface conditions. Numerical accuracy becomes a concern, as there would be sums and differences of large numbers, coming from $\boldsymbol{\omega} \times \boldsymbol{r}$ contribution to the free surface conditions. Therefore, the approach derived earlier, to set up a boundary value problem for ψ (or $\frac{\partial \phi}{\partial t}$) is a better alternative.

4.2 Convergence Studies

The convergence characteristics of the numerical methods used must be examined. This gives an idea about what sort of parameter ranges are acceptable for computational simulations. The studies here are for a two-dimensional circular section of radius $R = 10m$, with a forced heave motion amplitude of $1m$. The mean position coincides with half of the cylinder being submerged. Two oscillation frequencies are used, $\omega(R/g)^{0.5} = 0.6, 1.6$, in order to observe convergence a case of long and short wavelengths generated on the free surface. Using $R = 10m$ is convenient in that the non-dimensional frequency is approximately equal to the dimensional value. After the time simulation, the resulting heave force time series are Fourier transformed. Corresponding to linear seakeeping theory, the first-order component of the hydrodynamic force is divided into added mass and damping coefficients; the components that are in phase with the acceleration and velocity of the body, respectively.

Four parameters are studied: time-step size, body panel resolution, inner free

surface resolution, and free surface domain size. The time-step size is based on the a fraction of the period of oscillation. Body panel resolution is based on the number of panels used to model the circular section. Inner free surface resolution is the number of nodes on the free surface near the body with spacing comparable to the body panel spacing. Free surface domain size is the length the free surface extends to, *excluding* the numerical beach.

Each parameter is analyzed by changing its value while leaving the others fixed. The benchmark is a high resolution set of parameters where a converged solution exists. This can be determined by trial and error, using multiple iterations. The convergence of each parameter can be checked by decreasing that parameter's resolution. The convergence of the coefficients is presented in Figures 4.4 and 4.5. The coefficients are non-dimensionalized using ρ, g, R, and A, the fluid density, gravitational acceleration, cylinder radius, and submerged area, respectively.

The four parameters are plotted together against the fraction of the high resolution, or benchmark, values. The benchmark values used are a time-step of $T/400$, 250 total body panels (half are submerged in the body's mean position), 40 inner free surface nodes, and free surface length of $1000m$ or $100R$. The body panel number shows the same type of convergence in the Figures, and is important to get accurate solutions. The time-step and inner free surface resolution converge much faster, and appear to be almost constant. The time-step converges so quickly because of the acceleration potential formulation and higher order schemes used to evolve the free surface conditions. The free surface extent converges more slowly in the low frequency case, shown in Figure 4.4, because the radiated wavelength is significantly longer. The long and short wavelengths are approximately $172m$ and $24m$. This suggests that the numerical techniques described can be used to model a range of wavelengths accurately.
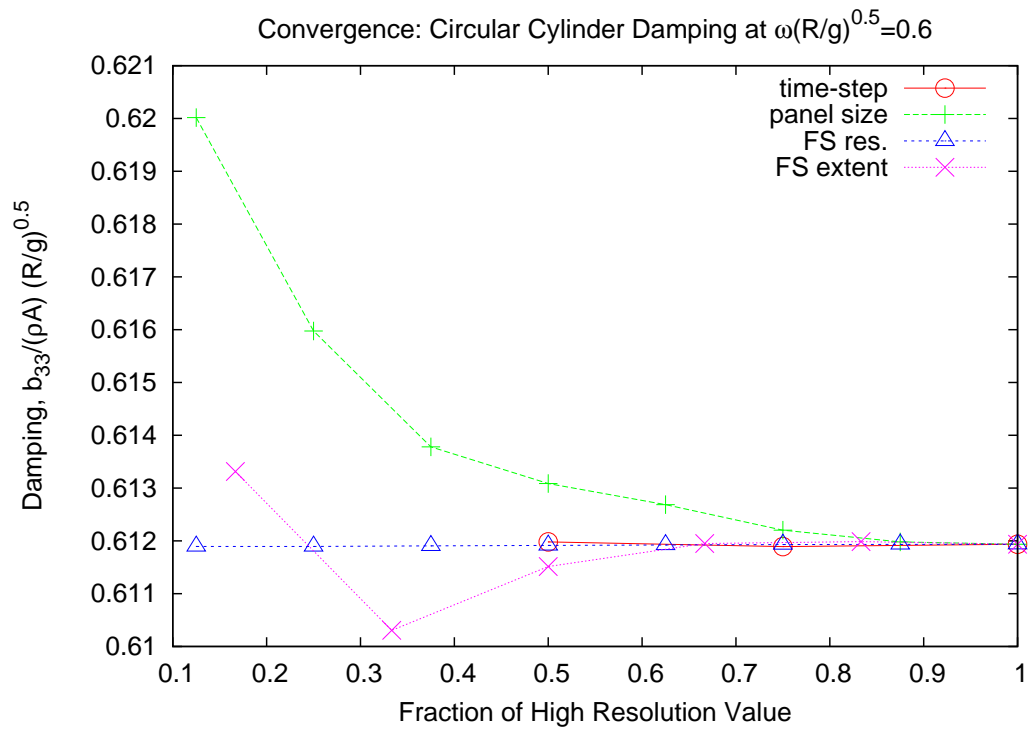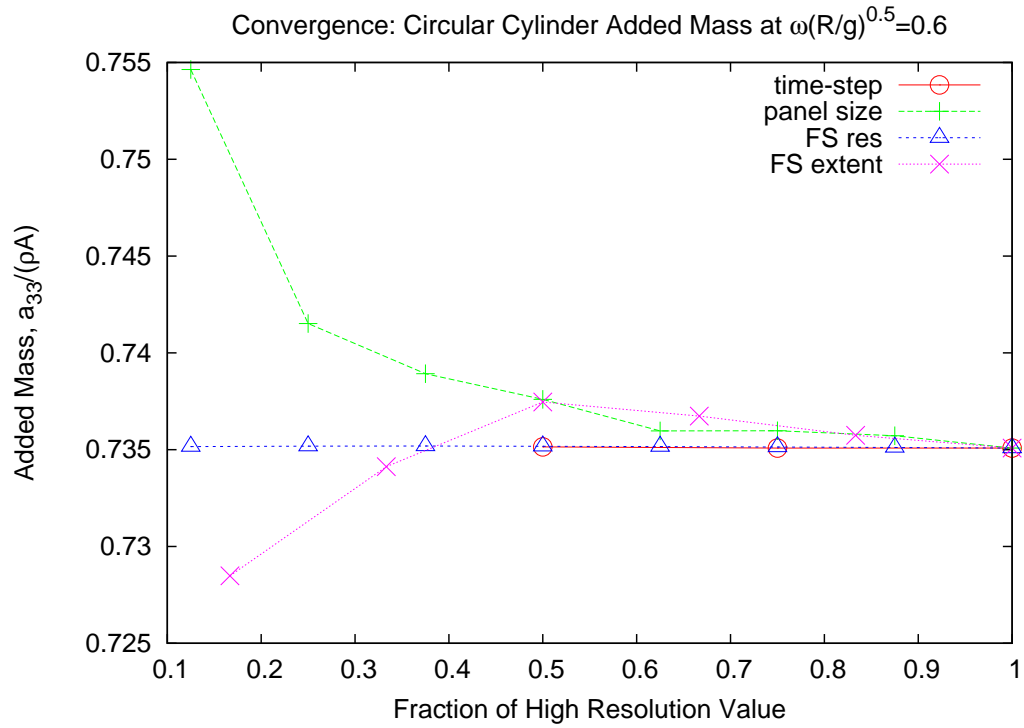
Figure 4.4: Convergence of Circular Cylinder in Heave, $\omega = 0.6$
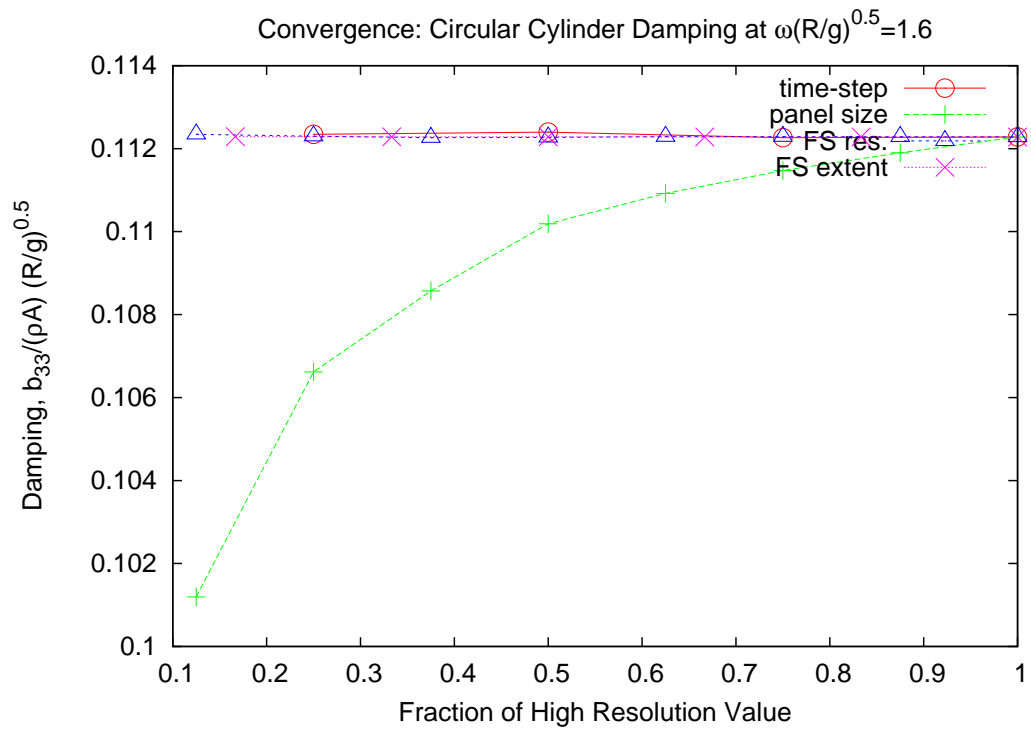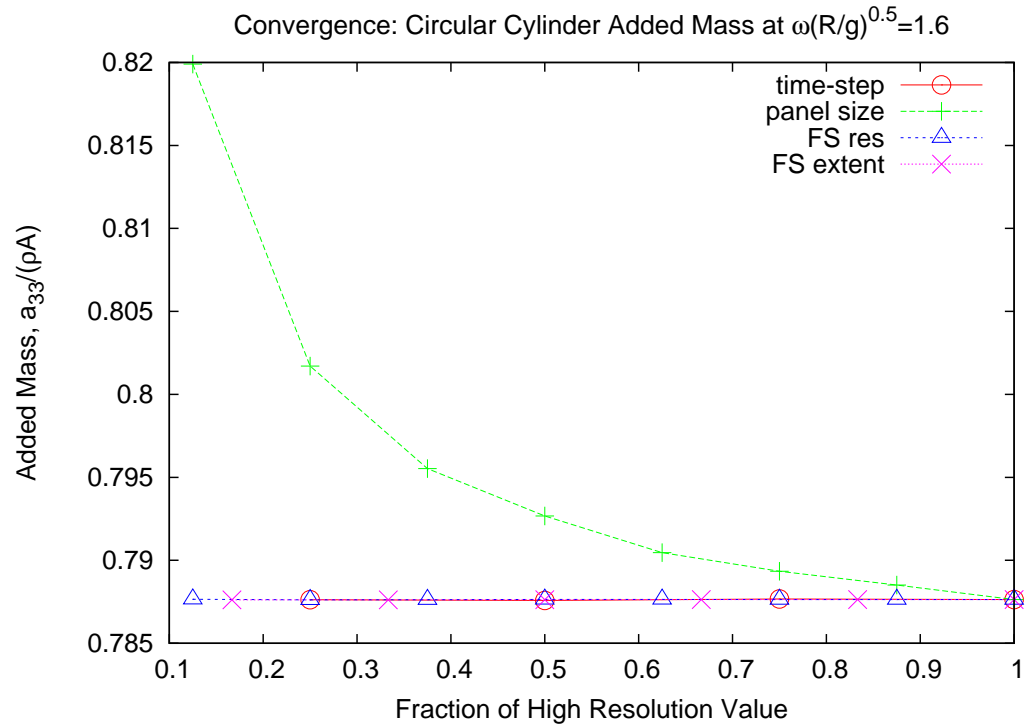
Figure 4.5: Convergence of Circular Cylinder in Heave, $\omega = 1.6$

4.3 Small Amplitude Radiation

The numerical results must be validated against experiments. Vugts (1968) offers a range of experimental data on various two-dimensional cross-sections. The sections compared are the circular cylinder and box barge types. The circular section has a radius $R = 10m$, and the box barge used has beam $B = 20m$ and draft $T = 10m$. In either case, the non-dimensional frequency is given as $\omega(B/2g)^{0.5}$, consistent with the conventions used by Vugts (1968).

The circular cylinder hydrodynamic coefficients are compared using the current method, an alternate free surface spacing, and the experimental results, as shown in Figures 4.6 and 4.7. The "current method" uses the incrementally increasing node spacing technique for the inner free surface and is independent of the frequency of oscillation. The initial node spacing is comparable to the body panel size while the outermost is comparable to the radius, and 80 nodes are distributed with increasing spacing. This is the same scheme used in the convergence studies. The "Alt. FS Grid" solutions use a constant node spacing, $\lambda/40$ in this case, to model the free surface over two wavelengths. Both methods use the same numerical beach. The two methods use the same number of points to model the boundaries and require the same amount of computational effort.

The results shown agree very well with the experimental data. Moreover, they justify the use of the free surface node distribution. The current method shows better agreement than the computationally comparable alternate free surface grid, when using the same number of nodes. This is especially evident at lower frequencies. The alternate method could use a higher resolution to resolve longer waves, but this would require more computation time.

The same set of computations can be carried out for the box barge section. The roll problem is also examined, including the coupling between roll and sway motions. The same sets of results are shown, in addition to "Viscous" simulations, which add
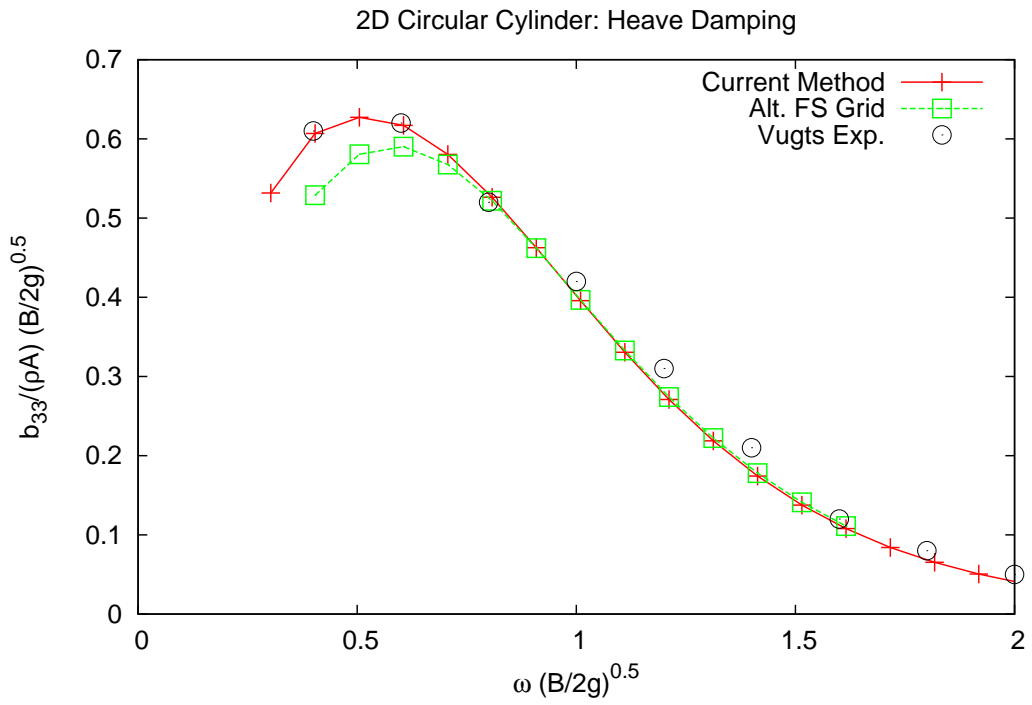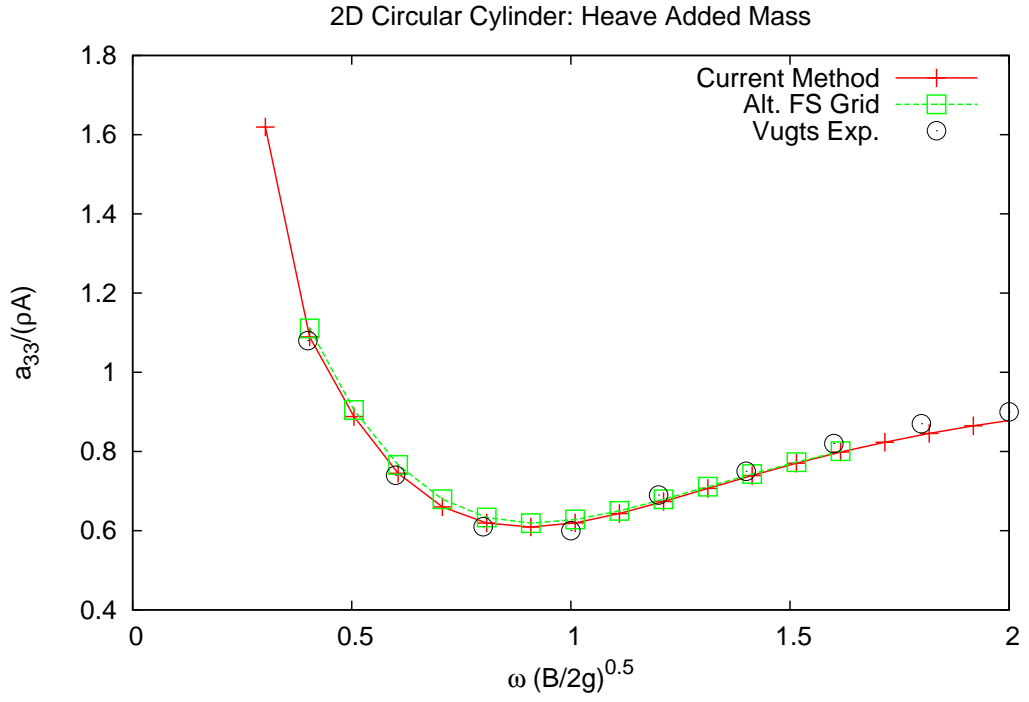
Figure 4.6: Circular Cylinder Heave Added Mass and Damping
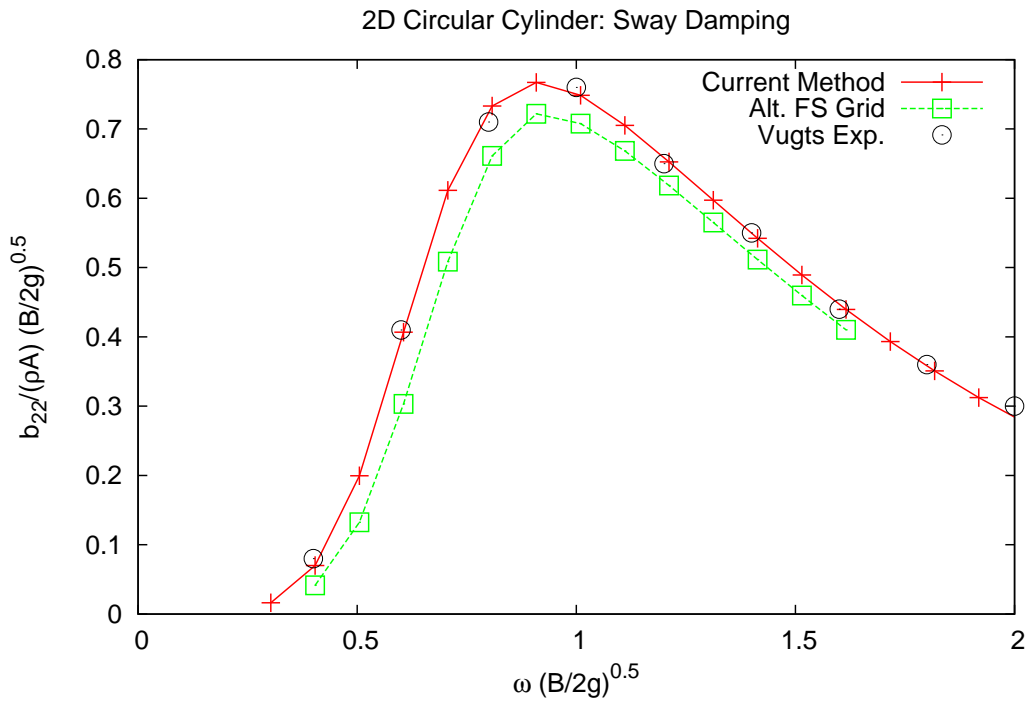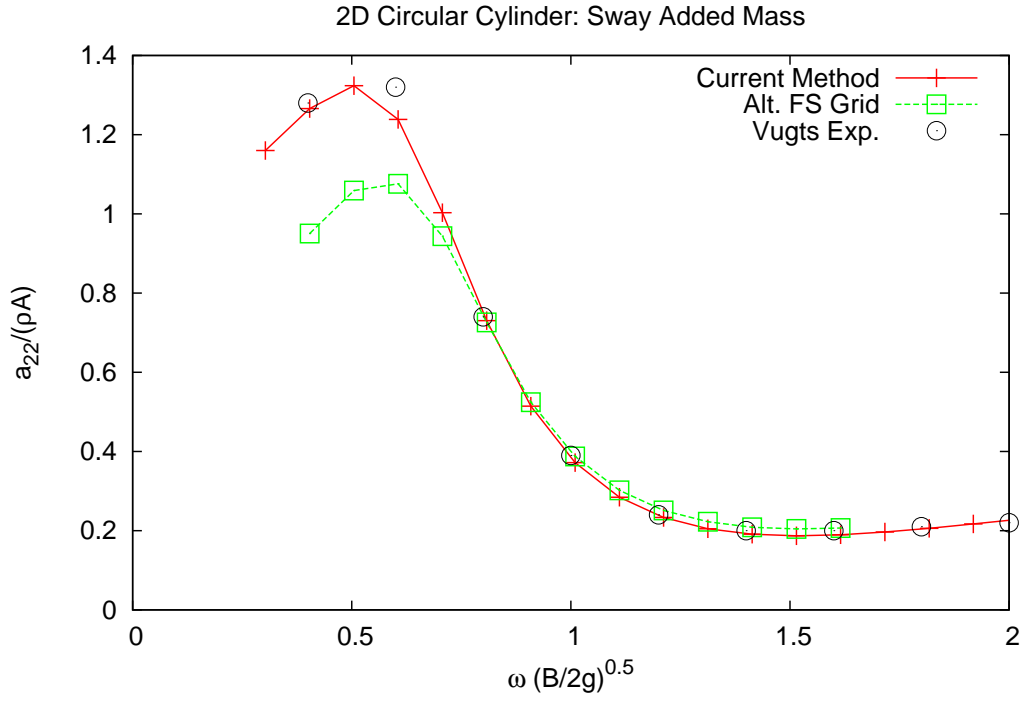
Figure 4.7: Circular Cylinder Sway Added Mass and Damping

the viscous roll correction described earlier and only affect the roll moment due to roll. The heave, sway, roll, roll due to sway, and sway due to roll result comparisons are shown in Figures 4.8 through 4.12.

The characteristics between the current method and alternate free surface grid technique are similar to those for the circular cylinder. The addition of the viscous roll correction term only affects the roll due to roll damping coefficient in Figure 4.10, as expected, improving the agreement with experiments. The roll due to roll added mass differs from the experimental value, showing similar trends to linear theory results. The coupling coefficients show good agreement, with the exception of the roll due to sway damping shown in Figure 4.11. The computational results maintain the symmetry of the coupling coefficients, $a_{24} = a_{42}, b_{24} = b_{42}$. The experiments differ, mainly due to the effects of viscosity, especially in the damping coefficients.

Overall, the agreement with experimental results for the two-dimensional problems studied is very satisfactory. The method of gridding the free surface, as described earlier, has also been justified. The same numerical discretization of the boundaries is used in all the simulations. It accurately predicts the forces for a variety of oscillation frequencies in all modes of motion, emphasizing the robust capabilities of the numerical methods.

4.4   Large Amplitude Oscillations of a Circular Cylinder

The body-exact method can be validated by using test cases in which the wetted geometry of a section changes significantly. This is especially important in sections whose sides are not vertical, or "wall-sided". The forced heave oscillation of a circular cylinder is a classic example of this. Yamashita (1977) presented a range of experimental and theoretical results for this type of problem. Kent (2005) developed a numerical method using a third-order pseudo-spectral method. Zhang (2007) also presents numerical results for this problem, using the body-exact time-domain

2D Box Barge (B/T=2): Heave Added Mass

2D Box Barge (B/T=2): Heave Damping
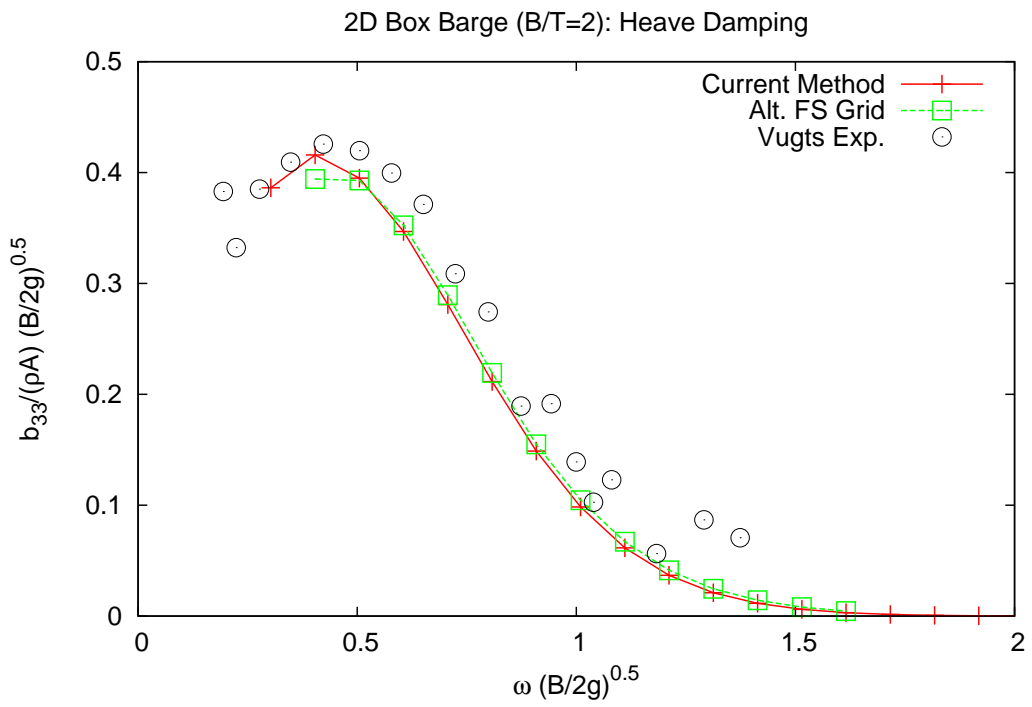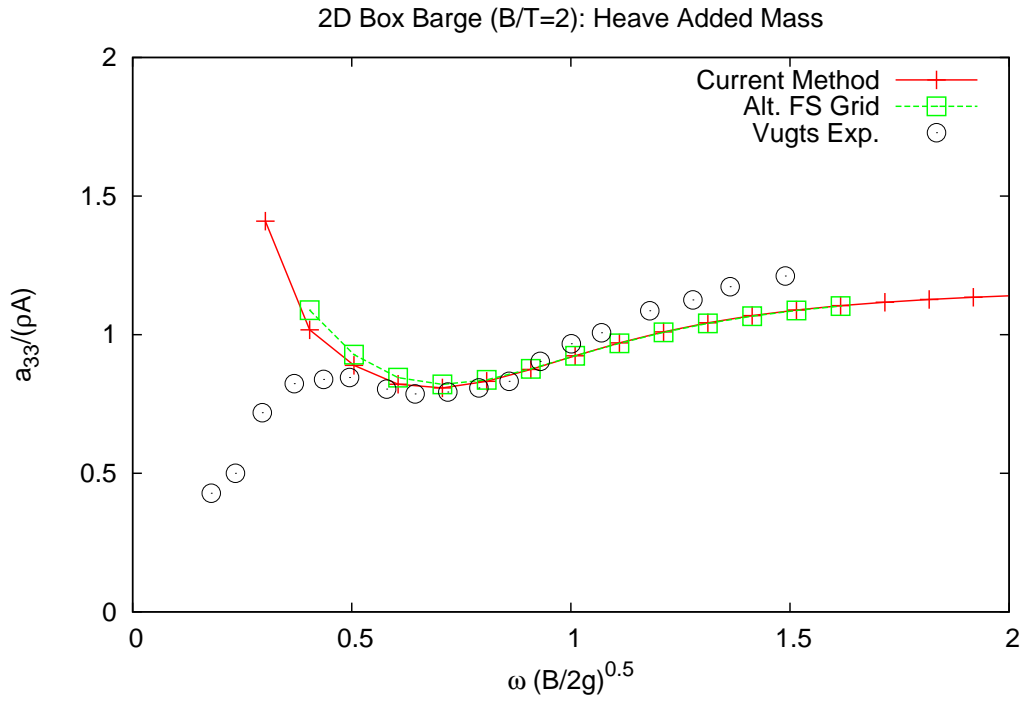
Figure 4.8: Box Barge Heave Added Mass and Damping
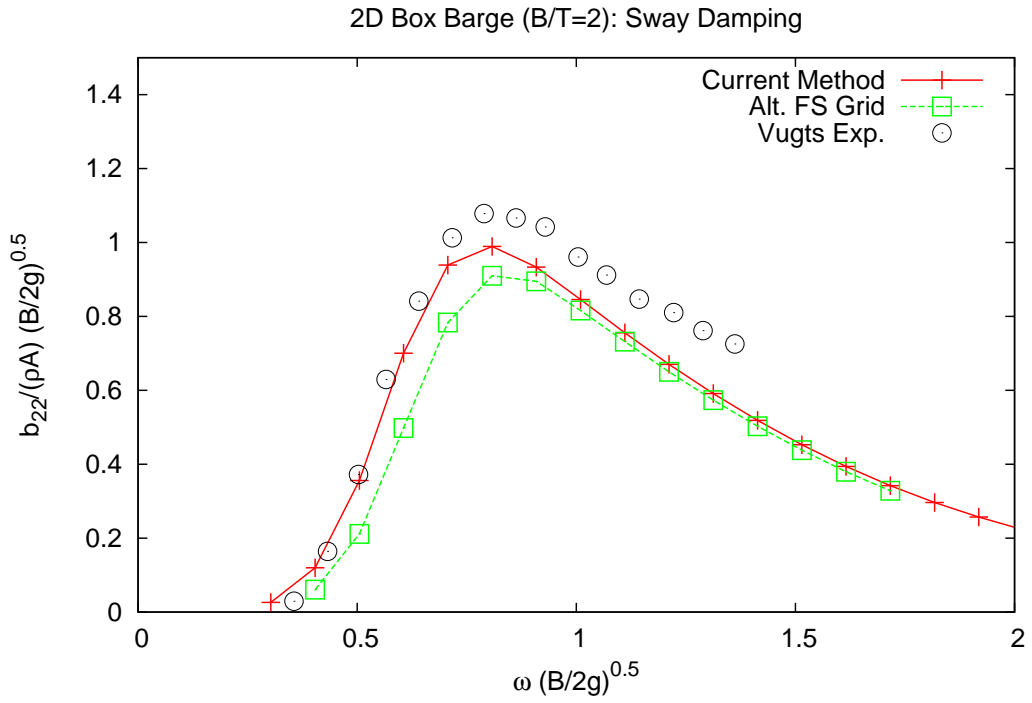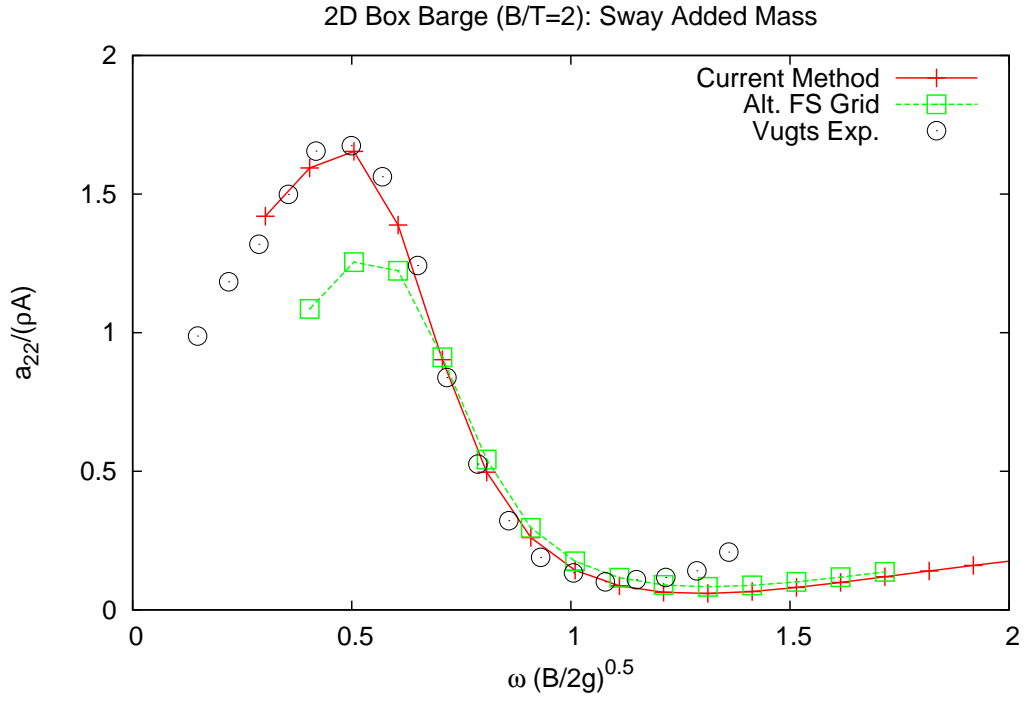
Figure 4.9: Box Barge Sway Added Mass and Damping
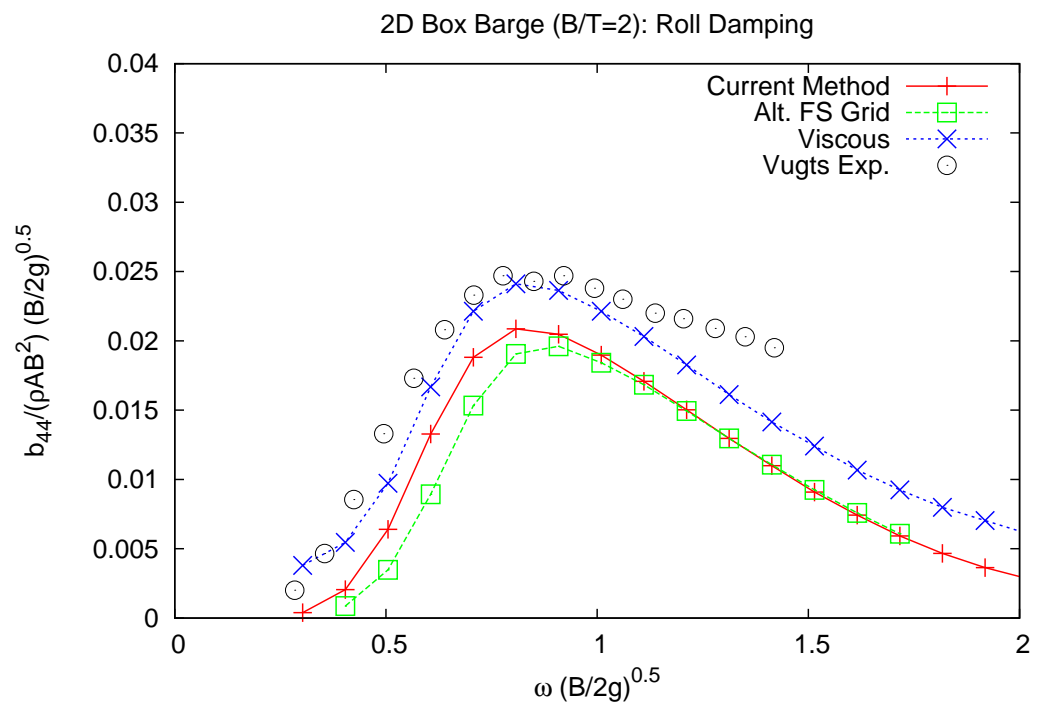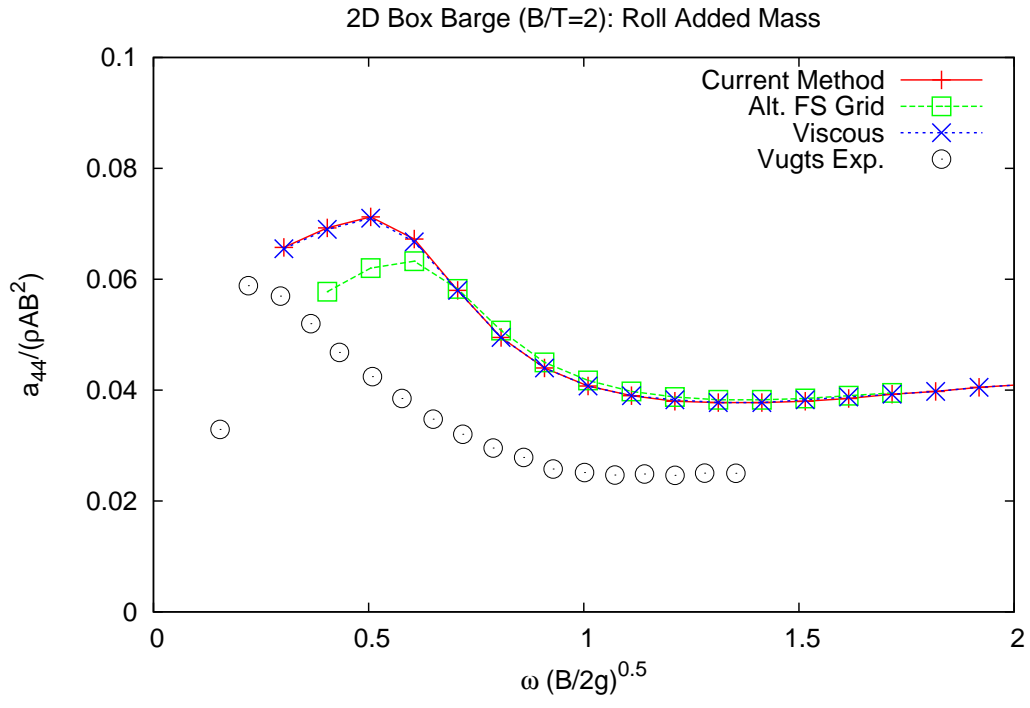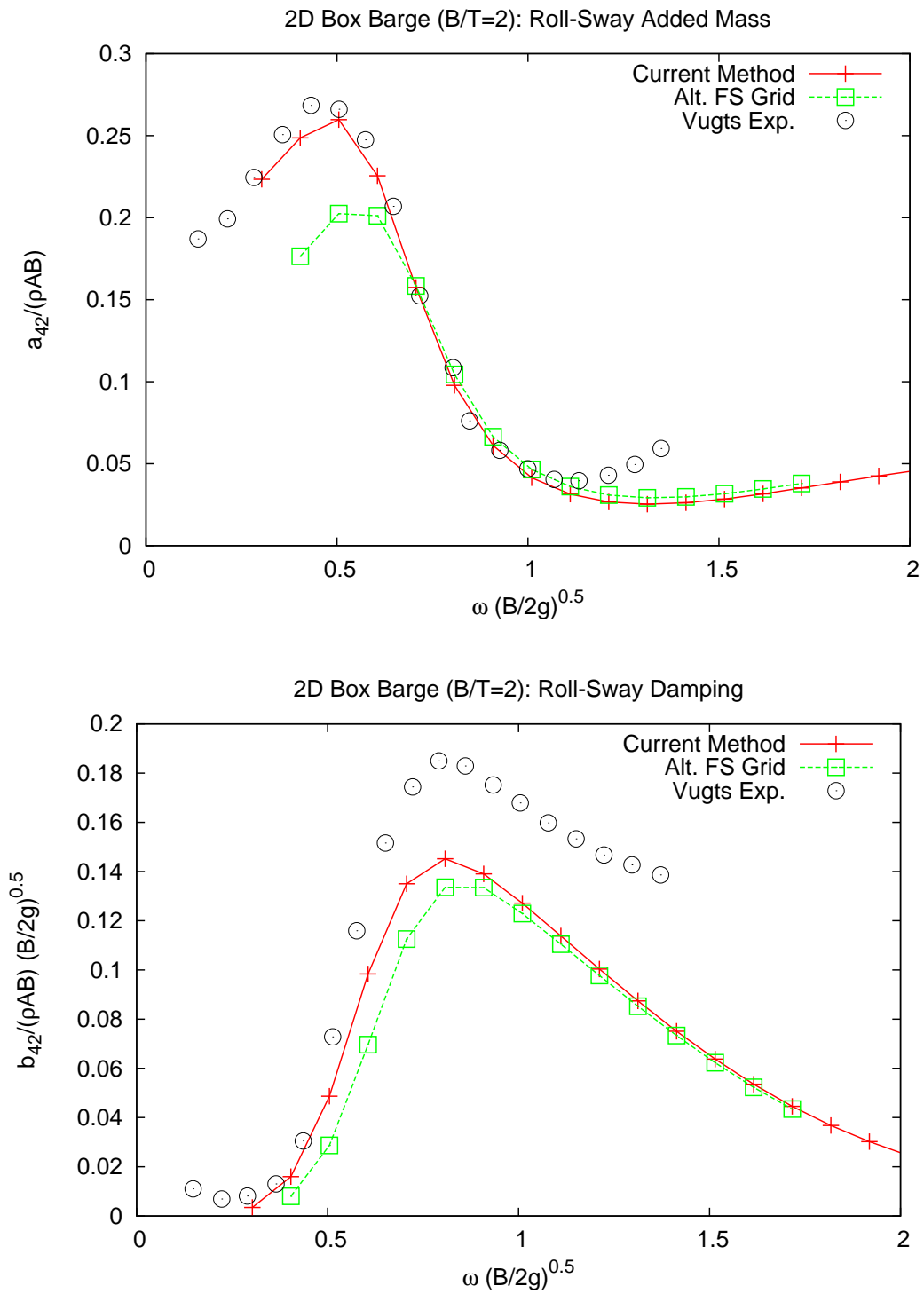
Figure 4.10: Box Barge Roll Added Mass and Damping

Figure 4.11: Box Barge Roll-Sway Added Mass and Damping

Figure 4.12: Box Barge Sway-Roll Added Mass and Damping
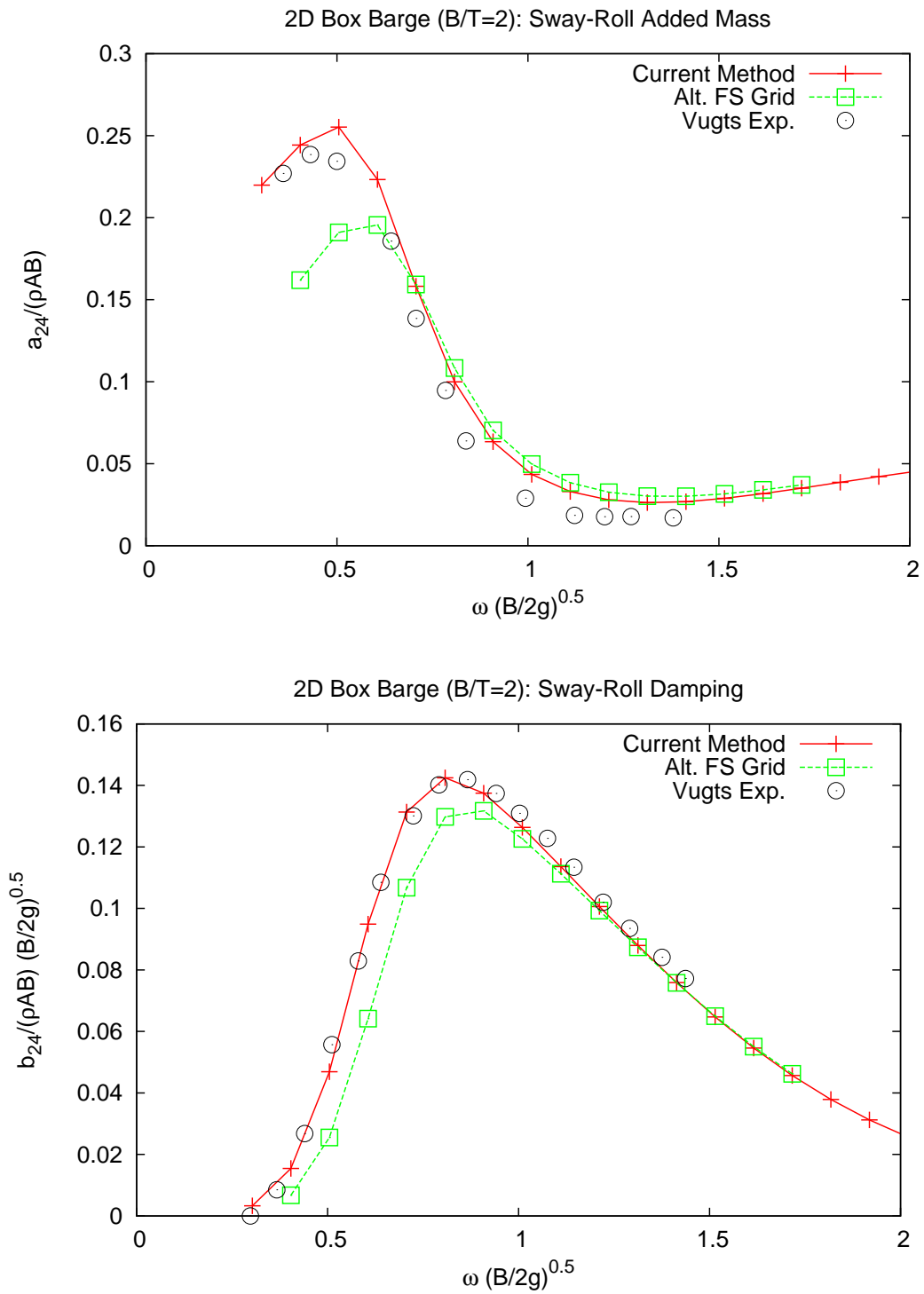
a/R=0.2	$\omega^2 R/g$	a_{33}	b_{33}	F_0^2	F_A^1	F_A^2
Yamashita (1977)	0.5	0.66	0.504	-0.01	/	0.15
Kent (2005)	0.5	0.600	0.557	-0.010	0.821	0.194
Zhang (2007)	0.5	0.630	0.574	-0.013	0.815	0.163
Current Method	0.5	0.649	0.573	-0.014	0.808	0.202
Yamashita (1977)	1.0	0.60	0.386	-0.08	/	0.45
Kent (2005)	1.0	0.580	0.371	-0.086	0.615	0.491
Zhang (2007)	1.0	0.600	0.406	-0.086	0.632	0.428
Current Method	1.0	0.611	0.398	-0.095	0.607	0.409
Yamashita (1977)	1.5	0.69	0.267	-0.15	/	0.8
Kent (2005)	1.5	0.620	0.254	-0.160	0.360	0.796
Zhang (2007)	1.5	0.670	0.279	-0.190	0.378	0.620
Current Method	1.5	0.671	0.262	-0.193	0.327	0.590

Table 4.1: Heave Force Coefficients on Circular Cylinder, amplitude = 0.2R

approach. Their results, along with the current method, are presented as force coefficients in Table 4.1.

The results are given for three non-dimensional frequencies, $\omega^2 R/g$, where ω is the circular frequency of oscillation, R is the radius, and g is the gravitational constant. Coefficients are given for: the non-dimensional sectional added mass and damping, a_{33} and b_{33}; the second-order mean force, F_0^2; the first-order harmonic force, F_A^1; and the second order harmonic force, F_A^2. The coefficients are defined in Eqns. 4.1 through 4.5, consistent with Yamashita (1977).

$$a_{33} = \frac{Re[f(\omega)]}{\omega^2 a} \tag{4.1}$$

$$b_{33} = \frac{Im[f(\omega)]}{\omega a} \tag{4.2}$$

$$F_0^2 = \frac{|f(0)| - \rho g A}{2\rho g a^2} \tag{4.3}$$

$$F_A^1 = \frac{|f(\omega)|}{2\rho g R a} \tag{4.4}$$

$$F_A^2 = \frac{|f(2\omega)|}{2\rho g a^2} \tag{4.5}$$

where f is the sectional force time-series, Re and Im represent its real and imagi-

nary Fourier components, $|f(\omega)|$ indicates the amplitude of the Fourier component at frequency ω, ρ is the water density, a is the amplitude of motion, A is the submerged sectional area. It is worth noting that the added mass and damping are defined in the classical sense, meaning *only* the first-order radiation force, while the force coefficients include the *entire* sectional force. The difference between the two, in this case, is the body-exacty hydrostatic force. We do not expect the magnitude of a_{33} and b_{33} to equal F_A^1, especially for increasing amplitudes of motion.

CHAPTER V

Strip Theory Results

The two-dimensional body-exact techniques described earlier can be extended to three-dimensions using the strip theory approximation. In the following sections, a variety of hull forms will be used for validations and discussion of results using the body-exact strip theory approach. The main particulars of these vessels are listed in Table 5.1, where L, B, T are the length, beam, and draft (all in meters). C_B and C_{WP} are the block and waterplane coefficients of the hull, defined by

$$C_B = \frac{Vol}{LBT} \tag{5.1}$$

$$C_{WP} = \frac{A_{WP}}{BT} \tag{5.2}$$

where Vol and A_{WP} are the submerged volume and waterplane area, respectively, when the hull is in its mean position.

	L	B	T	C_B	C_{WP}
	[m]	[m]	[m]	(nd)	(nd)
Wigley I	3.00	0.300	0.1875	0.557	0.689
Wigley III	3.00	0.300	0.1875	0.459	0.689
Series 60 (0.7)	121.9	17.42	6.97	0.700	0.793
m5514 (Destroyer)	142.0	19.10	6.50	0.518	0.790
m5613 (Tumblehome)	154.0	18.80	5.50	0.536	0.790
S-175 Containership	175.0	25.40	9.50	0.570	0.723

Table 5.1: Hull Particulars

The validations included are separated into radiation and wave excitation problems. The radiation problem includes isolated forced motions in one degree of freedom with no incident wave field, while the wave excitation problem fixes the ship and exposes it to an incident wave field. This allows the isolation of the boundary conditions, validating each separately. In both cases, the forces and moments acting on the hull are calculated into a time-history. The amplitudes are kept small so that time-histories may be Fourier transformed into linear components, either classical added mass and damping terms (in phase with the acceleration and velocity, respectively) or an amplitude and phase (typically done for exciting forces).

5.1 Small Amplitude Radiation

The body-exact strip theory approach must first be validated for small amplitude motions. The hydrodynamic coefficients from forced motions can be compared to linear theory or experimental results. The "Wigley" hull forms have extensive numerical and experimental results available, and will be used as test hulls. The Wigley I and III models will be used in forced heave and pitch simulations with forward speed of $Fn = 0.3$, where

$$Fn = \frac{U_o}{\sqrt{gL}} \tag{5.3}$$

The hydrodynamic coefficients, added mass and damping, are calculated for heave and pitch motions of the Wigley I hull and compared to other computational and experimental results. The current method results are given, as well as a five degree-of-freedom strip theory developed at MIT (as referenced by Nakos and Sclavounos (1990)) based on the work of Salvesen et al. (1970), the three-dimensional code SWAN described by Nakos (1990), and experimental results from Gerritsma (1988) and Journée (1992).

The linear strip theory results, based on the Salvesen et al. (1970) formulation,

might be expected to agree exactly with the current method, given that the amplitude of motion is small. However, we briefly examine a key difference in the treatment of the forward speed correction to the strip theory. In the linear strip theory, a variant of Stokes' theorem is used to replace the $\frac{\partial \phi}{\partial x}$ term in the pressure equation (2.33). This was originally derived by Ogilvie and Tuck (1969), and resulting expressions for the coefficients in heave and pitch are given by

$$A_{33} = A_{33}^0 \tag{5.4}$$

$$B_{33} = B_{33}^0 \tag{5.5}$$

$$A_{35} = A_{35}^0 - B_{33}^0 U_o/\omega^2 \tag{5.6}$$

$$B_{35} = B_{35}^0 + A_{33}^0 U_o \tag{5.7}$$

$$A_{53} = A_{53}^0 + B_{33}^0 U_o/\omega^2 \tag{5.8}$$

$$B_{53} = B_{53}^0 - A_{33}^0 U_o \tag{5.9}$$

$$A_{55} = A_{55}^0 + A_{33}^0 U_o^2/\omega^2 \tag{5.10}$$

$$B_{55} = B_{55}^0 - A_{33}^0 U_o^2/\omega^2 \tag{5.11}$$

where the left hand sides are the forward speed coefficients, and the superscript ^{0} on the right-hand sides indicate the zero speed coefficients. The formulation is based on the assumption that the steady velocity potential is given by $U_o x$, ignoring the steady perturbation potential introduced by the presence of the ship. Also, everything is based on the mean position of the hull, consistent with linear strip theory. The first assumption has since been shown to lead to errors, in certain cases.

The diagonal coefficients in Figures 5.1 and 5.2 show good agreement between all the results, with the exception of pitch-pitch damping. The coupling coefficients show better agreement in pitch due to heave (Figure 5.3) than heave due to pitch (Figure 5.4). For a symmetric hull, it is common to observe symmetry in the forward speed coupling coefficients ($A_{ij} = -A_{ji}, B_{ij} = -B_{ji}$ for $i \neq j$). This is exactly the case
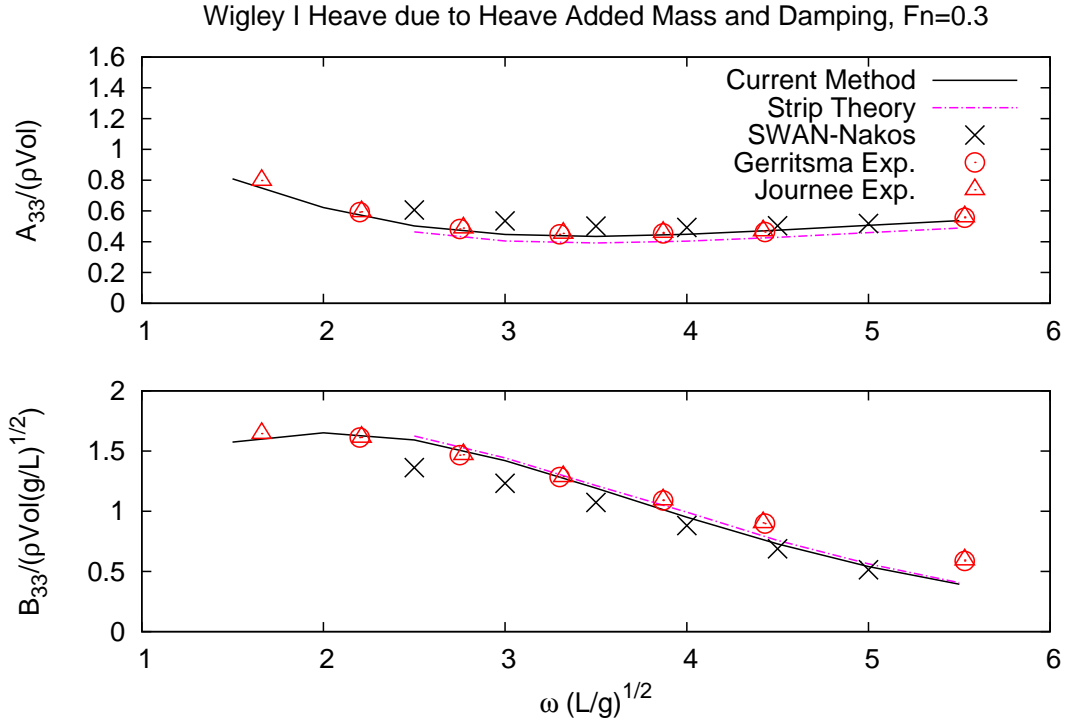
Figure 5.1: Wigley I Heave Hydrodynamic Coefficients, $Fn = 0.3$

for linear strip theory, as can be seen in the equations above. Timman and Newman (1962) also showed this holds for symmetric, slender hull shapes, where the error is of the same order as the slenderness of the hull. The current method does not exhibit this property. The differences may be due to the use of numerical estimation of the $\frac{\partial \phi}{\partial x}$ term in the pressure equation.

The same coefficients are calculated for the Wigley III hull form and shown in Figures 5.5 through 5.8. An alternative set of solutions is shown using the formulation of Ogilvie and Tuck (1969), as described earlier. Other comparisons include the code SHIPMO, a six dogree-of-freedom linear strip theory based on Salvesen et al. (1970) developed by Beck and Troesch (1989), the three-dimensional body-exact method of Zhang (2007), and experimental results by Journée (1992).

The diagonal coefficients, in Figures 5.5 and 5.6 show good agreement, again with the exception of the pitch-pitch damping coefficient. The pitch-heave coupling
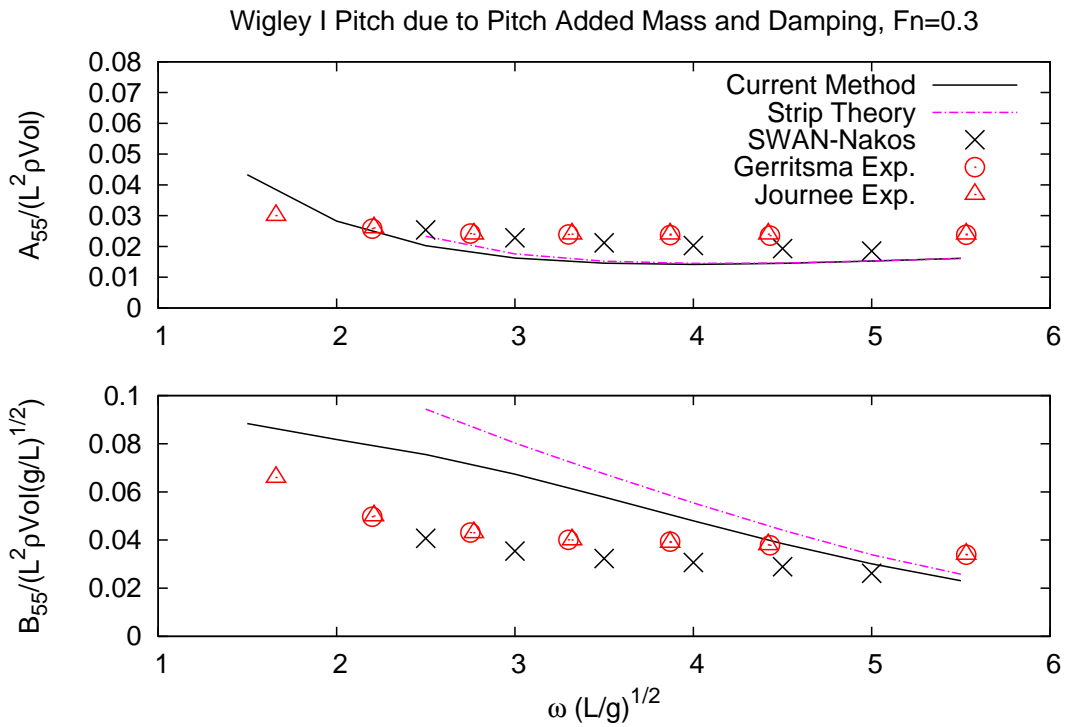
Figure 5.2: Wigley I Pitch Hydrodynamic Coefficients, $Fn = 0.3$
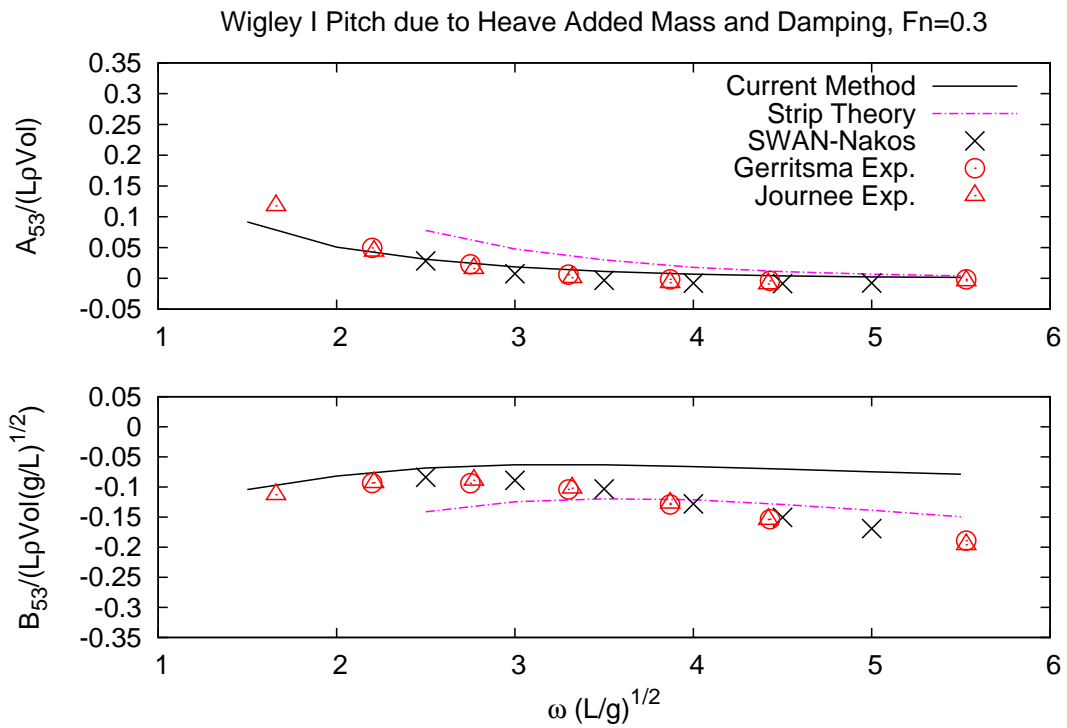
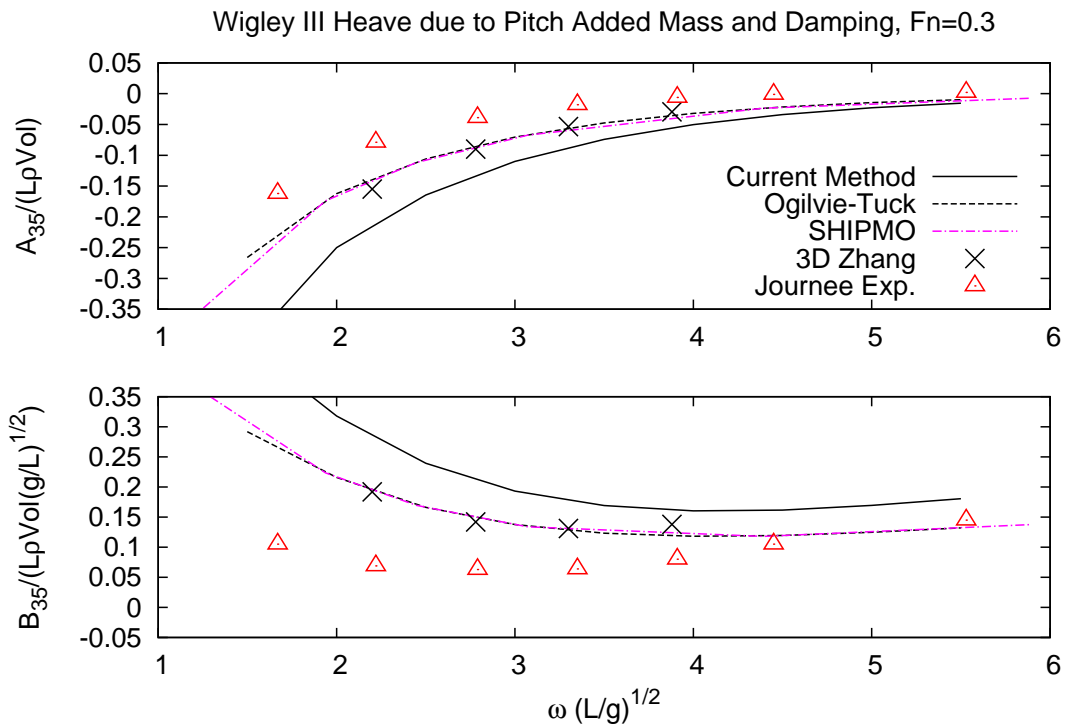Figure 5.3: Wigley I Pitch-Heave Hydrodynamic Coefficients, $Fn = 0.3$
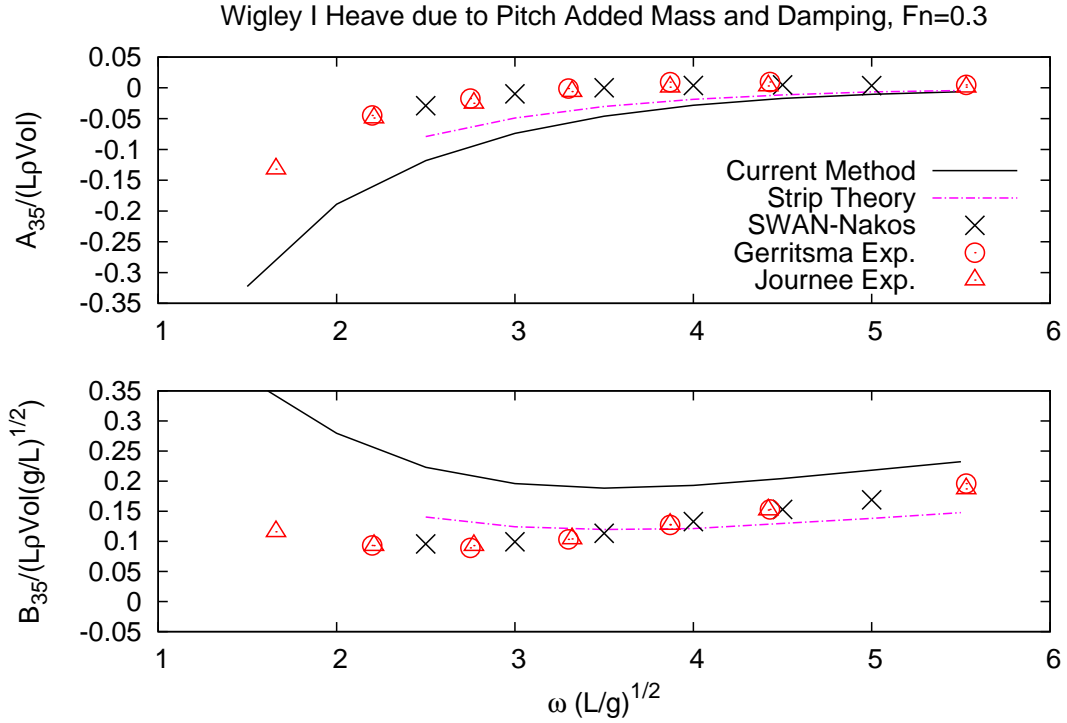
Figure 5.4: Wigley I Heave-Pitch Hydrodynamic Coefficients, $Fn = 0.3$

terms in Figure 5.7 show improved agreement over strip threory when compaing to experiments, while the opposite is true for the heave-pitch coupling terms in Figure 5.8. The current results do not exhibit the symmetric property of $A_{53} = -A_{35}, B_{53} = -B_{35}$, as is the case for linear theory.

In all the Wigley III results, Figures 5.5 through 5.8, excellent agreement can be seen between the Ogilvie-Tuck method and linear strip theory SHIPMO. This isolates the difference between the current method and classical strip theory in how the forward speed effects are handled. Although the symmetry property may be appealing from a validation standpoint, it is based on assumptions and linearizations which are inconsistent, especially when considering a body-nonlinear approach. For these reasons, we justify the use of the current method, being cautious of the use of numerical techniques to estimate $\frac{\partial \phi}{\partial x}$. Perhaps a more sophisticated method might be used to improve the results.
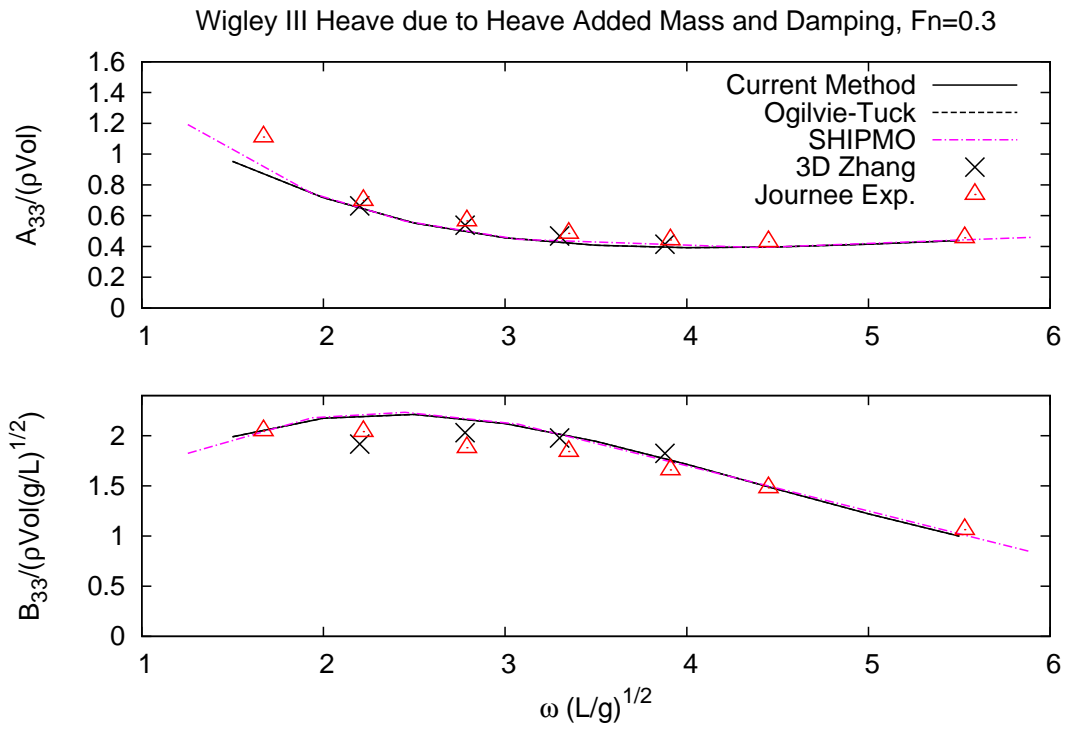
Figure 5.5: Wigley III Heave Hydrodynamic Coefficients, $Fn = 0.3$
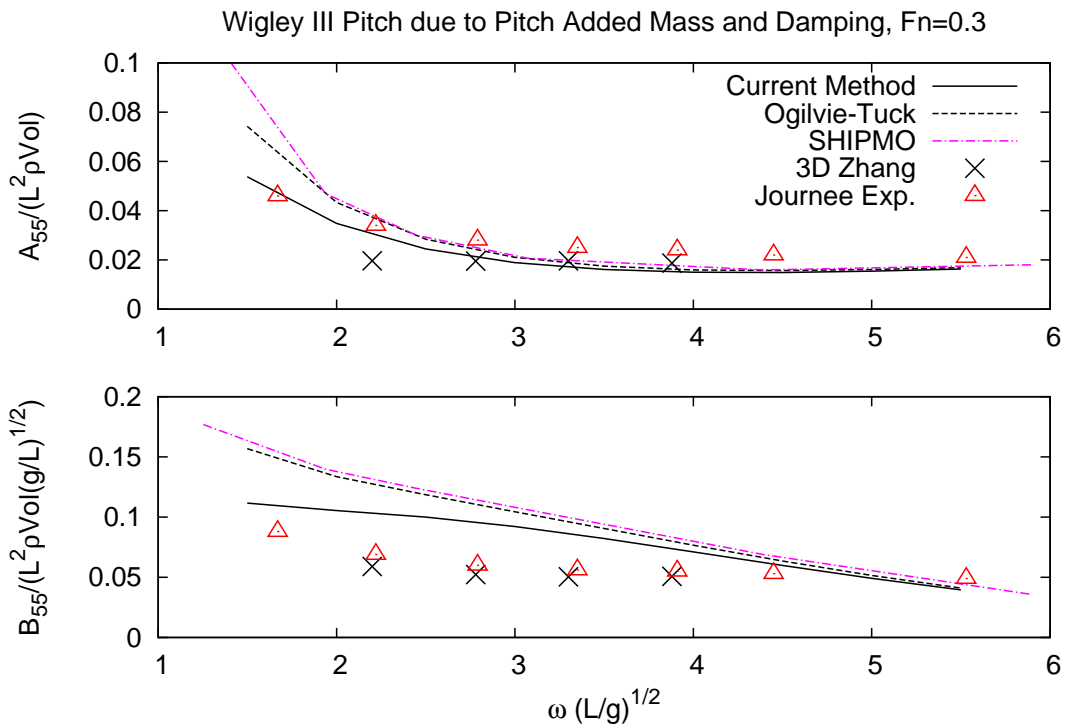
Figure 5.6: Wigley III Pitch Hydrodynamic Coefficients, $Fn = 0.3$
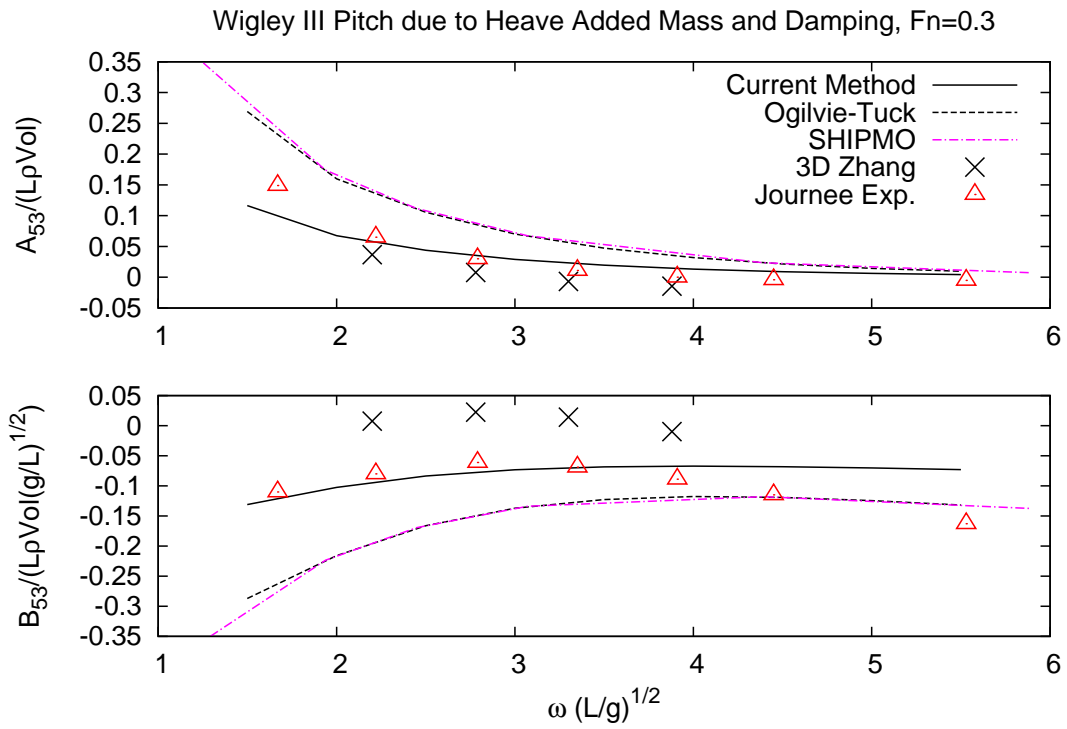
Figure 5.7: Wigley III Pitch-Heave Hydrodynamic Coefficients, $Fn = 0.3$

Figure 5.8: Wigley III Heave-Pitch Hydrodynamic Coefficients, $Fn = 0.3$

5.2 Wave Exciting Forces

The exciting force problem is validated using the Wigley I hull with forward speed of $Fn = 0.3$. The hull is fixed to the translating hydrodynamic frame. The incident wave field is for regular head seas, where the waves travel from the bow to the stern with some given wavelength or frequency. The heave force and pitch moment time-series are transformed into an amplitude and phase, relative to the wave crest at the origin. The results are shown in Figures 5.9 and 5.10.

The current method is compared to the strip theory and SWAN codes from MIT, as described earlier and available in Nakos (1990), and experimental results from Gerritsma (1988) and Journée (1992). Two sets of experimental results are available from Journée (1992), corresponding to "small" and "large" average wave amplitudes across the range of wavelengths. Even the large wave amplitudes, which are less than 30% of the draft, may be considered for linear comparisons since the Wigley models have a constant draft along their length, are wall-sided above the waterline, and nearly wall-sided below the waterline.

All the results show very good agreement, and the current method shows better comparison to experimental results than the linear strip theory for the pitch moment.

5.3 Large Amplitude Radiation

The body-exact approach is able to capture nonlinear forces due to large amplitude motions. This was validated for the two-dimensional problem earlier. The same approach is used in the strip theory model. We examine the effects of motion amplitude on the forces and moments acting on the body. The vessel used is a naval destroyer, hull model m5514. The particulars are listed in Table 5.1 and some images are shown in Figure 5.11. The bulbous bow and flat transom stern make this hull a good choice to test the effects of body shape on nonlinear forcing.
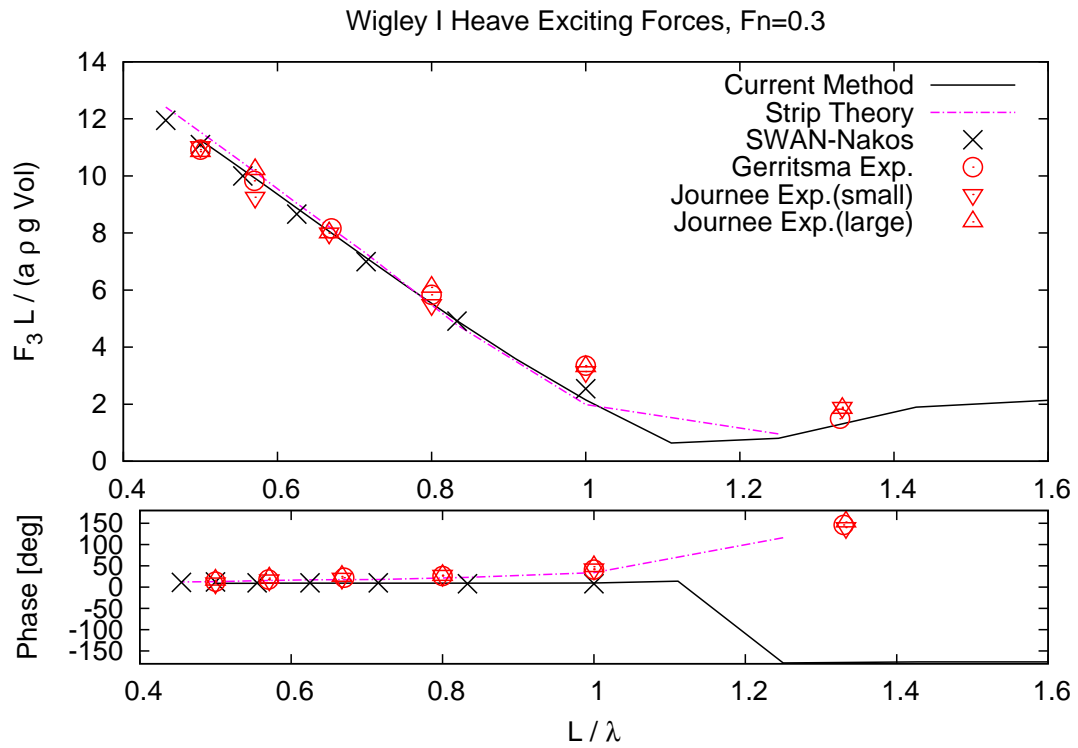
Figure 5.9: Wigley I Heave Exciting Force in Head Seas, $Fn = 0.3$
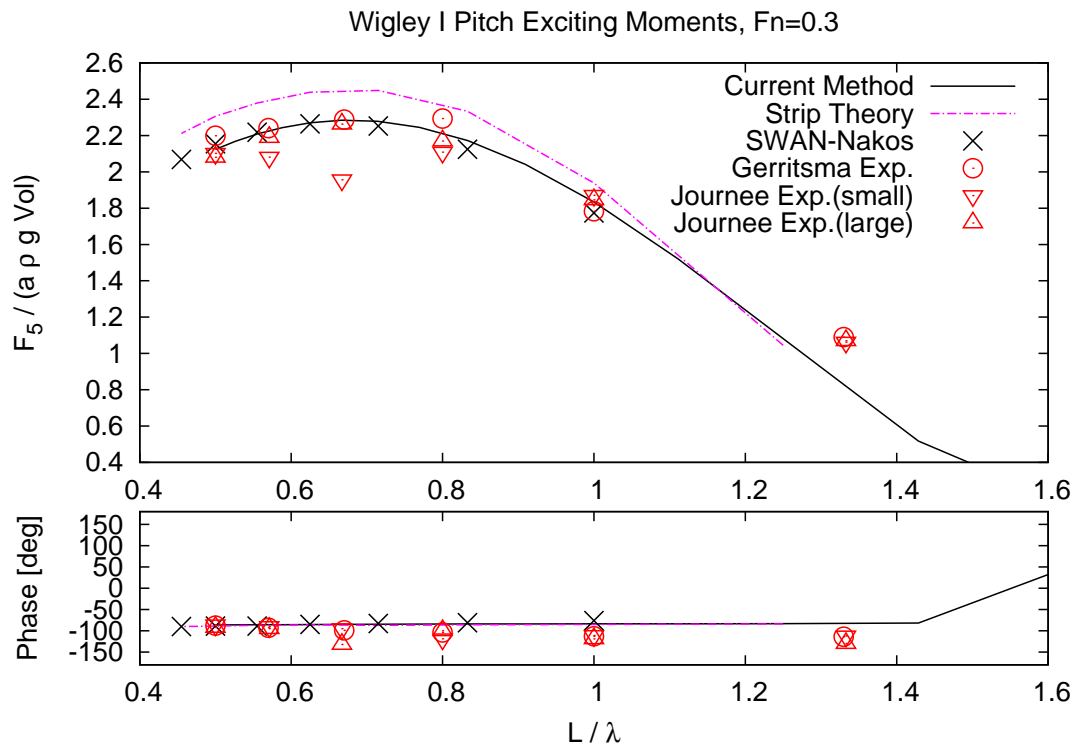
Figure 5.10: Wigley I Pitch Exciting Moment in Head Seas, $Fn = 0.3$
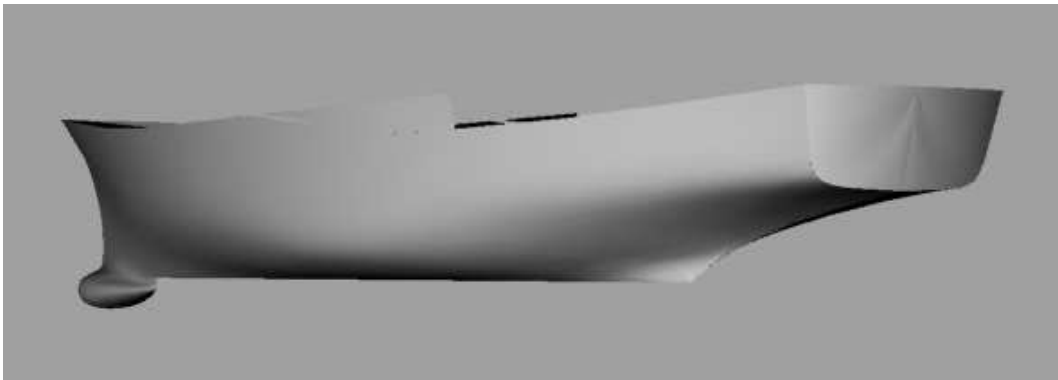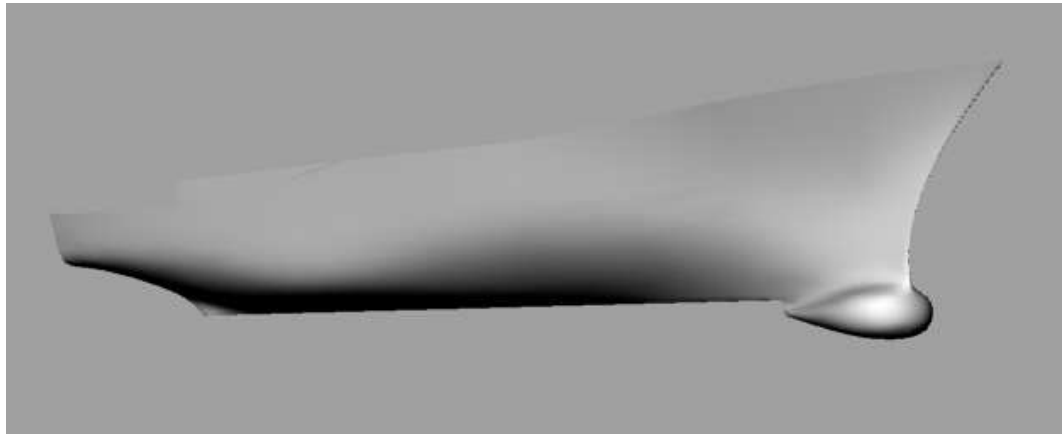
Figure 5.11: Views of m5514 (Naval Destroyer) Hull

The test case will be forced pitch motions with varying amplitudes of 1, 2.5, and 5 degrees. The results of the time-simulations are shown in Figures 5.12 and 5.13, for a low and high frequency case. The low frequency ($\omega = 0.3831$) corresponds to ship generated, or radiated, wavelengths of $420m$, while the high frequency ($\omega = 1.1$) corresponds to $50m$ radiated wavelengths. In each figure, the heave force and pitch moment is plotted against time, and separated into hydrostatic (HS) and radiated (RAD) components. The three cases are plotted together, and scaled by dividing the forces and moments by the amplitude of motion.

The hydrostatic terms are independent of frequency, while the radiation terms are more significant at the higher frequency, as expected. The hydrodynamic terms become more asymmetric and nonlinear as the amplitude of motion increases. The high frequency heave force due to pitch, shown at the top of Figure 5.13, shows significant nonlinearities with increasing amplitude because of the changing body shape. The flat transom stern sections exit (around 11.5s) and re-enter (around 14s) the water. The bulb nearly comes out of the water when the pitch angle reaches its negative maximum (around 10s). The body geometry must be considered in these large motions.

As an example of the improved techniques presented in this approach, the same computations are performed using the simplified method of numerically differentiating to find $\frac{\partial \phi}{\partial t}$. The backwards differencing scheme used produces a very noisy time-series, as shown in Figures 5.14 and 5.15. More spikes are present due to the adding and removing of panels. These problems can be addressed by using better numerical techniques, or using the acceleration potential, as described earlier.

The final case for comparison uses the same test conditions with a different hull form. The hull used here is an ONR tumblehome model, m5613. The particulars can be found in Table 5.1, and images are given in Figure 5.16. This hull has similar bulbous bow and transom stern characteristics, while also having a very pronounced
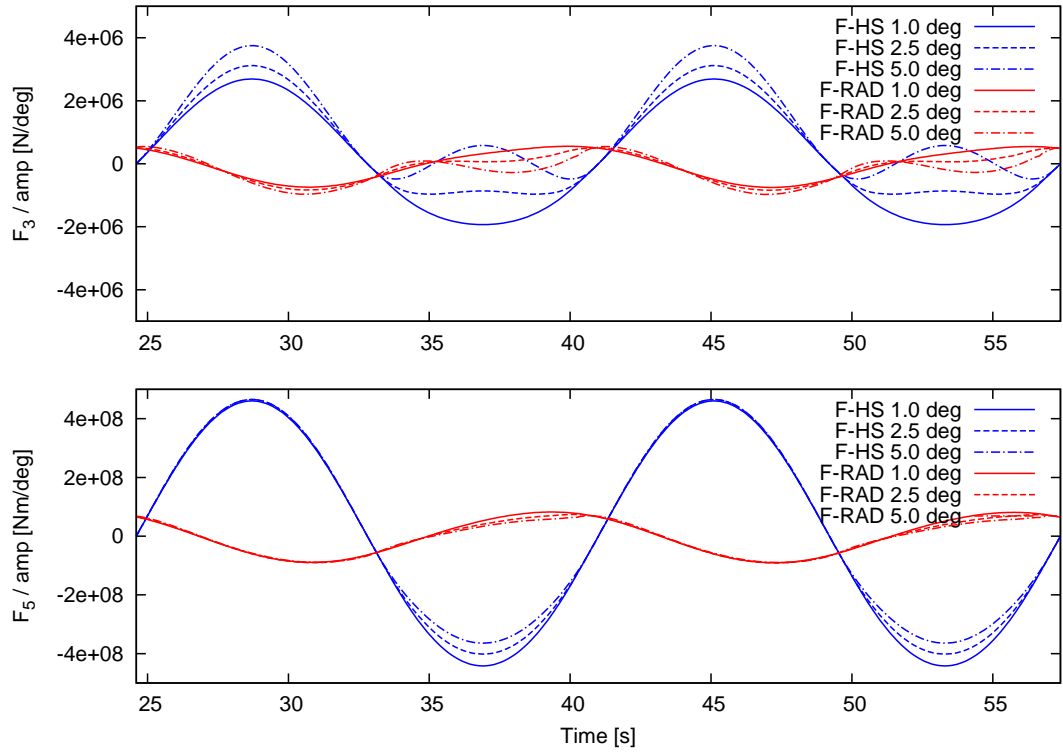
Figure 5.12: m5514 Forced Pitch, $\omega = 0.3831 rad/s$

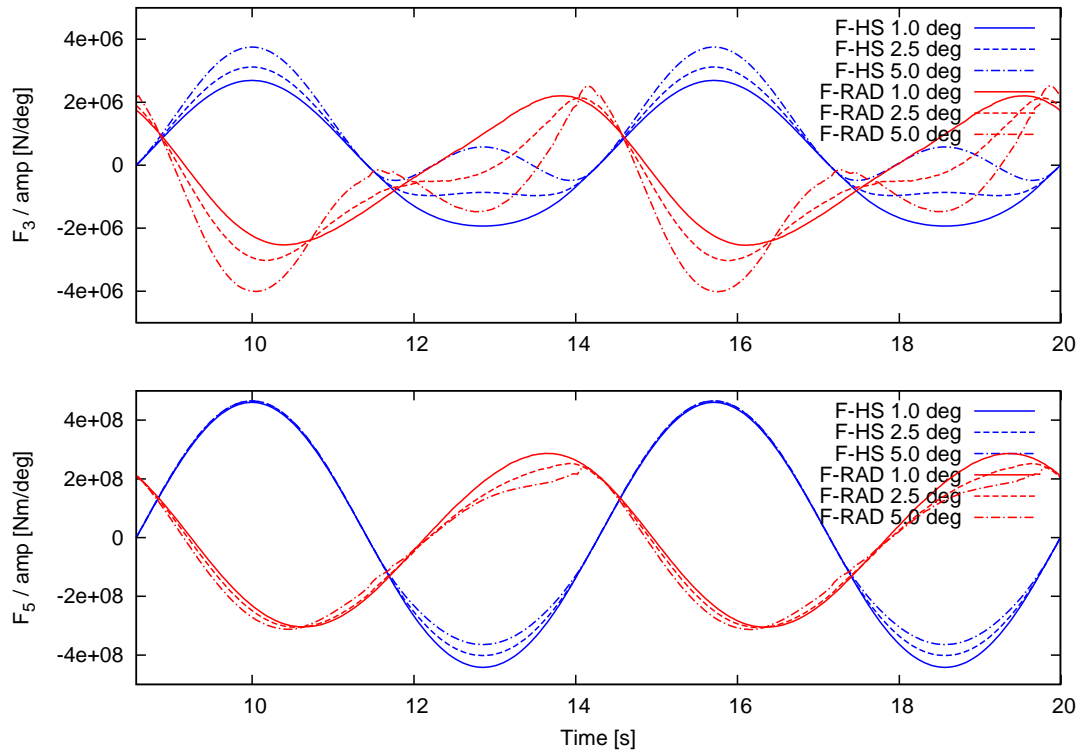Figure 5.13: m5514 Forced Pitch, $\omega = 1.1000 rad/s$
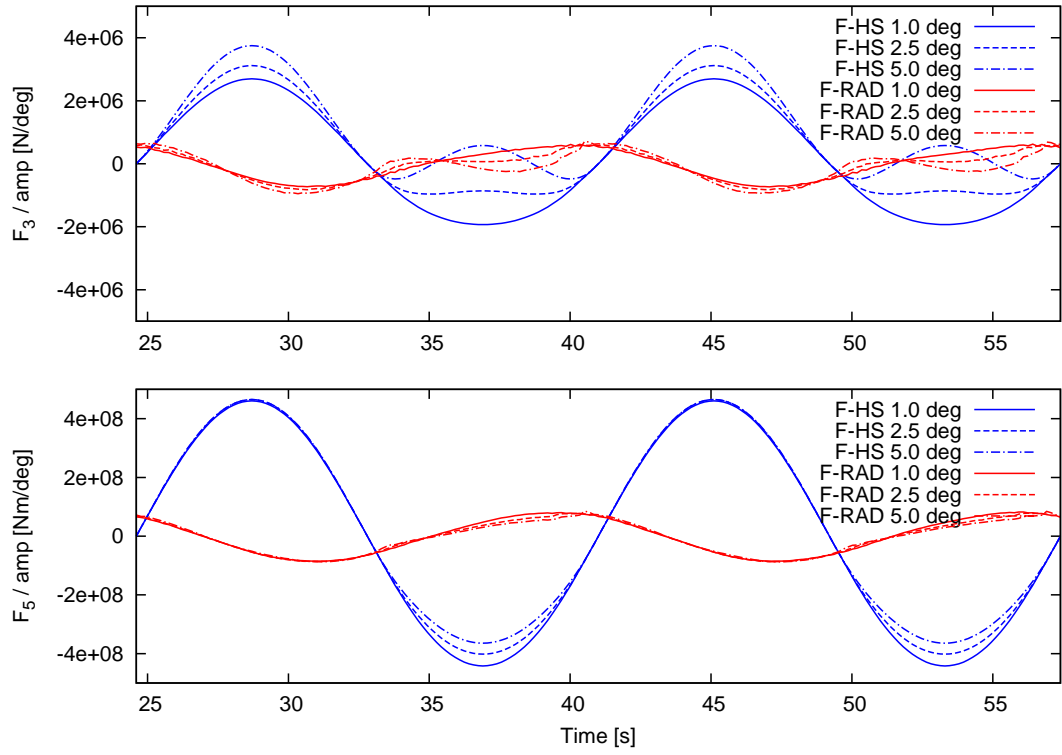
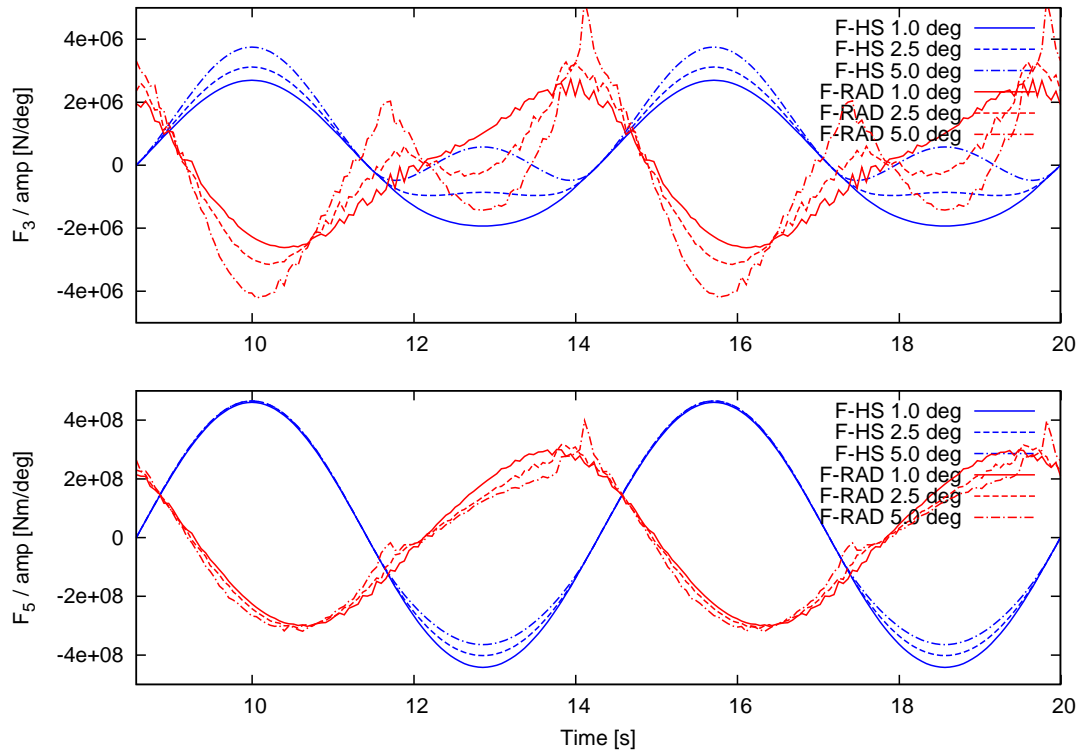Figure 5.14: m5514 Forced Pitch (Backward Diff), $\omega = 0.3831 rad/s$

Figure 5.15: m5514 Forced Pitch (Backward Diff), $\omega = 1.1000 rad/s$

76

tumblehome throughout the entire length of the vessel. This makes for interesting seakeeping characteristics in heavy seas.

The low-frequency case shows some interesting results as the amplitude increases. The more interesting results, in Figure 5.18, are the high frequency radiation forces when the nearly flat transom stern sections exit (around 11.5s) and re-enter (around 14s) the water, producing significant spikes in the heave force. The changing water-plane area significantly affects the hydrostatic and hydrodynamic components of the pressure on the hull surface, and must be considered when the motions become large.
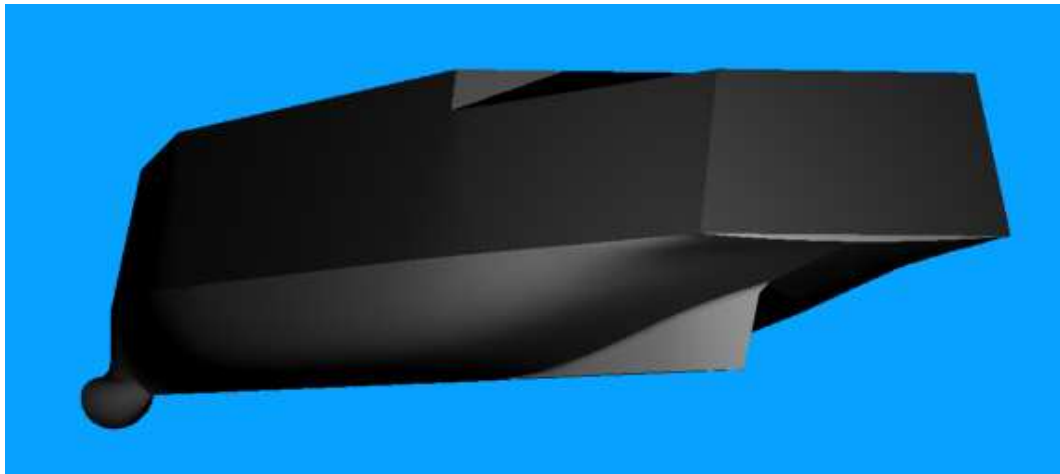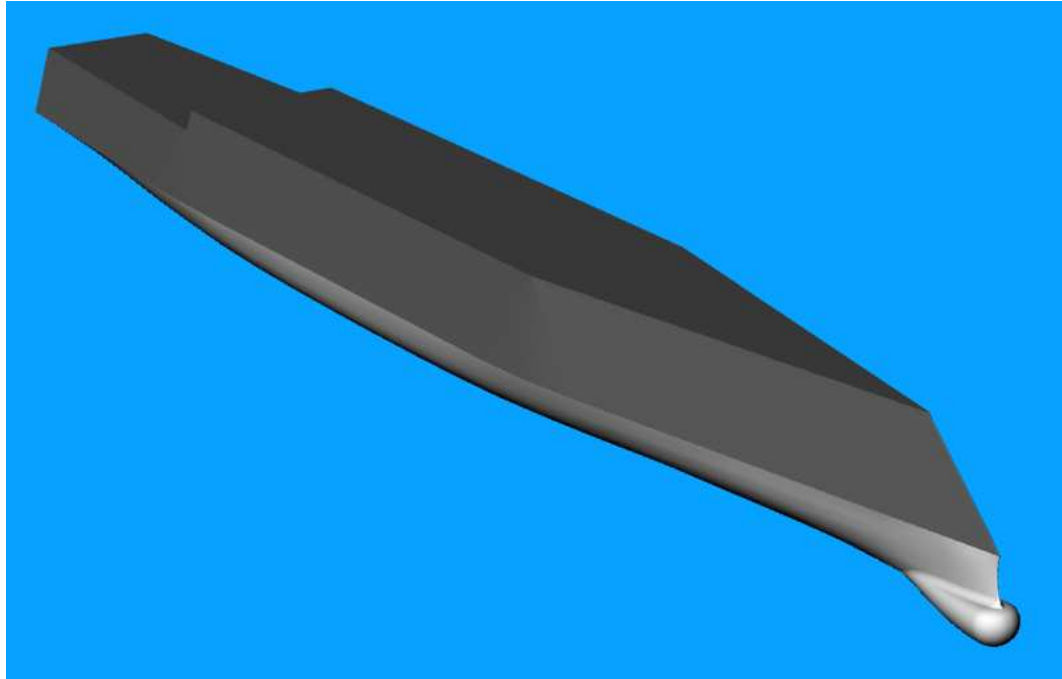
Figure 5.16: Views of m5613 (ONR Tumblehome) Hull
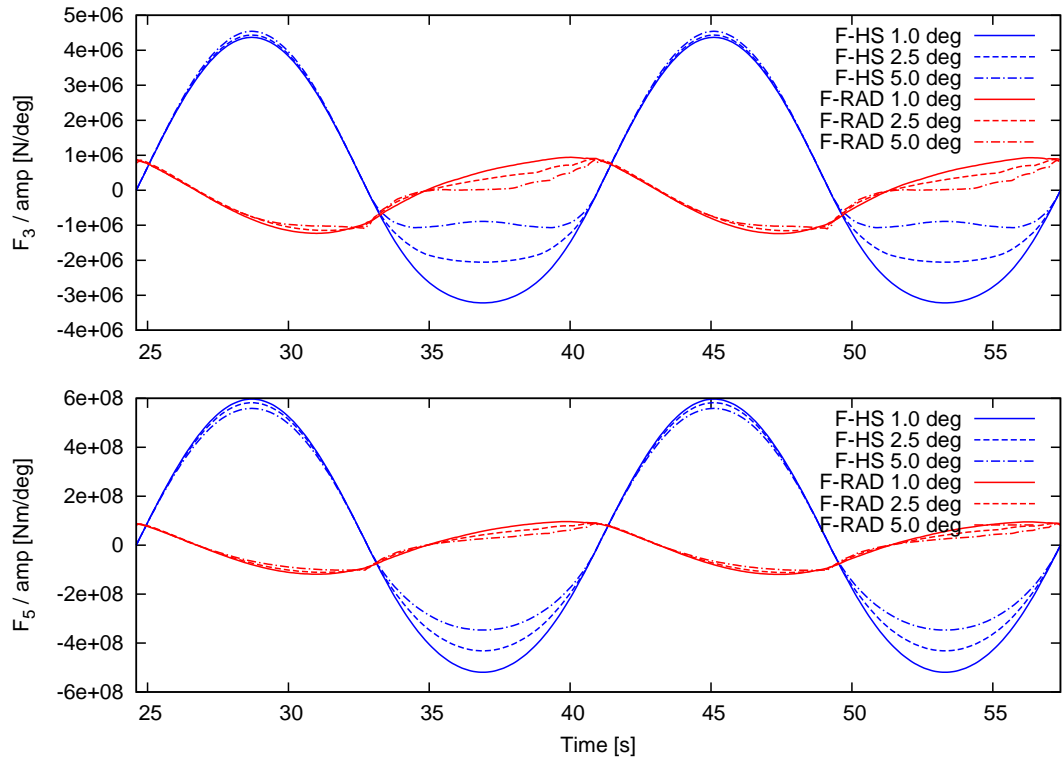
Figure 5.17: m5613 Forced Pitch, $\omega = 0.3831 rad/s$
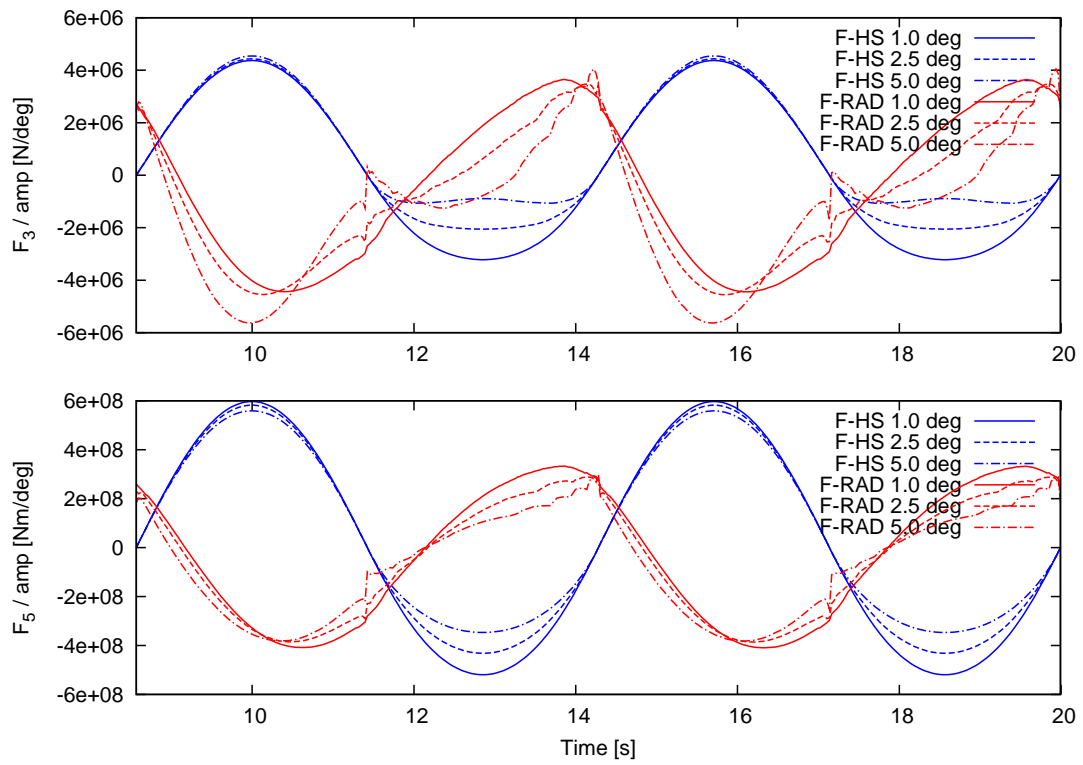
Figure 5.18: m5613 Forced Pitch, $\omega = 1.1000 rad/s$

CHAPTER VI

Free Motions

6.1   Nonlinear Equations of Motion

The hydrodynamic problem and rigid body equations of motion are solved simultaneously in the time-domain. The nonlinear equations of motion described in Chapter II must be validated. Small amplitude waves can be used to excite the body, which is now free to move. The type of ramp function used to evolve the free surface (which begins by being completely calm) will affect the resulting motions. Typically, a ramp over at least three periods is used for free motion problems. Several periods later, the body starts to settle into sinusoidal motion and an amplitude and phase can be determined.

The first model used for comparison is the Series-60 hull form with a block coefficient $C_B = 0.70$. The particulars can be found in Table 5.1. The vessel is exposed to regular head seas, and will begin to surge, heave, and pitch. The current method is compared to the strip theory and SWAN codes from MIT, as described earlier and available in Nakos (1990), and experimental results from Gerritsma et al. (1974). The surge results are not available because the model was restrained in surge, so only heave and pitch are shown in Figures 6.1 and 6.2.

The current method shows good agreement, except for over-estimating the resonant peak in heave. This may be related to inaccuracies in the hydrodynamic coupling
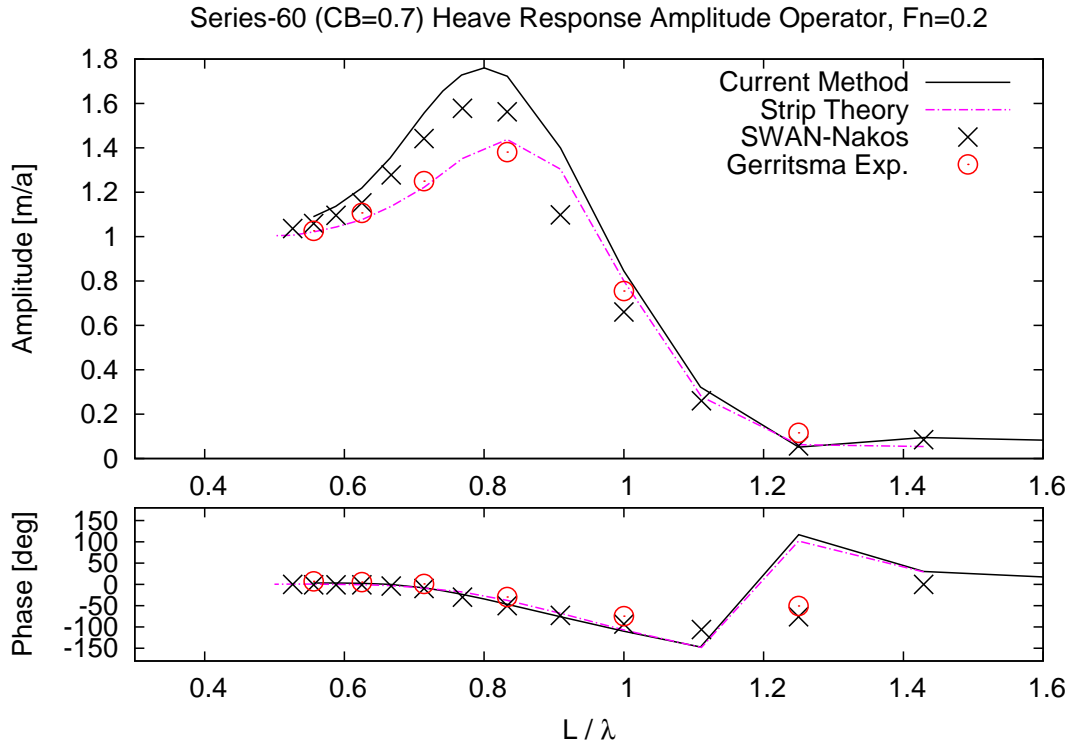
Figure 6.1: Series-60 (CB=0.7) Heave RAO in Head Seas, $Fn = 0.2$

terms, as discussed in Chapter V. The pitch motions are predicted very accurately, showing better agreement than the SWAN code. It also seems that the pitch peak has been shifted in the right direction using the current method, as compared to the linear strip theory.

An extensive comparison of experimental and computational results for this Series-60 hull is available in Bailey et al. (2001), including the hydrodynamic coefficients, exciting forces, and response amplitude operators.

Typically, experimental results for free motions are limited to the vertical plane, or surge, heave, and pitch. The remaining horizontal plane motions, namely sway and yaw, have no restoring mechanisms and viscosity is very important. This is especially true for the cases with forward speed, where the vessel would drift off course if it weren't restrained in sway and/or yaw. With that in mind, the remaining degrees-of-freedom may be validated by comparing to linear theory.
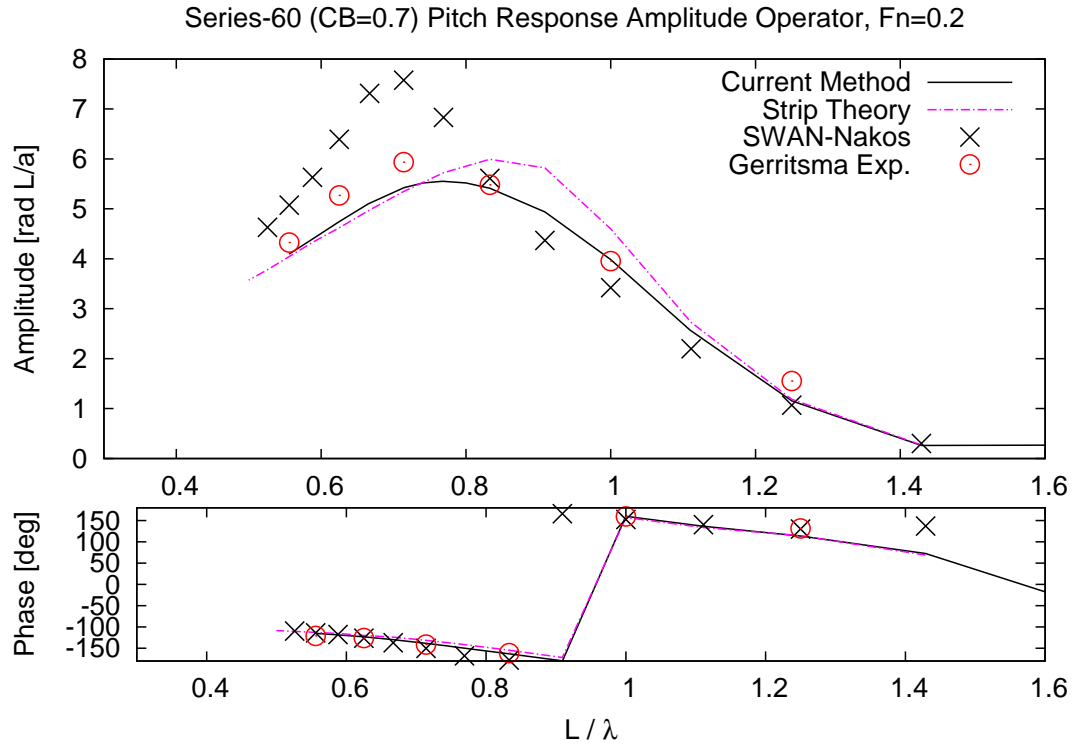
Figure 6.2: Series-60 (CB=0.7) Pitch RAO in Head Seas, $Fn = 0.2$

The next series of results are for the S-175 containership in regular waves with and without forward speed. SHIPMO, developed by Beck and Troesch (1989), is the six degree-of-freedom linear strip theory code used as a comparison. The current method, Ogilvie-Tuck approximation, and the momentum formulation results are computed and compared. The Ogilvie-Tuck approximation is the same method as described in Chapter V and the momentum formulation is described in Appendix A.

The current method and its two alternatives are subject to exactly the same boundary conditions and numerical schemes, differing only in how they treat the speed-dependent components of the problem. An extensive set of test parameters are used, including wave heading angles around the entire ship at increments or 45°, forward speeds of $Fn = 0.0, 0.2$, and absolute wavelengths of from $L/3$ to $5L$.

Figures 6.3 through 6.5 show the responses for head seas. The zero-speed results, shown in blue, are nearly identical. The forward speed results show fairly good
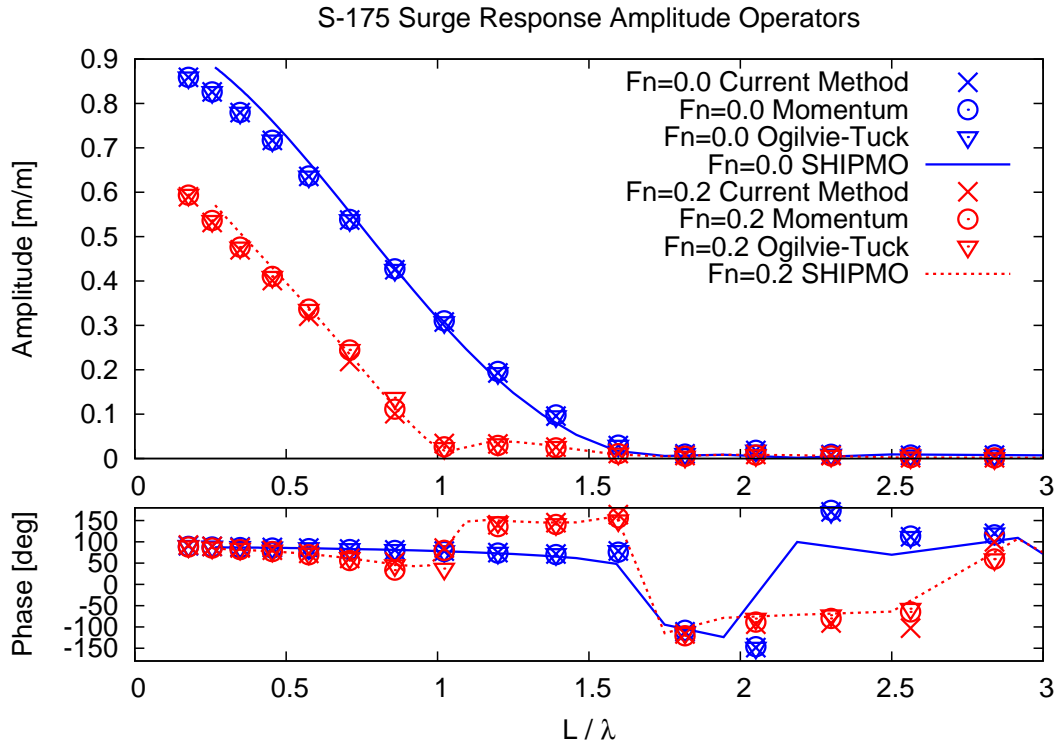
Figure 6.3: S-175 Surge RAO in Head Seas

agreement between all the methods, except at the resonant peaks of heave and pitch. The momentum formulation overestimates both of the peaks. The current method, using direct pressure integration, overestimates the peak heave motions. Using the Ogilvie-Tuck approach highlights the difference between the two: the treatment of speed-dependent terms.

Figures 6.6 through 6.11 show a more interesting case of stern-quartering seas, where all six degrees-of-freedom are excited and unrestrained. The surge, heave, roll, and pitch motions agree very well. The sway and yaw, in Figures 6.7 and 6.11, show some significant differences. This is due to the fact that the current method is a time-domain initial boundary value problem. The viscous corrections and simple controllers for sway and yaw motions should not affect the motions too significantly. However, any differences introducing during the startup or ramping phase will propagate in time, and affect the resulting long-term responses. The horizontal modes
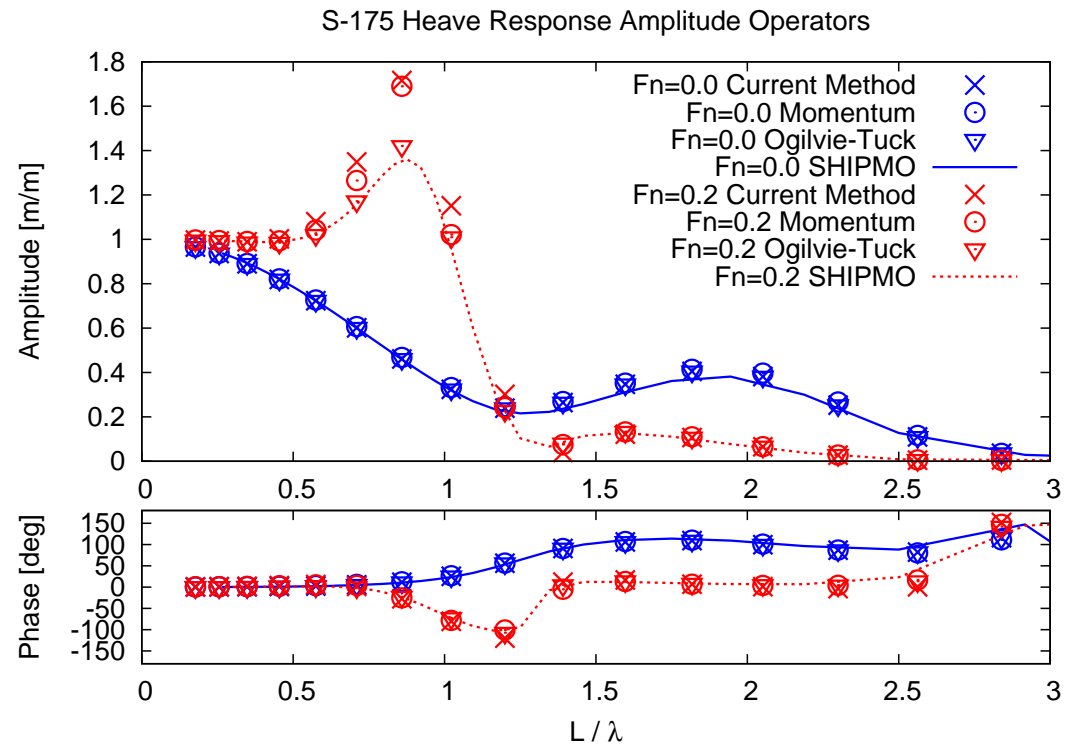
Figure 6.4: S-175 Heave RAO in Head Seas
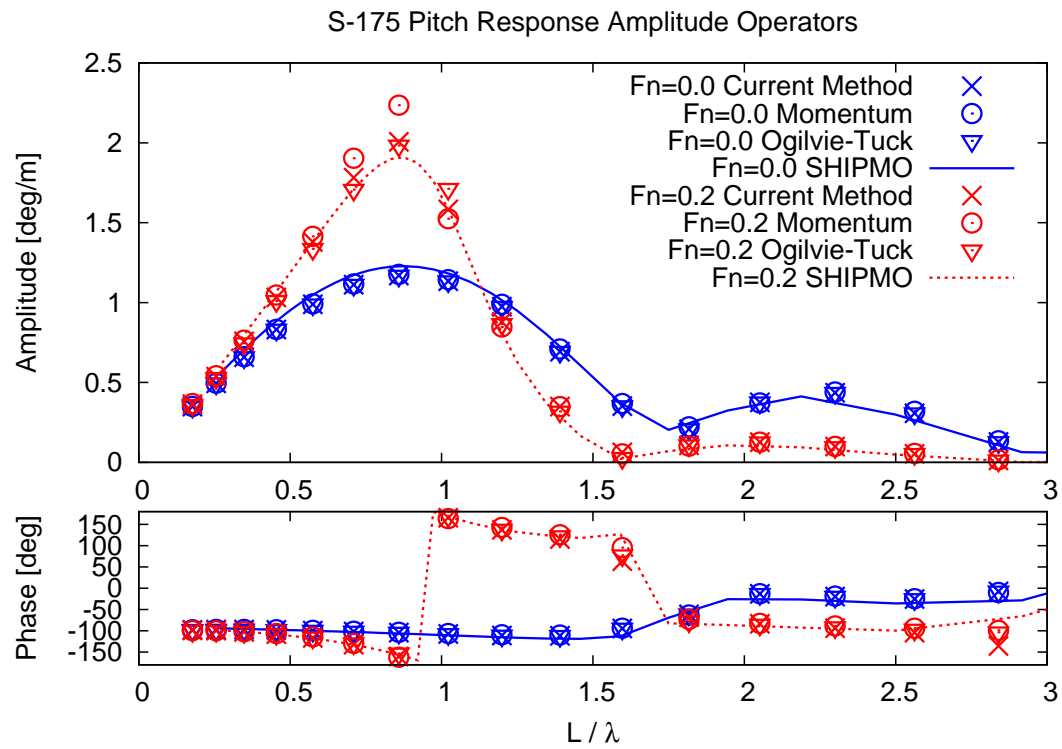
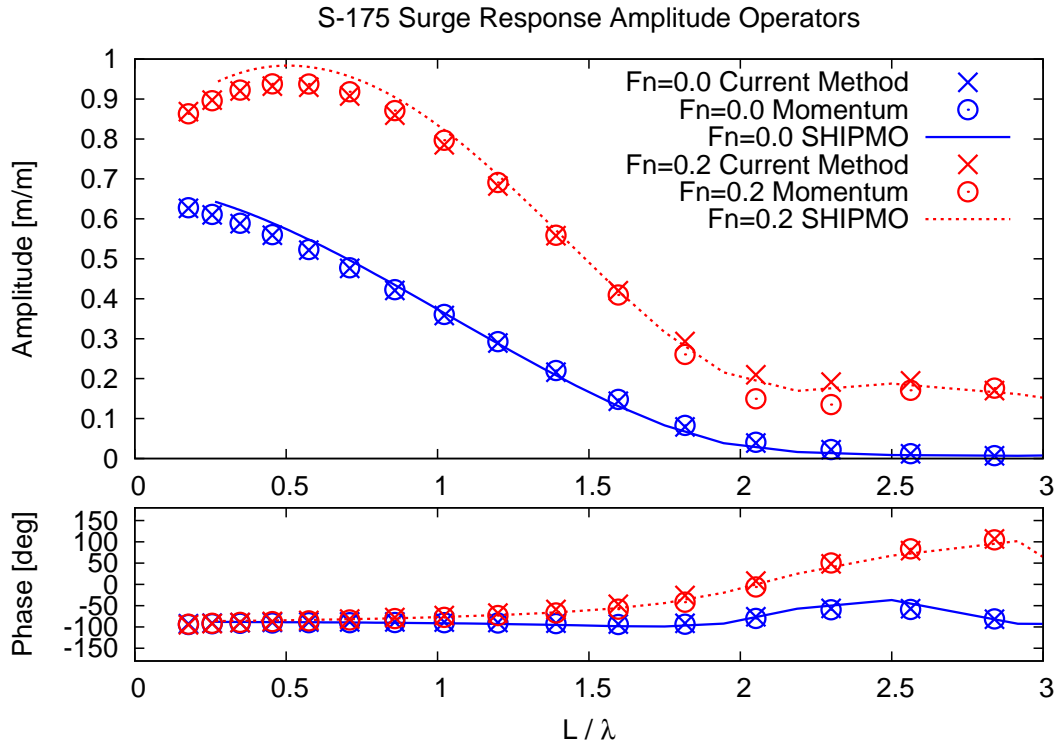Figure 6.5: S-175 Pitch RAO in Head Seas

Figure 6.6: S-175 Surge RAO in Stern Quartering Seas

have no restoring mechanisms. Any differences are difficult to control and may lead to significantly different motions.

The remaining runs (for following, beam, and bow quartering seas) are available in Appendix D. The direct pressure and momentum formulations agree fairly well. The agreement with SHIPMO must be considered on a case-by-case basis. However, the momentum formulation, as derived, may not be suitable for large amplitude motions. This is briefly discussed in Appendix A
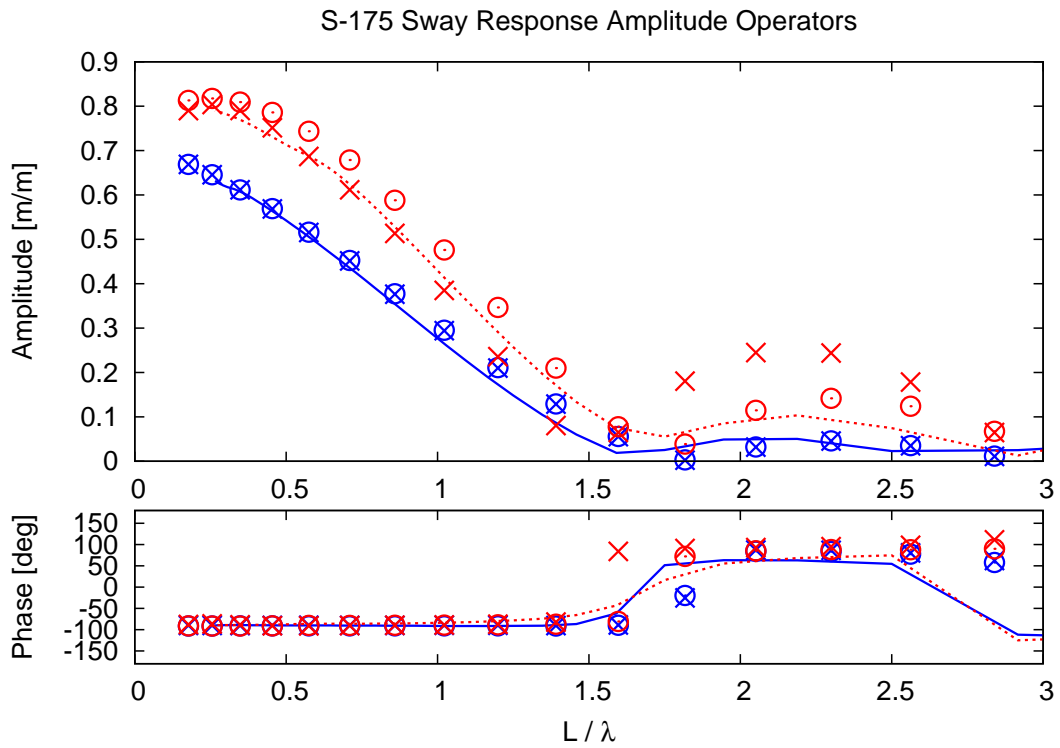
Figure 6.7: S-175 Sway RAO in Stern Quartering Seas
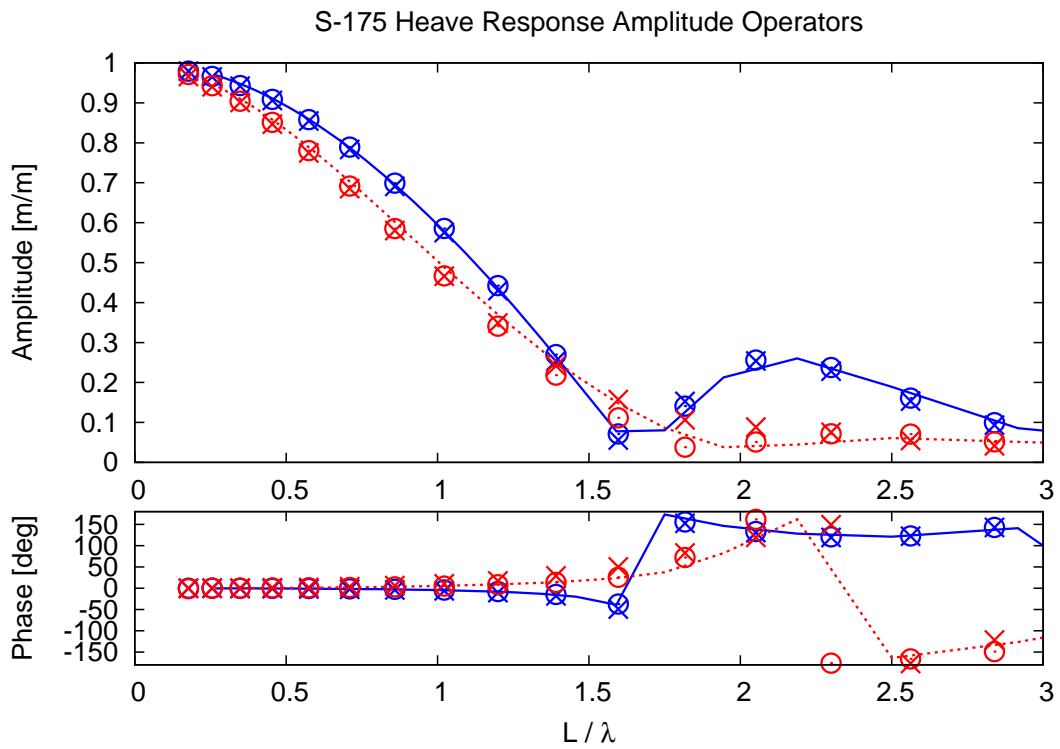
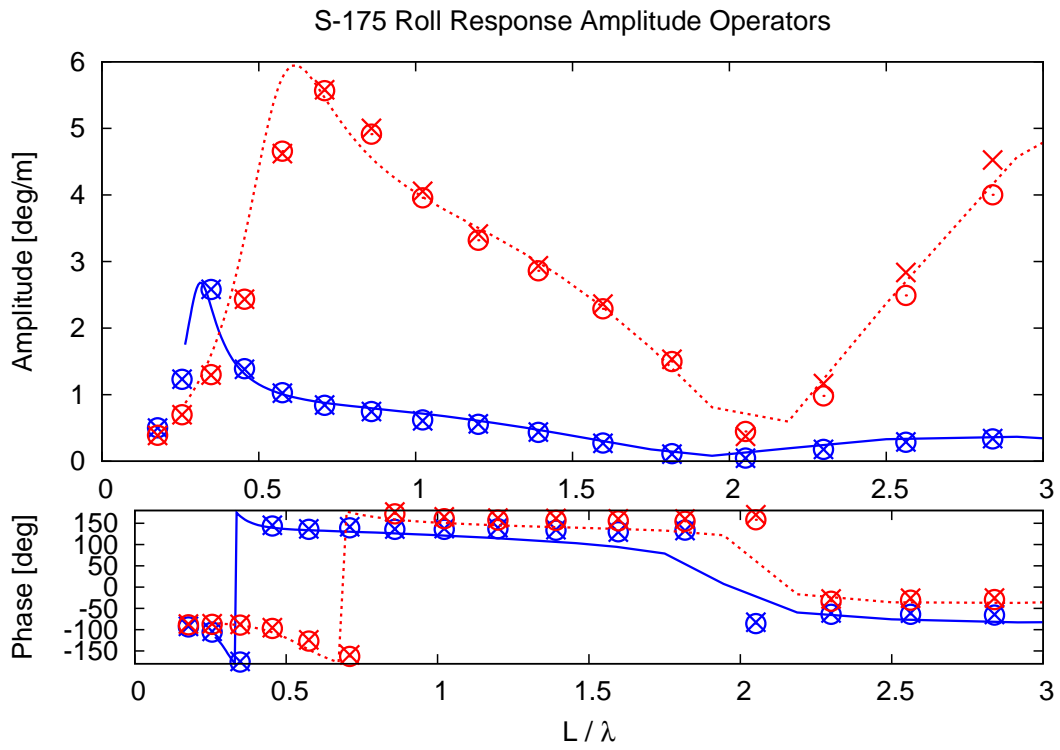Figure 6.8: S-175 Heave RAO in Stern Quartering Seas

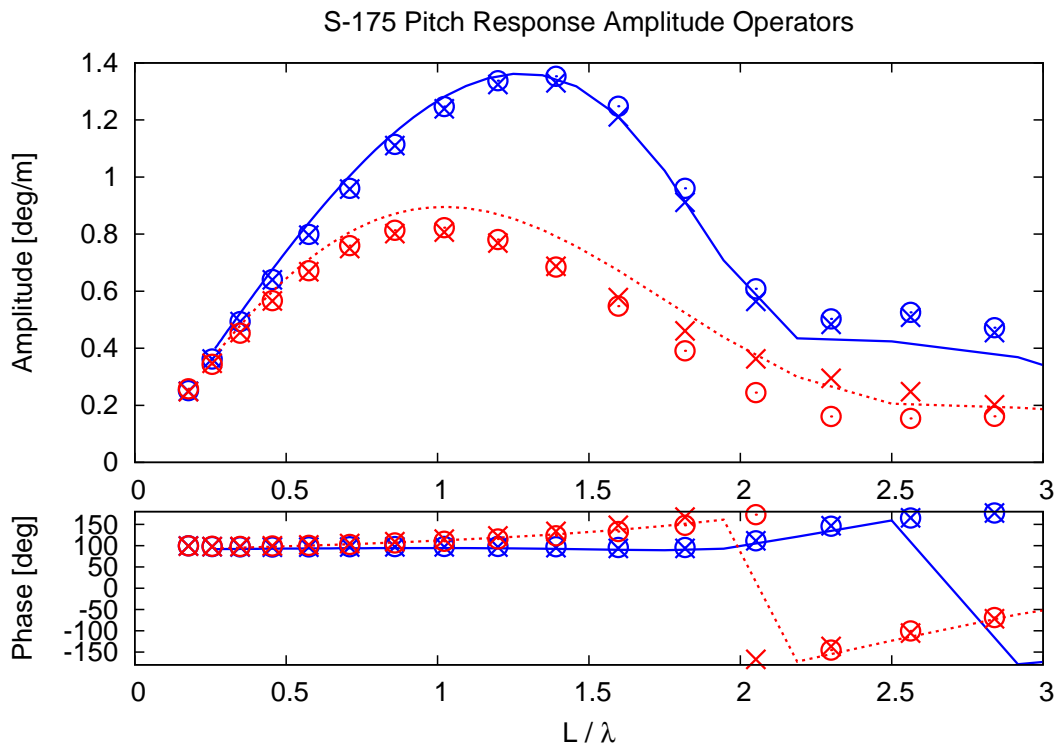Figure 6.9: S-175 Roll RAO in Stern Quartering Seas

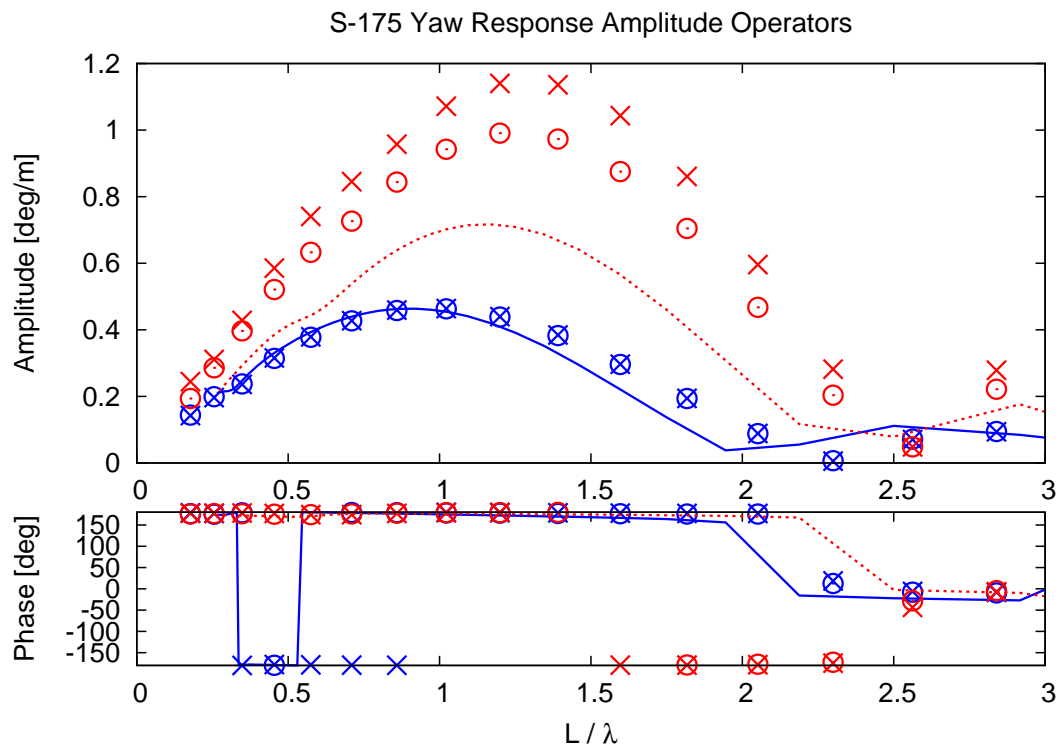Figure 6.10: S-175 Pitch RAO in Stern Quartering Seas

Figure 6.11: S-175 Yaw RAO in Stern Quartering Seas

CHAPTER VII

Discussion

7.1 Conclusions

The body-exact strip theory presented shows very encouraging results. Convergence tests have been carried out, as well as small and large amplitude validations for the two-dimensional problem. The strip theory has been demonstrated to give good predictions, with a few exceptions. Some of these poor comparisons might be improved if better techniques were used to account for the interaction between sections, which becomes important with forward speed.

The computation speed is very fast, executing near real-time (or better) on a high-end desktop PC. The numerical methods still have room for improvement as far as speed is concerned. The single most intensive portion of the code is the influence matrix inversion. This is needed for the two-dimensional boundary value problem(s) and the influence matrix when using Radial Basis Functions. The latter has the most room for improvements.

The robust capabilities of this method make it a good candidate for large motion simulations of any hull form that meets the slender-body requirements. Loading the hull offsets is straightforward, and a wide range of analyses is available.

7.2 Recommendations

The free surface grid described is fixed and depends on the length scale of the body. It is able to resolve wave frequencies in the range of interest. However, only regular waves were used in the results shown. There is no reason why we could not go to irregular waves, it was simply outside the scope of this research. The free surface grid and linearized boundary conditions make this a good candidate for simulating random seas in the time-domain.

The computational simulations presented in this dissertation are carried out for no longer than 10-15 periods, usually needed for free motions. Forced motions and exciting forces are usually done for even shorter durations. The introduction of the maneuvering and controller models requires that simulations be carried for 30 or more periods (based on the characteristic seakeeping frequencies). Park (1992) gives a detailed description of the desingularized free surface method, including the numerical beach used, and concludes that simulations will break down after 15-20 periods. After enough time has passed, fluid may leak into or out of the domain through the boundary. It is unclear whether this is due to the discretization in the numerical beach region, the desingularization scheme, or the open boundary. This must be investigated if the simulations are to be continued for longer durations, characteristic of the maneuvering problem. Scullen (1998) describes the numerical stability of the desingularized approach, and may offer some insight.

The simple controller used in these simulations is necessary to keep the ship from drifting off-course, as discussed earlier. The forces and moments it generates may be unrealistic. It is suggested that an automatic controller be used to keep the vessel on course. Models that would be suitable for this are described in Fossen (1994). Li et al. (2009) examine a path following controller using a four degree-of-freedom system. The current method hydrodynamic and rigid body equations of motion models are very well suited to utilize such a controller.

Finally, allowing the hydrodynamic frame to accelerate and rotate would be required to solve the combined seakeeping and maneuvering problem. The case of constant forward speed is important to validate the seakeeping model. However, maneuvering in a wave field should allow the ship to change heading, requiring a rotation of the hydrodynamic frame when using a strip theory.

APPENDICES

APPENDIX A

Momentum Formulation

The momentum formulation requires solving the ϕ problem first. However, the resulting formulas do not calculate the pressure on the body to find the forces and moments. This was derived as an alternative to the direct pressure integration for the "swimming fish" problem by Newman and Wu (1973). The derivation, including a free surface, is shown in Sclavounos (2008). The main difference is the use of $z = 0$ for the free surface conditions, instead of the weak scatterer assumption by Sclavounos. For the two-dimensional problem, the dynamic sectional forces can be approximated by

$$f_i^{DYN} = \int_{C_H} p^{DYN} N_i dl \tag{A.1}$$

$$f_i^{DYN} = -\rho \frac{d}{dt} \int_{C_H} \phi N_i dl - \rho \int_{C_{WP}} (g\zeta^I + \frac{\partial \phi^I}{\partial t}) N_i dl \tag{A.2}$$

where C_{WP} is the exact waterplane contour intersecting the body at that section

For the strip theory approximation, the total dynamic forces and moments can be

written in terms of the perturbation potential

$$F_i^{DYN} = -\rho \int_L dx [\frac{\partial}{\partial t} \int_{C_H} \phi N_i dl - U_o \frac{\partial}{\partial x} \int_{C_H} \phi N_i dl + \int_{C_{WP}} (g\zeta^I + \frac{\partial \phi^I}{\partial t} - U_o \frac{\partial \phi^I}{\partial x}) N_i dl] \quad (A.3)$$

where the sectional integrals are functions of both time and the longitudinal direction (or t and x), so partial derivates must be used.

The speed dependent component of the force is apparent in the second term. Numerically, this is much simpler than approximating $\frac{\partial \phi}{\partial x}$ at every node. A drawback of the momentum approach is that the pressure distribution is not known.

The momentum formulation works well for small amplitude motions. When the motions get large, and the sectional areas change, the evaluation of the time-derivative (or x-derivative if the sections change shape rapidly along the length) becomes problematic. The partial derivatives are brought outside of the sectional integrals, and now the changing integrals along the contour maybe be a function of time, t (or x) themselves.

As an example of this, a simple two-dimensional circular section is used. Oscillating at a frequency $\omega(R/g)^{0.5} = 1.0$, and a radius $R = 10m$, a range of heave amplitudes are used and the added mass and damping are plotted versus amplitude. The results are presented in Figure A.1, where $a'_{33} = a_{33}/(\rho A)$ and $b'_{33} = b_{33}(R/2)^{0.5}/(\rho A)$. The pressure and momentum results are presented, along with experimental results of Vugts (1968). The experimental results were done for small amplitudes, and compare well with linear theory. The linear result is plotted as a constant, independent of motion amplitude.

The results compare well up to about 20% of the radius. This might still be considered a "small" amplitude, especially for the a circular section where the waterplane intersection does not change significantly. As expected, the added mass and damping decrease with amplitude when compared to linear theory. However, the heave damp-
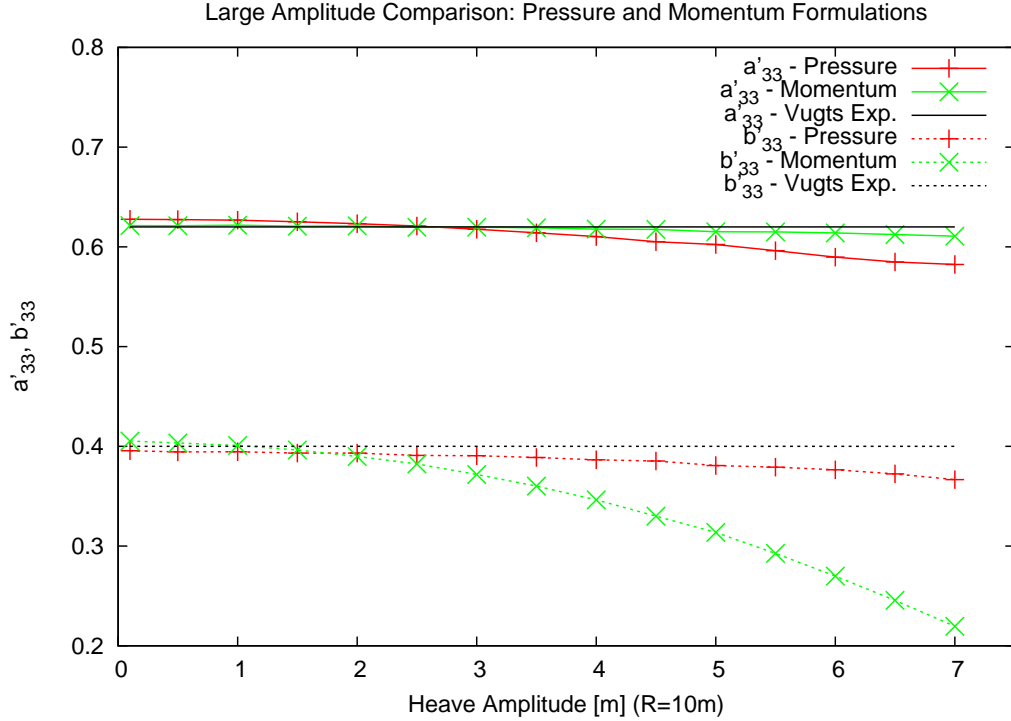
94

Figure A.1: Pressure and Momentum Comparison - Large Amplitude Heaving Circular Section

ing coefficient, b_{33}, seems to change much more significantly with the momentum approach. This emphasizes a possible problem with the method, as derived.

As the amplitude of motion increases, the force time-series should become more nonlinear and the linear coefficients are no longer sufficient to describe them. Figures A.2 through A.4 show the total hydrodynamic heave force acting on the two-dimesnional section with increasing amplitudes of motion (1.0, 4.0, and $7.0m$, where the cylinder radius $R = 10.0m$). As can be seen for the small amplitude case in Figure A.2, the methods agree well and may accurately be described using linear coefficients. However, as the amplitude increases, the force time-series comparisons begin to show significant differences. This confirms the results of the Fourier transform of the first-order terms, shown in Figure A.1. The momentum formulation, as derived, may have some difficulties when the amplitude of motion becomes significant. Further research is needed to investigate these differences.
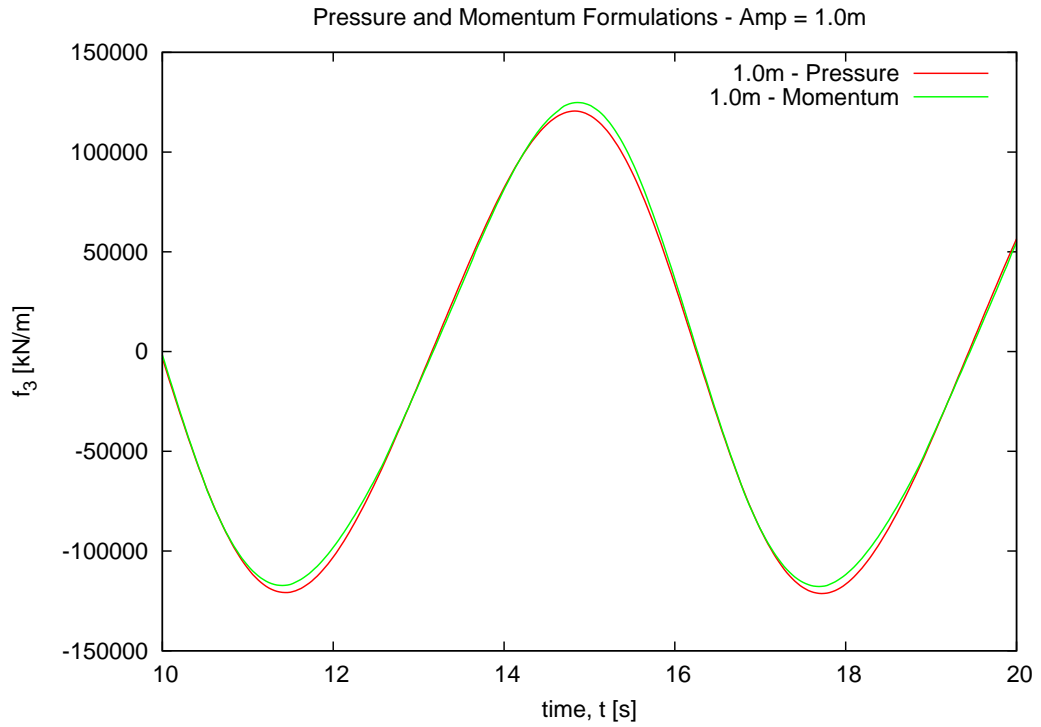
Figure A.2: Pressure and Momentum Comparison - Heaving Circular Section at 1.0m Amplitude
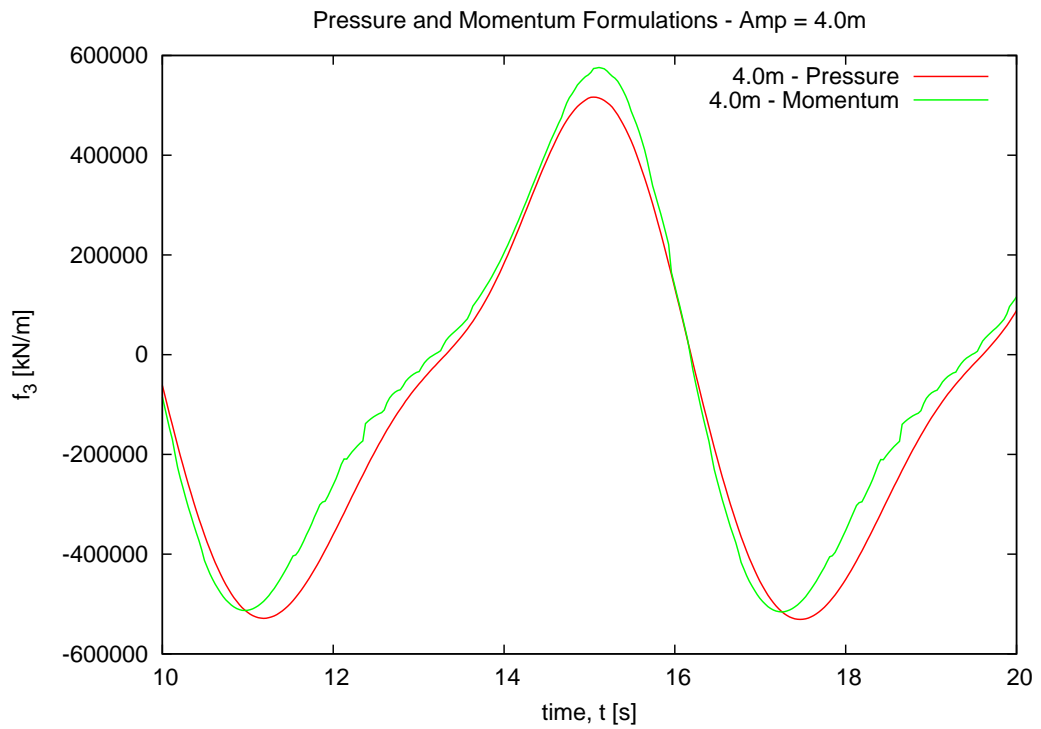

Figure A.3: Pressure and Momentum Comparison - Heaving Circular Section at 4.0m Amplitude
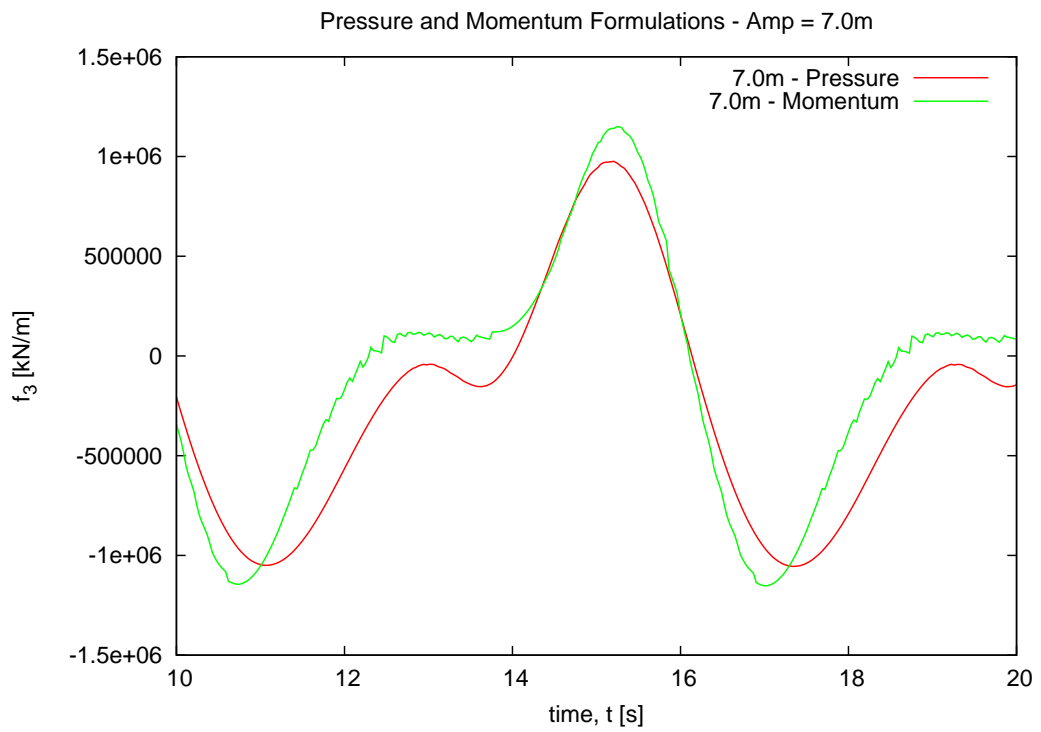
Figure A.4: Pressure and Momentum Comparison - Heaving Circular Section at 7.0m Amplitude

APPENDIX B

Influence Matrices for Two-Dimensional Problem

In the two-dimensional boundary value problem, we use a source distribution to satisfy the free surface and body boundary conditions. The free surface is modeled using desingularized sources, while the body is modeled using constant strength flat panels. In this section, the influence of a source point or panel on any field point is derived. This includes the influence to get the potential and it's derivatives in space at any field point. Along the way, common variables will be introduced that frequently appear in the derivations. These are intended to make more compact formulas, and are also helpful in terms of computational effort. The variables can be computed for each source influence on a field point and then used to determine the proper influence coefficients. It reduces the computational effort in setting up the influence matrices.

The Rankine source Green function used in the two-dimensional problem is

$$G(\mathbf{x}_i; \boldsymbol{\xi}_j) = \quad \ln r \qquad \text{is the Green function} \tag{B.1}$$

$$\mathbf{x}_i = \quad (y_i, z_i) \qquad \text{is the field point} \tag{B.2}$$

$$\boldsymbol{\xi}_j = \quad (\eta_j, \zeta_j) \qquad \text{is the source point} \tag{B.3}$$

$$r = \quad |\mathbf{x}_i - \boldsymbol{\xi}_j| \qquad \text{is the distance between the points} \tag{B.4}$$

Now, we derive the influence of one source point on one field point, so the indices can be dropped. This simplifies the mathematical notation in the following derivations. The following terms are also defined

$$\Delta y = \quad y - \eta \tag{B.5}$$

$$\Delta z = \quad z - \zeta \tag{B.6}$$

$$\mathbf{N} = \quad (N_2, N_3) \qquad \text{is the two-dimensional unit normal} \tag{B.7}$$

$$r = \quad \sqrt{\Delta y^2 + \Delta z^2} \tag{B.8}$$

where $\mathbf{N}$ will be the unit normal on the field point. It is well-defined on the body, and equal to $(0, 1)$ on the linearized free surface.

The derivation for desingularized point sources and panels is slightly different. Let GS be the point source influence, and GP be the line source influence on a panel of length L.

$$GS = \quad \ln r \tag{B.9}$$

$$GP = \quad \int_L \ln r \, dl \tag{B.10}$$

The space derivatives are found by simply taking the partial derivatives with respect to the variables y, z. The notation will be such that GS_y, GS_z are the $y-$ and $z-$ partial derivatives of GS. Second derivatives follow a similar notation. The gradient of GP, for example, would be given by $\nabla GP = (GP_y, GP_z)$.

First, we derive the influence of a desingularized point source. Finding the potential from the influence is trivial, given by Eqn. B.9. Its derivatives are given

by

$$GS_y = \frac{\Delta y}{r^2} \tag{B.11}$$

$$GS_z = \frac{\Delta z}{r^2} \tag{B.12}$$

$$GS_{yy} = -GS_{zz} = \frac{\Delta z^2 - \Delta y^2}{r^4} \tag{B.13}$$

$$GS_{yz} = GS_{zy} = \frac{-2\Delta y \Delta z}{r^4} \tag{B.14}$$

The derivation of the constant strength flat panel, or line source, influence is a bit more cumbersome. Since the integrals are along the panel, we introduce a new variable t that is tangent to the panel in the $yz - plane$, in a direction of negative rotation about x, using the right-hand rule. The integration is now in one space dimension, and goes from $-L/2$ to $L/2$, as shown in Figure B.1. The variables η, ζ have been parameterized by the single variable t, such that

$$\eta^* = \eta - tN_3 \tag{B.15}$$

$$\zeta^* = \zeta + tN_2 \tag{B.16}$$

$$GP = \int_{-L/2}^{L/2} \frac{1}{2} \ln([y - (\eta - tN_3)]^2 + [z - (\zeta + tN_2)]^2) dt \tag{B.17}$$

$$GP = L(\frac{c_1 + c_2}{4} - 1 - \ln 2) + a_2 c_0 + a_1 \frac{c_1 - c_2}{2} \tag{B.18}$$

100
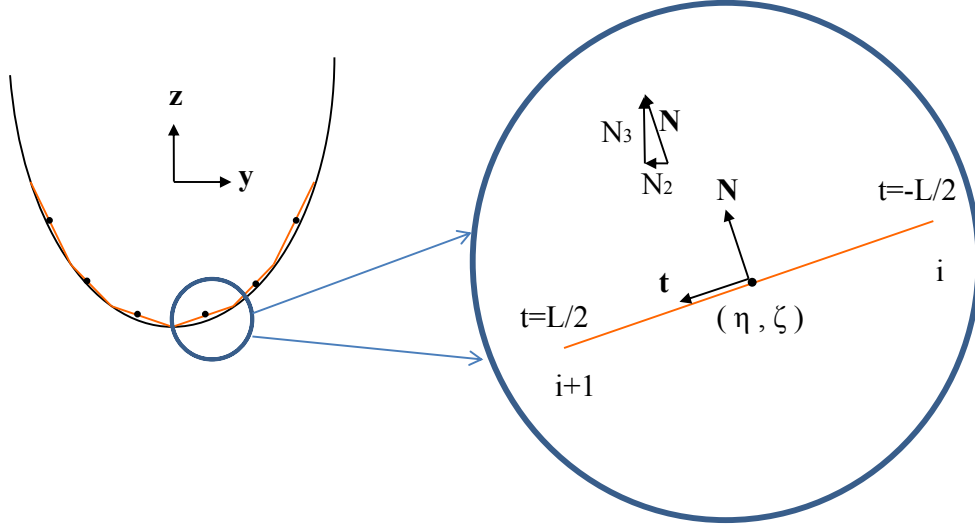
Figure B.1: Parameterization of panel integrals using t, the tangent variable

$$
\text{where} \quad a_1 \;=\; -\Delta y N_3 + \Delta z N_2
$$

$$
a_2 \;=\; -\Delta y N_2 - \Delta z N_3
$$

$$
b_1 \;=\; r^2 + \frac{L^2}{4}
$$

$$
b_2 \;=\; a_1 L
$$

$$
c_0 \;=\; arctan(\frac{\frac{L}{2} - a_1}{a_2}) + arctan(\frac{\frac{L}{2} + a_1}{a_2})
$$

$$
c_1 \;=\; \ln(4(r^2 + a_1 L) + L^2)
$$

$$
c_2 \;=\; \ln(4(r^2 - a_1 L) + L^2)
$$

And the derivatives are given by

$$
GP_y = -N_3 \frac{c_1 - c_2}{2} - N_2 c_0 \tag{B.19}
$$

$$
GP_z = N_2 \frac{c_1 - c_2}{2} - N_3 c_0 \tag{B.20}
$$

$$
GP_{yy} = -GP_{zz} = L \frac{\Delta z^2 - \Delta y^2 + \frac{L^2}{4}(N_3^2 - N_2^2)}{(b_1 + b_2)(b_1 - b_2)} \tag{B.21}
$$

$$
GP_{yz} = GP_{zy} = 2L \frac{-\frac{L^2}{4} N_3 N_2 - \Delta y \Delta z}{(b_1 + b_2)(b_1 - b_2)} \tag{B.22}
$$

Finally, the limiting case of $\mathbf{x} = \boldsymbol{\xi}$ must be examined. This is not an issue in the point source derivation, since they are desingularized. For the panel influence, we observe the following when considering a panel's influence on itself: $\Delta y = \Delta z = r = a_1 = a_2 = b_2 = 0$ and $c_1 = c_2$. This simplifies the coefficients, and we must be careful of the *arctan* terms in c_0. Taking the limit as $\mathbf{x} \to \boldsymbol{\xi}$ (from the fluid domain towards the boundary), we get $c_0 = \pi$, and the following coefficients for the panel's influence on itself

$$GP_y = -\pi N_2 \tag{B.23}$$

$$GP_z = -\pi N_3 \tag{B.24}$$

$$\tag{B.25}$$

which results in the $-\pi$ term in Eqn. 3.7, the special case of the panel's influence on itself.

APPENDIX C

Validation of Influence Matrices

The velocity potential for a circular section translating vertically an infinite fluid is given by

$$\phi = -W \frac{R^2 \bar{z}}{\bar{y}^2 + \bar{z}^2} \tag{C.1}$$

where W is the vertical velocity, R is the radius, and $\bar{y}, \bar{z}$ are the location of a point in the fluid domain, in the body-axis system. As a preliminary check, the influence matrices derived in Appendix B can be verified. The velocity potential and it's derivatives using the influence matrices can be compared to the analytic solutions.

The velocity potential and its derivatives in space (first and second) are compared. The panel method, desingularized method, and analytic solutions are compared. Figures C.1 through C.3 show the potential, its gradient, and gradient of the gradient. The values are plotted against the location on the body, in radians, measured clockwise from the positive $z-$axis. Note that Figure C.3 only shows ϕ_{yy} and ϕ_{yz}, since the following relations hold for the two-dimensional potential: $\phi_{zz} = -\phi_{yy}$ and $\phi_{zy} = \phi_{yz}$.

The potential and its gradient, shown in Figures C.1 and C.2, match exactly using all three solutions. This validates the influence matrices that were derived earlier. The second space derivatives are needed for the body boundary conditions of the radiation acceleration potential, as can be seen in Eqn. (2.65). Determining these values using
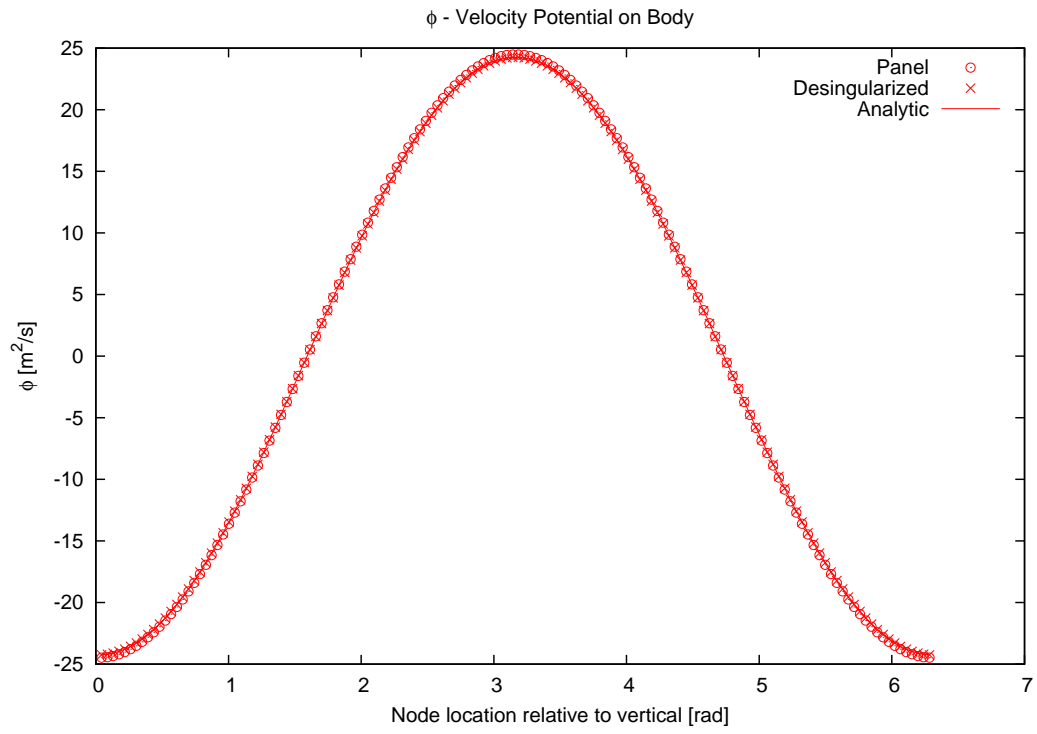
103

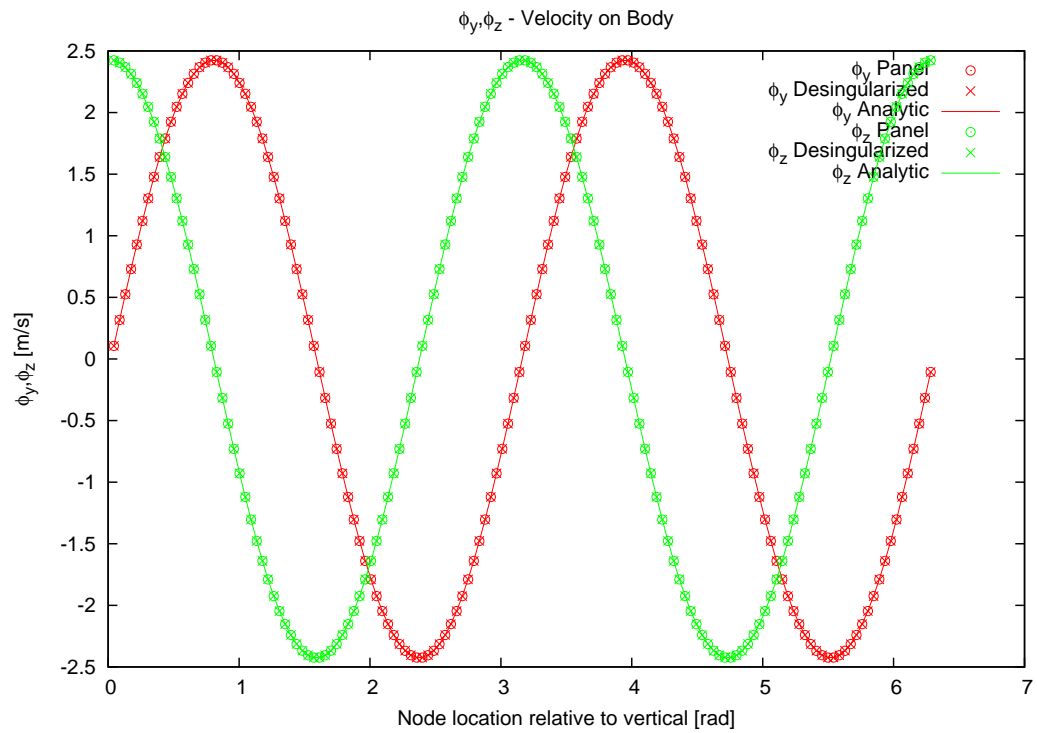Figure C.1: ϕ on Body, Deeply Submerged Heaving Circular Cylinder

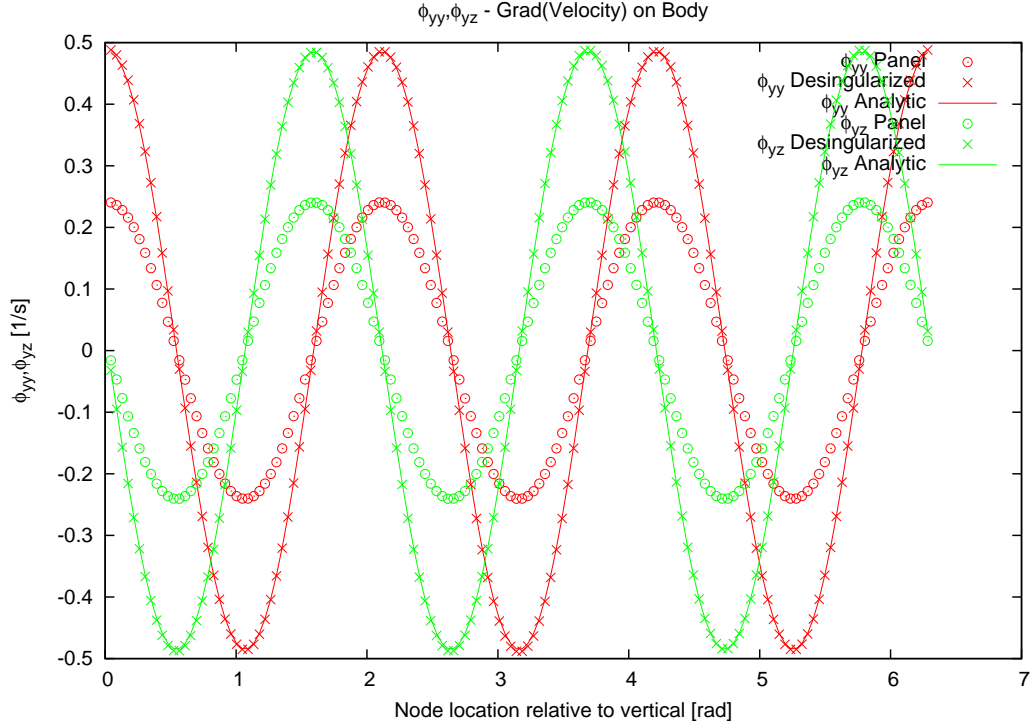Figure C.2: ϕ_y, ϕ_z on Body, Deeply Submerged Heaving Circular Cylinder

Figure C.3: ϕ_{yy}, ϕ_{yz} on Body, Deeply Submerged Heaving Circular Cylinder

the influence matrices is shown in Figure C.3, and there are significant differences when using the panel method. The influence matrices have been checked for errors, and are correct. The reason for this difference appears to be inherent to the panel method itself. Each individual panel is flat and has a constant source strength along its length. As partial derivatives are taken and found in the limit of the panel control point, or midpoint, the panel method will not provide good results for the gradient of the fluid velocity. If a field point somewhere off the panel were chosen instead, the solution would improve. An example of this can be seen in Figure C.4, plotting the second space derivates as a function of the radial distance from the control point. In this case, the panel size is $0.42m$ and $R = 10m$, and the solutions start to diverge for values of $r/R < 0.05$, or $r < 0.5m$. This suggests that using the influence matrices to find $\nabla(\nabla\phi)$ in the vicinity of the panel will yield bad results. As this distance of the field point from the panel increases, the solution approaches that of the desingularized method (assuming the desingularized point is on the "inside" of the body, while the
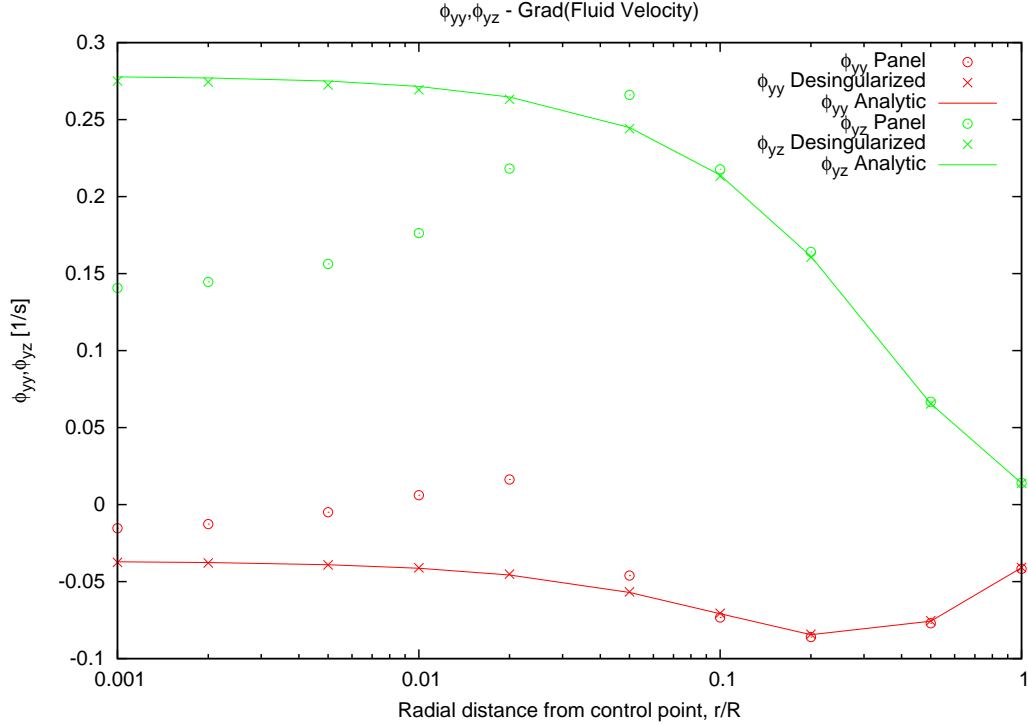
105

Figure C.4: ϕ_{yy}, ϕ_{yz} Comparison at Field Points in Fluid Domain, in Radial Direction from Body, Panel Length $dl = 0.042R$

field point is in the fluid domain).

As an alternative solution, we use the panel method solution of the gradient of phi, ϕ_y, ϕ_z, and numerically differentiate it between adjacent panels to estimate ϕ_{yt} and ϕ_{zt}, where the t subscript indicates a partial derivative in the tangential direction. The results can then be transformed back into ϕ_{yy}, ϕ_{yz} coordinates, as needed. Figure C.5 shows the improved results.

This numerical approach is accurate as long as the angle between panels does not change significantly. In most ship stations, there will only be a few "corners" (at most) where this may not work too well. Overall, since there will be 50-100 panels on a section, it will not significantly affect the solution, since this value is a higher order component in the boundary value problem and only problematic for small fraction of points.
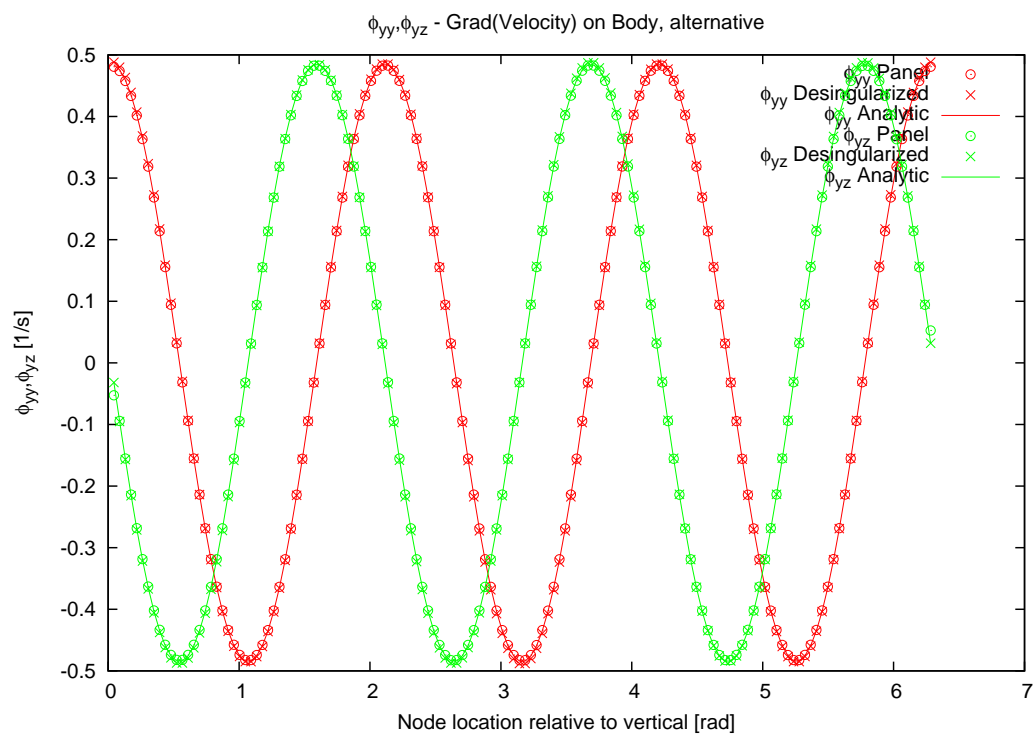
Figure C.5: Corrected ϕ_{yy}, ϕ_{yz} on Body

APPENDIX D

S-175 Response Amplitude Operators

The remaining cases of S-175 response validations are presented, completing the set of results shown in Chapter VI.
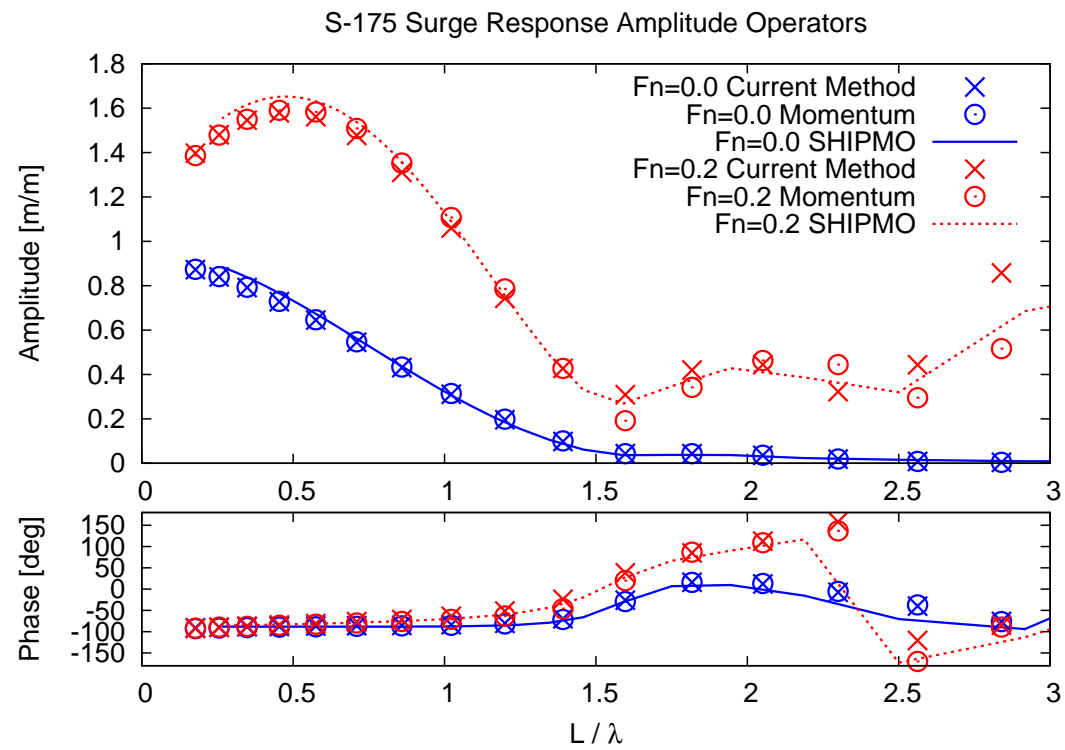
Following Seas

Beam Seas

Bow Quartering Seas
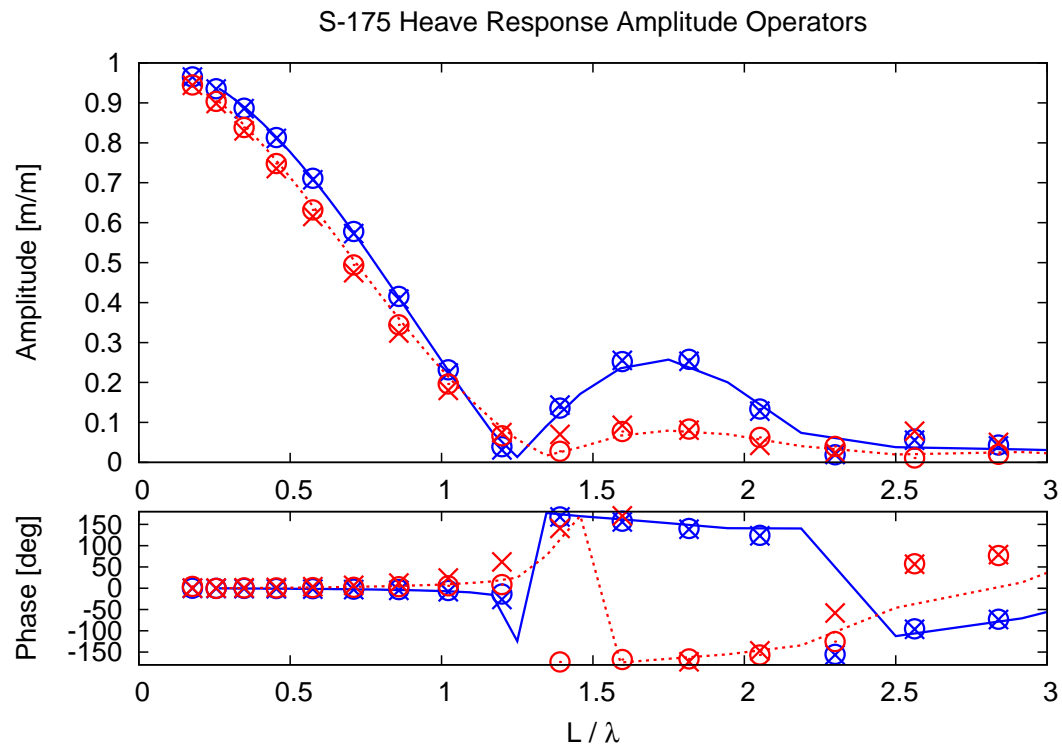
Figure D.1: S-175 Surge RAO in Following Seas
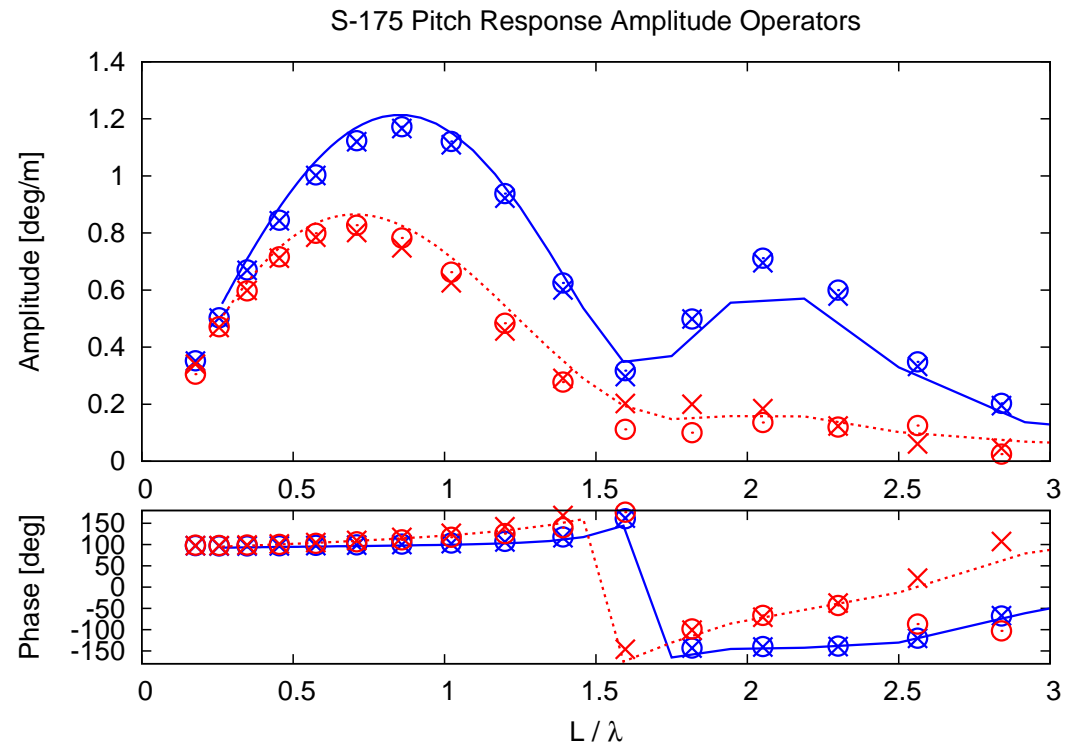

Figure D.2: S-175 Heave RAO in Following Seas

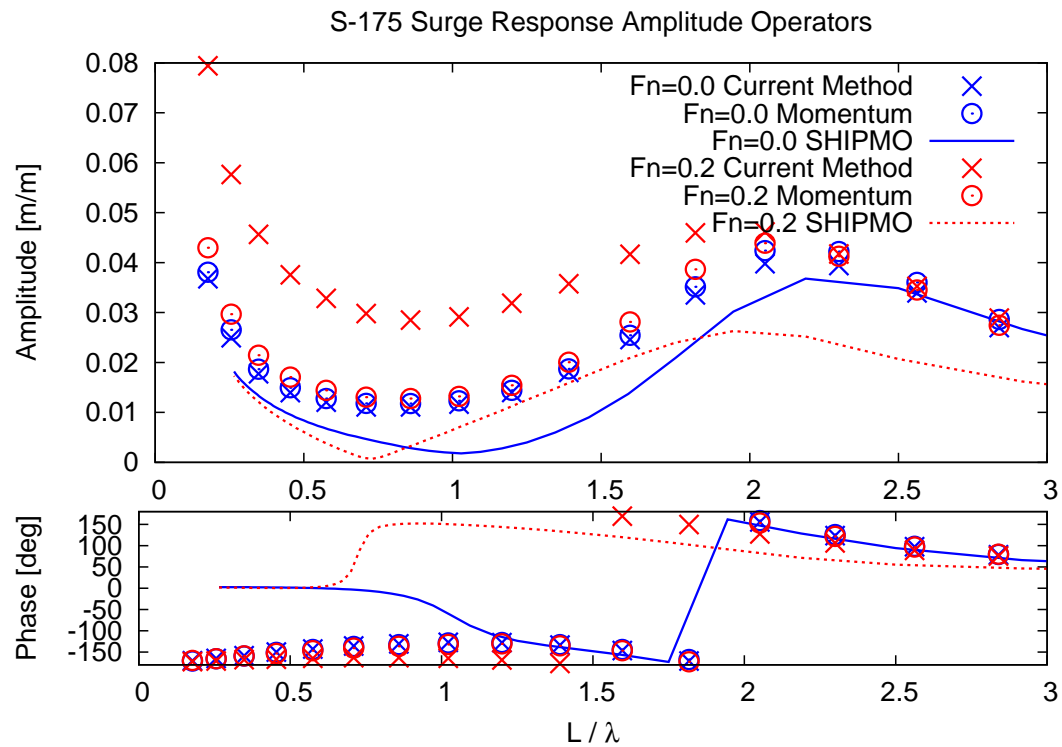Figure D.3: S-175 Pitch RAO in Following Seas
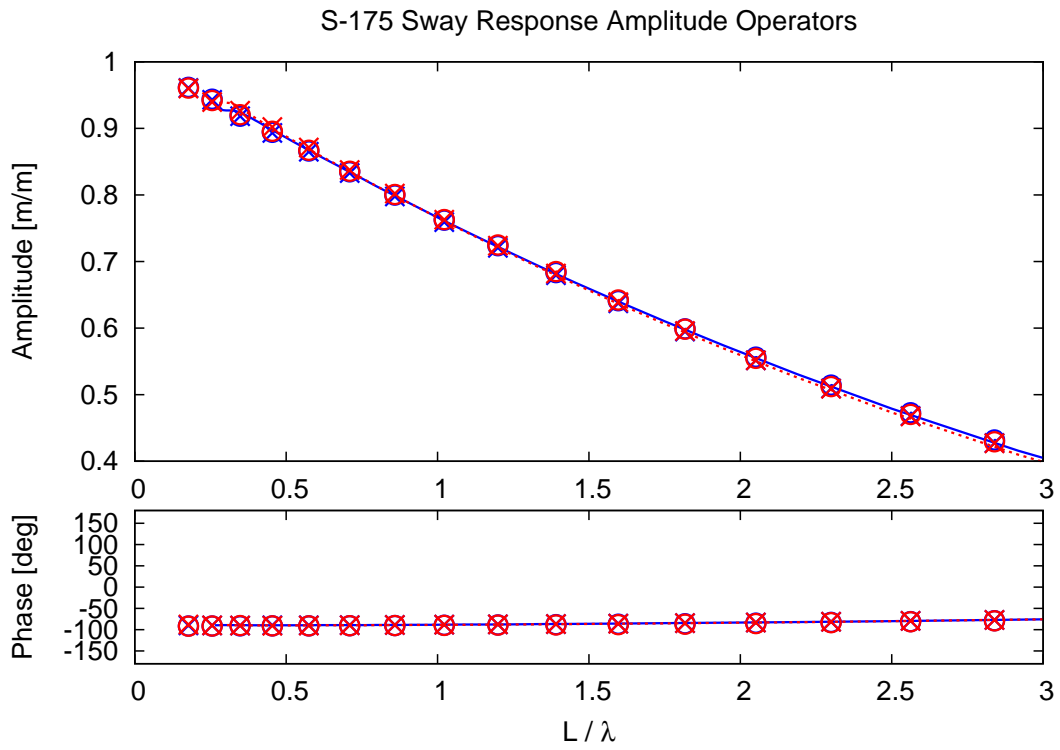

Figure D.4: S-175 Surge RAO in Beam Seas
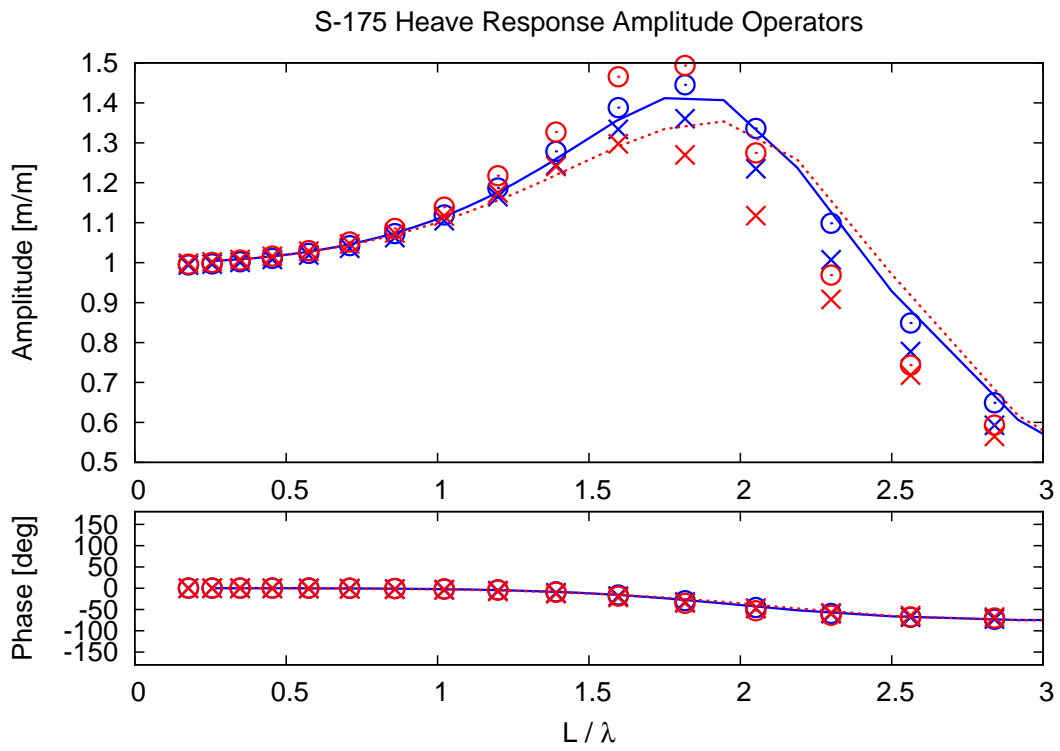
Figure D.5: S-175 Sway RAO in Beam Seas

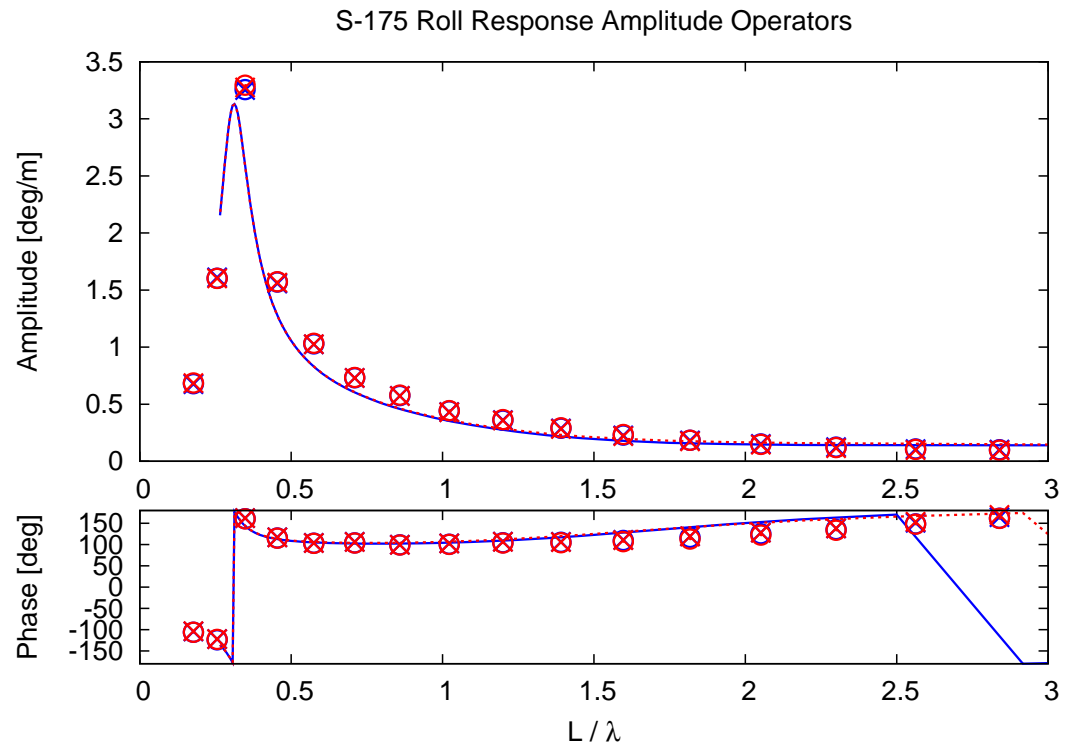

Figure D.6: S-175 Heave RAO in Beam Seas

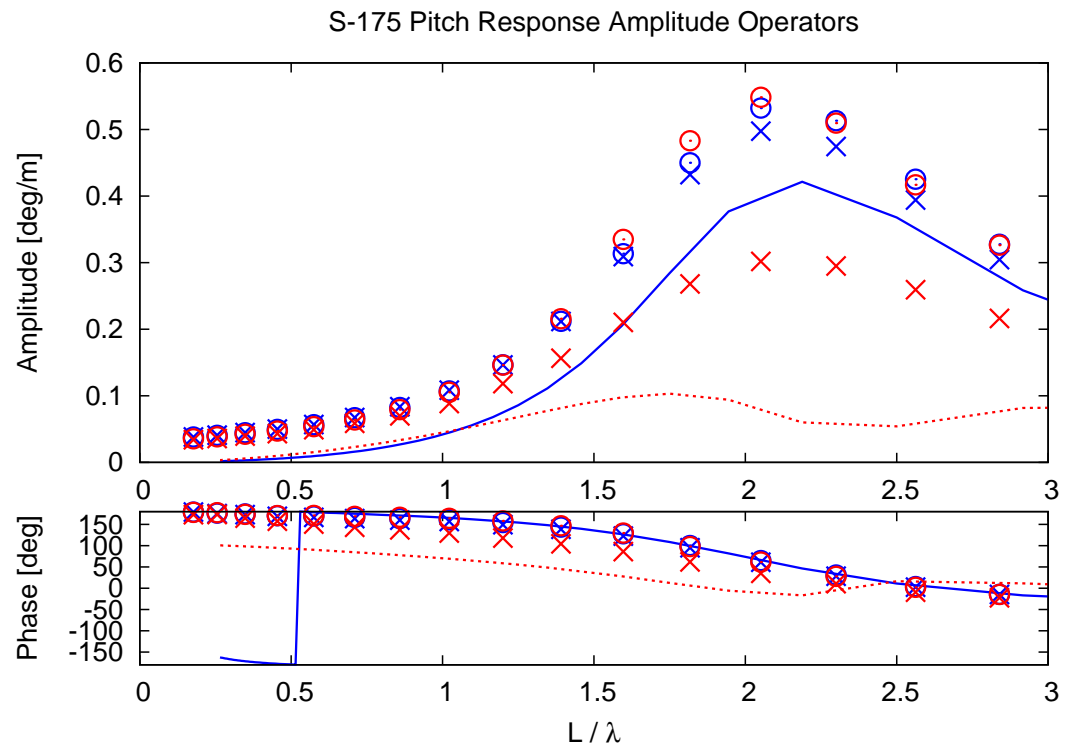Figure D.7: S-175 Roll RAO in Beam Seas

Figure D.8: S-175 Pitch RAO in Beam Seas
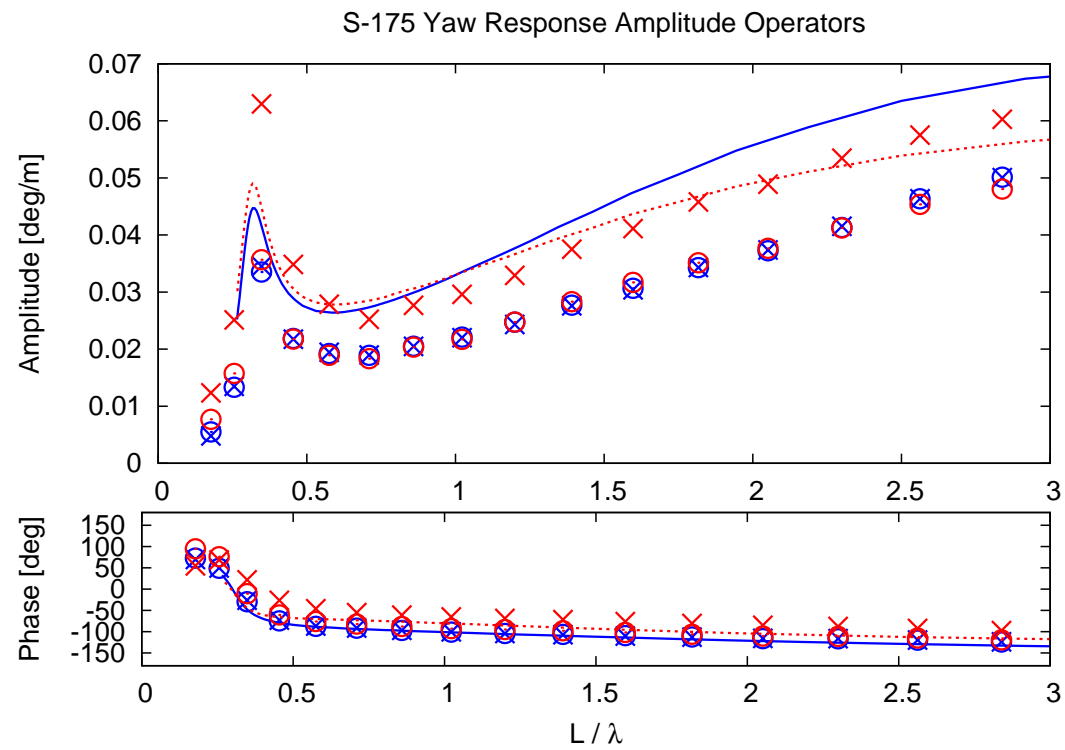
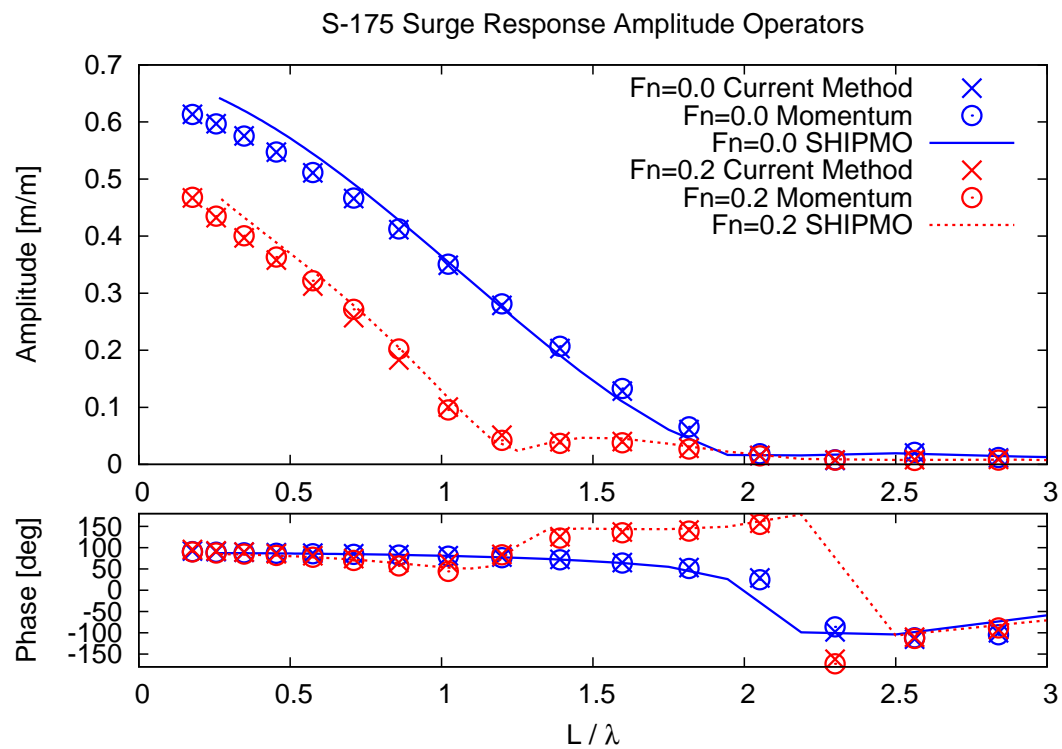Figure D.9: S-175 Yaw RAO in Beam Seas

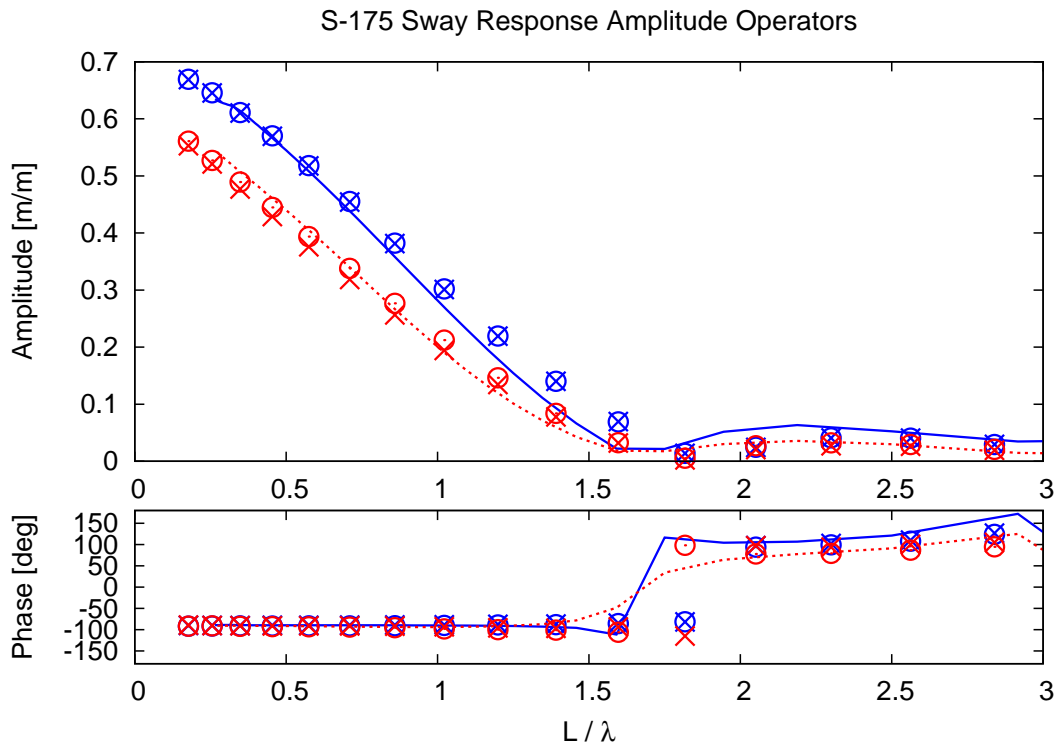Figure D.10: S-175 Surge RAO in Bow Quartering Seas

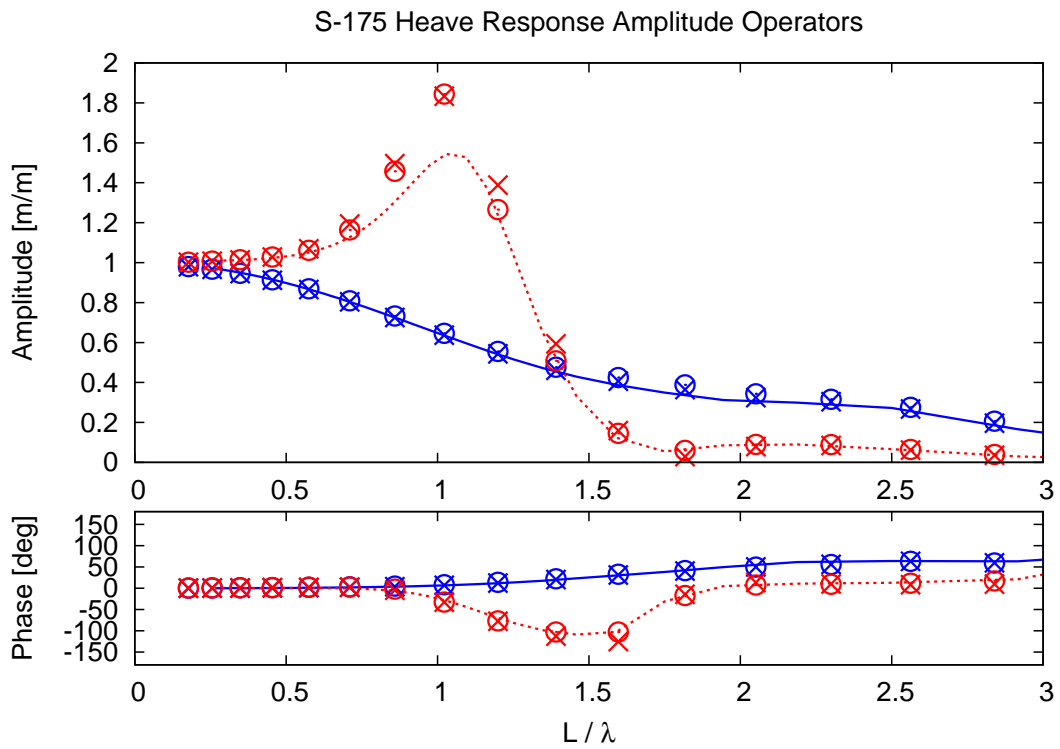Figure D.11: S-175 Sway RAO in Bow Quartering Seas

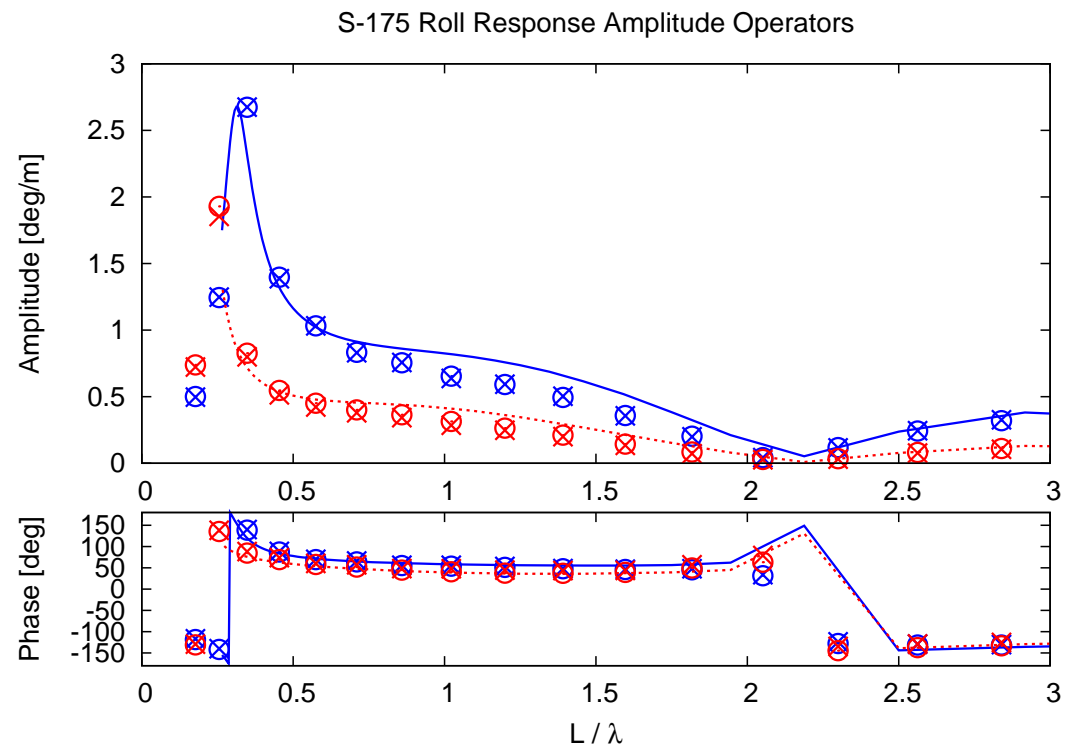Figure D.12: S-175 Heave RAO in Bow Quartering Seas

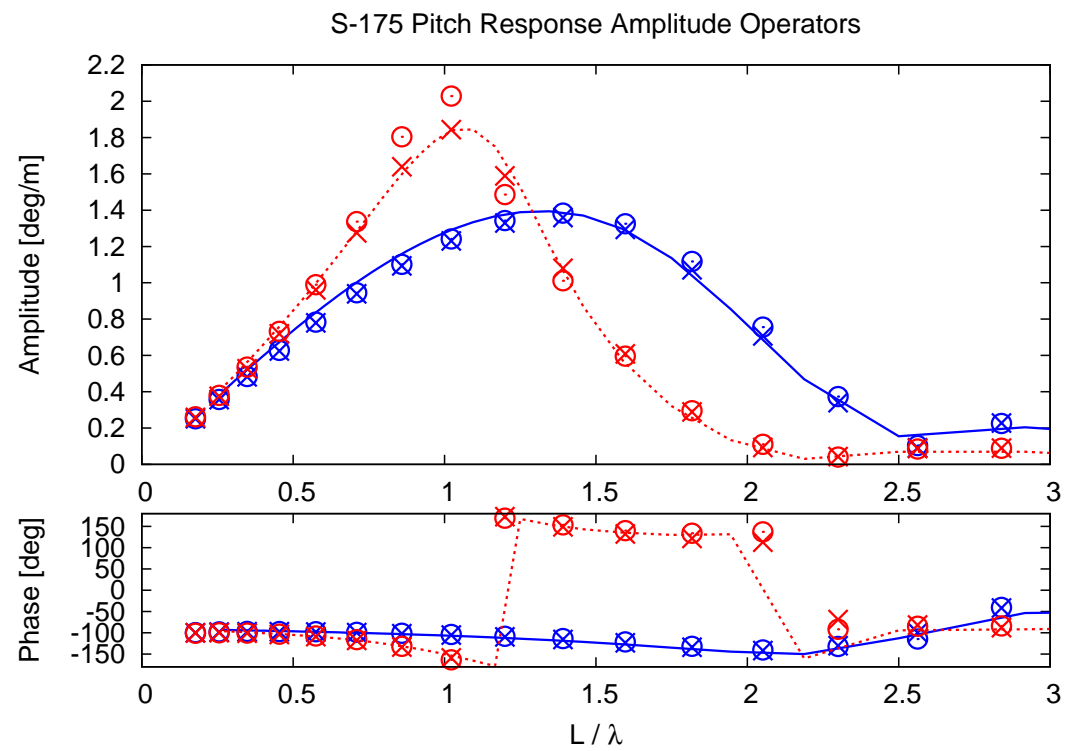Figure D.13: S-175 Roll RAO in Bow Quartering Seas
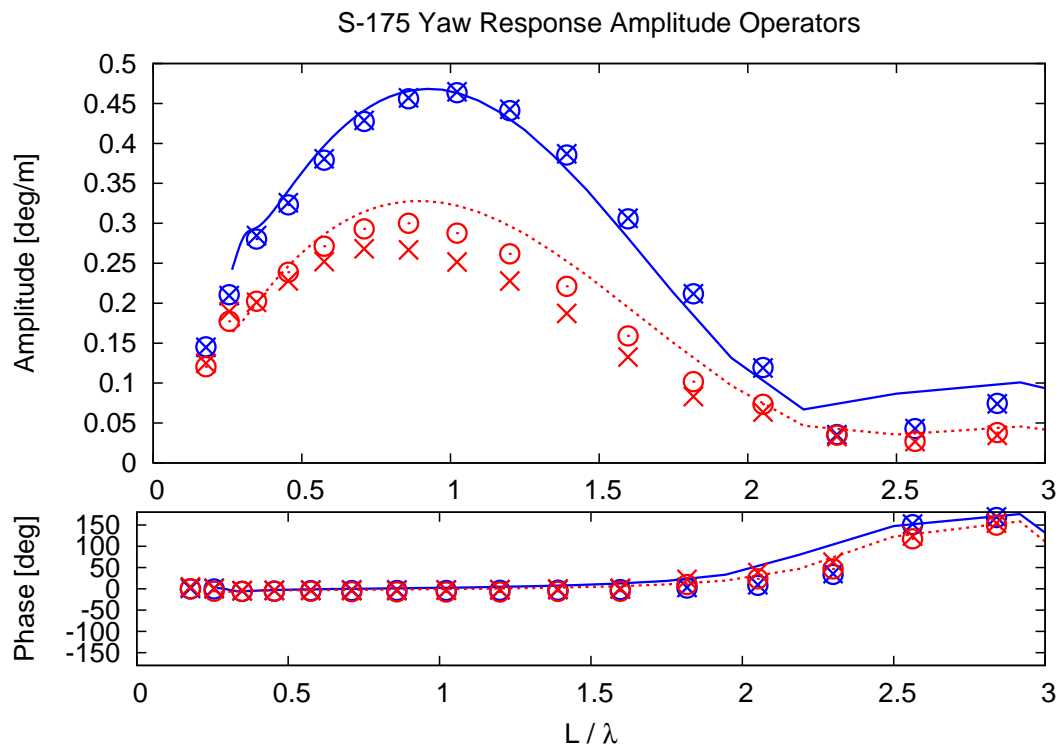

Figure D.14: S-175 Pitch RAO in Bow Quartering Seas

115

Figure D.15: S-175 Yaw RAO in Bow Quartering Seas

BIBLIOGRAPHY

BIBLIOGRAPHY

Bailey, P. A., D. A. Hudson, W. G. Price, and P. Temarel (2001). Comparisons between theory and experiment in a seakeeping validation study. *Transactions RINA*.

Bailey, P. A., W. G. Price, and P. Temarel (1998). A unified mathematical model describing the manoeuvring of a ship travelling in a seaway. *Transactions RINA 140*, 131–149.

Beck, R. F. (1989). Ship responses to regular waves. In *Principles of Naval Architecture*, Volume III, Chapter 8, pp. 41–83. SNAME.

Beck, R. F. (1999). Fully nonlinear water wave computations using a desingularized euler-lagrange time-domain approach. In *Nonlinear Water Wave Interaction*, pp. 1–58. WIT Press.

Beck, R. F., Y. Cao, S. Scorpio, and W. W. Schultz (1994). Nonlinear ship motion computations using the desingularized method. In *20th Symposium on Naval Hydrodynamics*. National Academies Press.

Beck, R. F. and A. R. Magee (1990). Time-domain analysis for predicting ship motions. In *Symposium on the Dynamics of Marine Vehicles and Structures in Waves*, Brunel University, Amsterdam, the Netherlands, pp. 49–65.

Beck, R. F. and A. M. Reed (2001). Modern computational methods for ships in a seaway. *Transactions SNAME 109*, 1–51.

Beck, R. F. and A. W. Troesch (1989). Documentation and users manual for the computer program shipmo. Technical report, The University of Michigan, Department of Naval Architecture and Marine Engineering.

Bishop, R. E. D. and W. G. Price (1981). On the use of equilibrium axes and body axes in the dynamics of a rigid ship. *Journal of Mechanical Engineering Science 23*(5), 243–256.

Buhmann, M. D. (2000). Radial basis functions. *Acta Numerica*, 1–38.

Cao, Y. (1991). *Computation of nonlinear gravity waves by a desingularized boundary integral method*. Ph. D. thesis, The University of Michigan, Department of Naval Architecture and Marine Engineering.

Cao, Y., W. W. Schultz, and R. F. Beck (1990). Three-dimensional, unsteady computations of nonlinear waves caused by underwater disturbances. In *18th Symposium on Naval Hydrodynamics*, pp. 417–425. National Academies Press.

Cao, Y., W. W. Schultz, and R. F. Beck (1991). Three-dimensional desingularized boundary integral methods for potential problems. *International Journal for Numerical Methods in Fluids 12*, 785–803.

Clarke, D., P. Gedling, and G. Hine (1983). The application of maneuvering criteria in hull design using linear theory. *Transactions RINA*, 45–68.

Dawson, C. W. (1977). A practical computer method for solving ship-wave problems. In *2nd International Conference on Numerical Ship Hydrodynamics*, Berkeley, California.

Faltinsen, O. M. and R. Zhao (1991). Numerical predictions of ship motions at high forward speed. *Philosophical Transactions A: Physical Sciences and Engineering 334*, 241–252.

Fang, M. C., J. H. Luo, and M. L. Lee (2005). A nonlinear mathematical model for ship turning circle simulation in waves. *Journal of Ship Research 49*(2), 69–79.

Finn, P. J., R. F. Beck, A. W. Troesch, and Y. S. Shin (2003). Nonlinear impact loading in an oblique seaway. *Journal of Offshore Mechanics and Arctic Engineering 125*(3), 190–197.

Fossen, T. I. (1991). *Nonlinear modelling and control of underwater vehicles*. Ph. D. thesis, Norwegian Institute of Technology, Department of Engineering Cybernetics.

Fossen, T. I. (1994). Modeling of marine vehicles. In *Guidance and Control of Ocean Vehicles*, Chapter 2, pp. 5–56. John Wiley and Sons.

Fossen, T. I. (2005). A nonlinear unified state-space model for ship maneuvering and control in a seaway. *15*(9), 2717–2746. International Journal of Bifurcation and Chaos.

Fossen, T. I. and O. N. Smogeli (2004). Nonlinear time-domain strip theory formulation for low-speed manoeuvring and station-keeping. *Modeling Identification and Control 25*(4), 201–221.

Gerritsma, J. (1988). Motions, wave loads and added resistance in waves of two wigley hull forms. *Delft University of Technology, Shiphydromechanics laboratory, Report 804*.

Gerritsma, J. and W. Beukelman (1967). Analysis of the modified strip theory for the calculation of ship motions and wave bending moments. *International Shipbuilding Progress 14*(156), 319–337.

Gerritsma, J., W. Beukelman, and C. C. Glansdorp (1974). The effect of beam on the hydrodynamic characteristics of ship hulls. In *10th Symposium on Naval Hydrodynamics*, Boston, USA.

Himeno, Y. (1981). Prediction of ship roll damping-state of the art. Technical Report 239, University of Michigan, Dept. of Naval Architecture and Marine Engineering.

Journée, J. M. (1992). Experiments and calculations on four wigley hull forms,technical report 909. Technical report, Delft University of Technology, Ship Hydromechanics Laboratory, Delft, The Netherlands.

Kang, C. G. and I. Y. Gong (1990). A numerical solution method for three-dimensional nonlinear free surface problems. In *18th Symposium on Naval Hydrodynamics*, pp. 427–438. National Academies Press.

Kansa, E. J. (1999). Motivation for using radial basis functions to solve pdes. Technical report, Lawrence Livermore National Laboratory, Livermore, Ca.

Kent, C. P. (2005). *A pseudo-spectral method for calculating wave-body interaction using an explicit free-surface formulation*. Ph. D. thesis, The University of Michigan, Department of Naval Architecture and Marine Engineering.

Korvin-Kroukovsky, B. V. and W. R. Jacobs (1957). Pitching and heaving motions of a ship in regular waves. *Transactions SNAME 65*, 590–632.

Kring, D., Y. Huang, P. Sclavounos, T. Vada, and A. Braathen (1996). Nonlinear ship motions and wave-induced loads by a rankine method. In *21st Symposium on Naval Hydrodynamics*, pp. 45–63. National Academies Press.

Lee, T. H. (1992). *Nonlinear radiation problems for a surface-piercing body*. Ph. D. thesis, The University of Michigan, Department of Naval Architecture and Marine Engineering.

Li, Z., J. Sun, and S. Oh (2009). Design, analysis and experimental validation of a robust nonlinear path following controller for marine surface vessels. *Automatica*.

Lin, W. M. and D. K. P. Yue (1990). Numerical solutions for large-amplitude ship motions in the time-domain. In *18th Symposium on Naval Hydrodynamics*, pp. 41–66. National Academies Press.

Longuet-Higgins, M. S. and E. D. Cokelet (1976). The deformation of steep surface waves on water. i. a numerical method of computation. In *Royal Society of London. Series A: Mathematical and Physical Sciences*, Volume 350, pp. 1–26.

Maruo, H. and W. Song (1994). Nonlinear analysis of bow wave breaking and deck wetness of a high-speed ship by the parabolic approximation. In *20th Symposium on Naval Hydrodynamics*. National Academies Press.

Nakos, D. and P. D. Sclavounos (1990). Ship motions by a three-dimensional rankine panel method. In *18th Symposium on Naval Hydrodynamics*, pp. 21–40. National Academies Press.

Nakos, D. E. (1990). *Ship wave patterns and motions by a three dimensional Rankine panel method*. Ph. D. thesis, Massachusetts Institute of Technology, Department of Ocean Engineering.

Newman, J. N. (1978). The theory of ship motions. *Advances in Applied Mechanics 18*, 221–283.

Newman, J. N. and T. Y. Wu (1973). A generalized slender-body theory for fish-like forms. *Journal of Fluid Mechanics Digital Archive 57*(04), 673–693.

Ogilvie, T. F. and E. O. Tuck (1969). A rational strip theory of ship motions: Part i. Technical Report 013, University of Michigan, Dept. of Naval Architecture and Marine Engineering.

Park, J. H. (1992). *The numerical stability of nonlinear floating body calculations*. Ph. D. thesis, The University of Michigan, Department of Naval Architecture and Marine Engineering.

Park, J. H. and A. W. Troesch (1992). Numerical modeling of short-time scale nonlinear water waves generated by large vertical motions of non-wallsided bodies. In *19th Symposium on Naval Hydrodynamics*, pp. 143–158. National Academies Press.

Pawlowski, J. (1992). A nonlinear theory of ship motion in waves. In *19th Symposium on Naval Hydrodynamics*, pp. 33–58. National Academies Press.

Salvesen, N., E. O. Tuck, and O. M. Faltinsen (1970). Ship motions and sea loads. *Transactions SNAME 78*, 250–287.

Sclavounos, P. D. (2008). Nonlinear response modeling of a vessel in steep random waves. Personal Correspondence with R. F. Beck.

Sclavounos, P. D., D. C. Kring, Y. Huang, D. A. Mantzaris, S. Kim, and Y. W. Kim (1997). A computational method as an advanced tool of ship hydrodynamic design. *Transactions SNAME 105*, 378–397.

Scorpio, S., R. F. Beck, and F. Korsmeyer (1996). Nonlinear water wave computations using a multipole accelerated, desingularized method. In *21st Symposium on Naval Hydrodynamics*, pp. 64–74. National Academies Press.

Scullen, D. C. (1998). *Accurate computation of steady nonlinear free-surface flows*. Ph. D. thesis, The University of Adelaide, Department of Applied Mathematics.

Sutulo, S. and C. Guedes Soares (2008). A generalized strip theory for curvilinear motion in waves. In *27th Int'l Conference on Offshore Mechanics and Arctic Engineering*. ASME.

Tanizawa, K. (1995). A nonlinear simulation method of 3-d body motions in waves: formulation with the acceleration potential. In *Proceedings of 10th International Workshop on Water Waves and Floating Bodies*, pp. 235–239.

Timman, R. and J. N. Newman (1962). The coupled damping coefficients of a symmetric ship. *Journal of Ship Research 5*(4), 1–7.

Tulin, M. and M. Wu (1996). Divergent bow waves. In *21st Symposium on Naval Hydrodynamics*, pp. 661–679. National Academies Press.

van Daalen, E. F. G. (1993). *Numerical and theoretical studies of water waves and floating bodies*. Ph. D. thesis, University of Twente, Enschede, The Netherlands.

Vinje, T. and P. Brevig (1981). Nonlinear ship motions. In *3rd International Conference on Numerical Ship Hydrodynamics*, Paris, France, pp. 257–268.

Vugts, J. H. (1968). The hydrodynamic coefficients for swaying, heaving and rolling cylinders in a free surface. *International Shipbuilding Progress 15*, 251–276.

Wang, M. and A. W. Troesch (1997). Numerical stability analysis for free surface flows. *International Journal for Numerical Methods in Fluids 24*(9), 893–912.

Wehausen, J. V. and E. V. Laitone (1960). Surface waves. In S. Flugge and C. Truesdell (Eds.), *Handbuch der Physik*, Volume IX, pp. 446–778. Springer Verlag.

Wheeler, J. D. (1970). Method for calculating forces produced by irregular waves. *Journal of Petroleum Technology*, 359–367.

Yamashita, S. (1977). Calculations of the hydrodynamic forces acting upon thin cylinders oscillating vertically with large amplitude. *The Society of Naval Architects of Japan 141*, 61–70.

Yang, J. (2004). Time domain, nonlinear theories on ship motions. Master's thesis, University of Hawaii.

Yeung, R. W. and S. H. Kim (1985). A new development in the theory of oscillating and translating slender ships. In *15th Symposium on Naval Hydrodynamics*, pp. 195–218. National Academies Press.

Zhang, X. S. (2007). *Large amplitude ship motion computations using a time dependent body geometry*. Ph. D. thesis, The University of Michigan, Department of Naval Architecture and Marine Engineering.

Zhang, X. S., P. J. Bandyk, and R. F. Beck (2007). Large amplitude body motion computations in the time-domain. In *9th International Conference on Numerical Ship Hydrodynamics*, Ann Arbor, MI, USA.

Zhang, X. S. and R. F. Beck (2007). Computations for large-amplitude two-dimensional body motions. *Journal of Engineering Mathematics (Special Volume in Honor of J. N. Newman)*.